Feasibility studies for a Transverse Deflecting Structure measurement at FLUTE

Zur Erlangung des akademischen Grades eines

Doktors der Naturwissenschaften (Dr. rer. nat.)

von der KIT-Fakultät für Physik
des Karlsruher Instituts für Technologie (KIT)

genehmigte

Dissertation

von

M.Sc. Jens Schäfer

aus Karlsruhe

Bezugnehmend auf die Stellungnahme der Deutschen Forschungsgemeinschaft vom 21. September 2023[1] möchte ich auf die Verwendung des Sprachmodells ChatGPT, Version 3.5, entwickelt von OpenAI[2], hinweisen. Dieses Sprachmodell wurde im Rahmen dieses Dokuments mehrfach verwendet, um Inspirationen für verständliche, englischsprachige Formulierungen zu erzeugen. Die endgültige Formulierung sowie die Strukturierung der Texte und insbesondere die Inhalte sind vollumfänglich und ausnahmslos eigenständig erarbeitet worden.

---

[1] `https://www.dfg.de/foerderung/info_wissenschaft/info_wissenschaft_23_72/index.html`, besucht 03.12.2023

[2] `https://chat.openai.com/`

Abstract

This thesis discusses the commissioning of the Transverse Deflecting Structure (TDS) experiment, conducted at the Ferninfrarot Linac- und Test- Experiment at the Karlsruhe Institute of Technology, Germany. The TDS experiment is a novel approach for measuring ultra-short electron bunch lengths in the femto-seconds regime. This endeavor supports a world-wide trend in accelerator facilities of optimizing towards ever-shorter bunches. As the laser-induced streaking field oscillates with around 0.3 THz, a higher measurement resolution compared to conventional RF-based streaking methods is possible. This work encompasses a theoretical examination of the streaking field, extensive simulations on the beam dynamics for different scenarios, and first experimental findings. The strategies developed on this topic lay the groundwork for transforming the TDS experiment into a routine measurement tool.
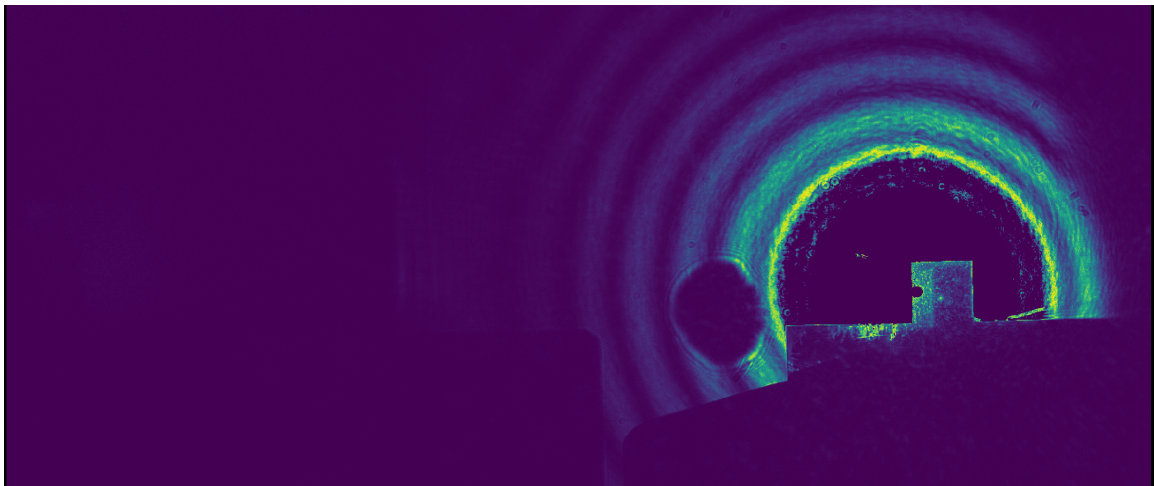
Illustration of the TDS resonator with a Split-Ring resonator geometry, recorded with the diagnostic camera of a beam screen monitor. The image was created during a laser-based alignment of the resonator, the laser interference rings align concentric around the resonator gap, where the streaking field builds up during operation.

Abbreviations

CST	Computer Simulation Technology Studio Suite
EM	Electro-magnetic
EO	Electro-optical
EMG	Exponentially modified Gaussian distribution
FLUTE	Ferninfrarot Linac- und Test-Experiment
FWHM	Full width half maximum
ICT	Integrated Current Transformer
iFFT	Inverse fast Fourier transform
IR	Infrared
IP	Interaction Point
NIPD	Normalized Integrated absolute Pixel Difference
OTR	Optical Transition Radiation
RAP	Raster Alignment Program
RF	Radio Frequency
RMS	Root Mean Square
ROI	Region of Interest
SRR	Split-Ring resonator
THz	Terahertz
TDS	Transverse Deflecting Structure
TPFM	Tilted-pulse-front modulation
UHMWPE	Ultra-high-molecular-weight polyethylene
UV	Ultraviolet
YAG	Yttrium Aluminium Garnet

Contents

Introduction

Particle accelerators are truly fascinating machines. Their operation requires a choreographed interplay of applied beam physics with the components from multiple technical fields of technology such as electromagnetic engineering or laser science. The development of accelerators is tied to the improvements within the different technical fields, in particular the discipline of beam diagnostics to which this dissertation contributes with the first feasibility studies of a low-energy transverse deflecting structure (TDS) experiment. A TDS setup will finally allow to measure the longitudinal charge profile for compactly bundled electron ensembles, referred to as bunches hereafter.

The direction of developments of accelerators varies significantly depending on their purpose. In the field of particle physics, huge colliders with progressively higher center-of-mass energies are utilized. Light sources store electron beams and generate synchrotron radiation, with the objective of approaching diffraction-limited light sources for more precise radiation or imaging techniques. Linear light sources like Free Electron Lasers (FEL) strive for increasingly shorter electron bunches, thereby optimizing their radiation towards shorter pulses and higher frequencies. One motivation for this development is the production of intense THz pulses which themselves have manifold scientific and technical applications [1], for example the live monitoring of chemical reactions [2] or the possibility for a destruction free tomography of delicate specimen. To enable these applications, a high resolution measurement of the length of ultra-short electron bunches is essential. The bunch length is comparatively challenging to measure compared to other beam parameters. Yet it stands out as one of the most relevant parameters because it determines properties of the emitted radiation but also the bunch charge density, which often becomes the dominant factor for short pulse dynamics. Despite the existence of several established technical methods for bunch length measurement, FEL or Laser-Plasma Accelerators (LPA) are already entering a regime with femtosecond lengths, surpassing conventional resolution capabilities.

A Transverse Deflecting Structure builds up an electro-magnetic streaking field that deflects the electron bunch in the vertical plane. The oscillation of the streaking field deflects the bunch's head and tail in opposing directions. This way, the transverse bunch size depends on the bunch length and the streaking field frequency. As the frequency is well defined from the resonating structure, the bunch length can be measured precisely from the bunch footprint with a beam monitor. This principle has successfully been implemented for over 20 years with Radio Frequency (RF)-cavities [3], modern setups can reach resolutions for bunch length measurements down to 100 femto-seconds [4]. Latest developments in this field utilize RF structures with a variable streaking direction, allowing for a tomographic

investigation of the bunch's phase space in five dimensions: (x, x', y, y', t). The resolution for bunch length measurements is expected to reach 20 femto-seconds [5], experimental demonstrations can be expected in the following years.

However, a new approach to the TDS principle utilizes laser-powered THz resonators, building up streaking fields with much higher frequencies of typically 0.3 THz, promising resolutions in the sub-fs regime [6]. Additionally to the improved resolution, a THz-TDS setup comes with three more advantages compared to conventional RF streaking. A TDS setup is powered from a laser-generated THz pulse. Accelerators capable of producing short bunches are typically based on an RF-photoinjector or a Laser-Plasma accelerator, both of which already require a sophisticated laser system, which can be used as the TDS driver. This cuts the cost of otherwise required acquisition and powering of a dedicated, energy hungry RF system. Another advantage is the size of the setup, as a THz-driven resonator naturally falls within the millimeter regime. This reduces the required, valuable space in the accelerator and allows for a more compact facility. The TDS experiment therefore saves on monetary, energetic and spatial expenses while offering higher resolution in the measurement of the bunch length, compared to RF-based streaking.

A first proof-of-principle was demonstrated by monitoring deflected bunch centroids in 2019 [7] and also in 2020 [8], followed by demonstrating bunch streaking in 2022 [9]. However, THz-based streaking is experimentally challenging and demands high level of stability and precision in alignment and synchronization. Also, the stated experiments have examined bunches with charges below 5 pC, while this technique is especially interesting as a measurement procedure for LPA-based accelerators, which often operate with higher charges.

The Ferninfrarot Linac- und Test-Experiment (FLUTE), located at the Karlsruhe Institute of Technology, provides a versatile platform with a broad range of addressable bunch parameters.[10] This RF-photoinjector based accelerator allows to tune several bunch parameter, among them the bunch charge and even the bunch length, providing a versatile test bench for the TDS device in various different scenarios. Therefore the test experiment is a perfect location for a feasibility study of the TDS setup with higher bunch charges.

The experimental challenges require a holistic examination of the accelerator and the accompanying laser system which are both introduced in Chapter 1. For the feasibility study, a clear expectation on the streaking field and its impact on the electron bunch is required, these topics are addressed in Chapter 2. One major experimental challenge arises from the spatial confinement of the streaking field which is spatially limited to a gap in the resonator measuring merely $20\,\mu m \times 20\,\mu m$, electron bunch sizes with charges above 5 pC usually have significantly larger beam sizes. This impedes guiding the bunch through the streaking field and thus hinders the detection of a streaking signal. A strategy to handle this difficulty is elaborated by extensive simulations on the beam dynamics in the FLUTE parameter space, aiming for beneficial bunch parameters to facilitate the commissioning. Two distinct strategies have been determined in the scope of Chapter 3. The exceptional experimental challenges of the required precision and stability for a micrometer alignment and a picosecond synchronization, and the handling thereof are discussed in Chapter 4. Finally, Chapter 5 presents advanced strategies designed to simplify future streaking

experiments, featuring an improved resonator geometry and optimizations distributed across all topics touched so far.

1. The experimental setup at FLUTE

For the commissioning of the Transverse Deflecting Structure (TDS) experiment, a holistic perspective on the Ferninfrarot Linac- und Test-Experiment (FLUTE) is necessary, involving the accelerator, laser and diagnostic components. The electron beam must be ideally focused to efficiently guide sufficient charge through the tiny resonator gap and the streaking field therein. Consequently, the limitations and possibilities of FLUTE are comprehensively discussed. The here introduced degrees of freedom are examined by simulations in Chapter 3 or directly tested experimentally in Chapter 4. A precise understanding of the TDS setup is essential for this endeavor, the TDS experimental chamber, with its internal components is introduced as well. The actual dynamics occurring in the TDS resonator are topic of the subsequent Chapter 2.

An overview of the most crucial components in the low-energy section of FLUTE is presented in fig. 1.1. These components have been categorized into four distinct groups, each designated by its respective label color. Over the next four sections, each category is discussed separately:

Section 1.1: Bunch controlling elements (green labels)

Section 1.2: Diagnostic devices (blue labels)
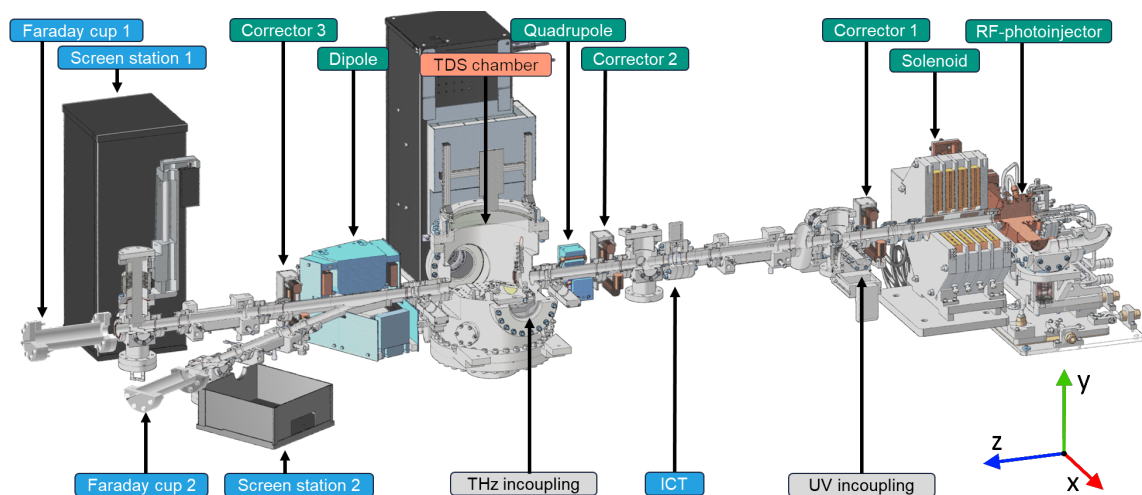
Figure 1.1.: CAD drawing of the FLUTE low energy section with beam controlling elements (green labels), diagnostics (blue). Also the UV and THz incoupling (grey) and the TDS chamber (orange) are displayed. Depending on the dipole field, the beam path follows either the straight arm for the streaking measurement or the curved, spectrometer arm for the energy measurement. The overall length is 2.8 m. Figure based on a CAD drawing from S. Schott, IBPT

Section 1.3: Laser components (gray labels)

Section 1.4: The TDS chamber (orange label)

FLUTE generates bunches by the photoelectric effect [11], making the laser system a fundamental component. The laser components themselves are not explicitly displayed in this figure, with the exception of their entry points into the accelerator, labeled as THz- and UV incoupling. A dedicated illustration of the relevant laser components can be found in the corresponding laser section.

The TDS chamber is situated in the middle of the low-energy section. Within this chamber, several components are housed, one of which is the TDS resonator, where the streaking effect takes place. These components, their purpose and alignments are introduced here, the actual Electro-magnetic (EM)-dynamics in the resonator will be discussed in detail in the next chapter 2.

Coordinate System: For the scope of this thesis a global, right-handed coordinate system is used, it is presented also in fig. 1.1.

- The x-axis is horizontally aligned.

- The y-axis is vertically aligned and points upwards.

- The z-axis is longitudinal aligned and follows the beam pipe.

The same coordinate system is applied inside the TDS chamber which will be explained in detail later in section 1.4.1.

1.1. Accelerator components

1.1.1. RF-photoinjector

The RF-photoinjector is the most crucial component of this accelerator. It emits the electrons from a copper cathode by the photoelectric effect, using an Ultraviolet (UV) laser pulse with a wavelength of 266 nm. Further it applies an RF field on the bunch that accelerates and also focuses the bunch, therefore this component already defines most of the bunch parameters. It operates within the S-band[1] at a frequency of 2.9985 GHz[2] and consists of a 2.7-cell injector, meaning the first cell is truncated and the latter two span half the RF wavelength each. The first, truncated cell compensates for the initially slow electron velocity and allows for optimal acceleration throughout the entire structure. This RF-photoinjector was initially designed for high bunch charge configurations of up to 1 nC [12], specifically tailored to withstand operation in a bunch train mode. To support

---

[1] The term S-band refers to waves with frequencies between 2 GHz and 4 GHz.
[2] This frequency is a european standard for RF sources designated for particle accelerators, featuring a wavelength of 10 cm which facilitates manufacturing.
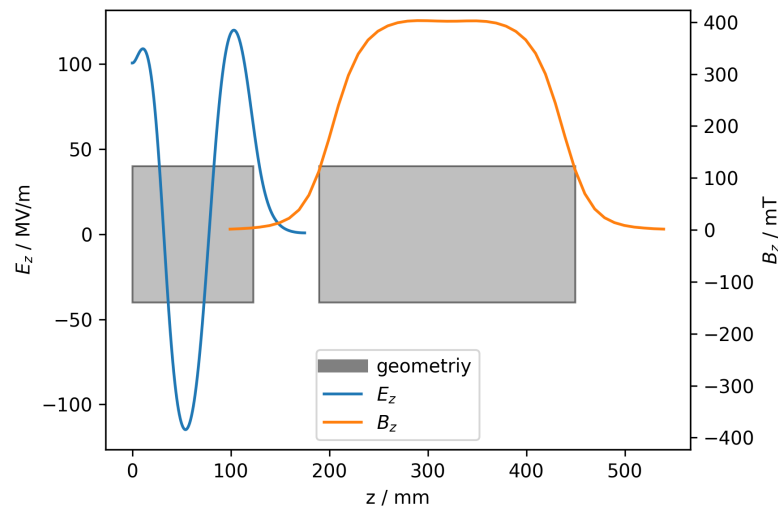
Figure 1.2.: Field profile of the oscillating, accelerating electric field in the RF photoinjector (blue) and of the static, focusing solenoid magnetic field (orange). The electric field is displayed for a fixed time. The boxes display the geometrical outline of the two elements.

such a high charge release, the back plane of the injector is curved such, that charges released even centimetres off-axis still are guided onto the symmetry axis and may leave the injector, contributing to the bunch current. Because of this design choice, a relatively large dark current up to several hundred pico-coulombs is ubiquitous even while operating with small bunch charges, which has to be addressed in the data analysis.

The distribution of the accelerating field is plotted in fig. 1.2 (blue), alongside the solenoid magnetic field (orange). While the magnetic field of the solenoid is static, the electric field of the photoinjector oscillates, and the plotted distribution represents the field at the time of maximum amplitude. The components geometric expansions are marked with gray boxes. Both fields leak out of their components outline and overlap in the 65 mm gap between their geometry.

Degrees of freedom: The RF photoinjector effectively has two degrees of freedom to alter bunch parameters for the TDS experiment, the RF phase and the RF field strength.

The electric field strength can be raised up to 120 MV/m, enough for accelerating electrons to an average momentum of 8.5 MeV/c. However, for the standard operation at around 5 MeV/c, a field strength of approximately 80 MV/m suffices. The timing system allows to delay the RF pulse granting the flexibility to select the desired relative RF phase at which the laser pulse reaches the cathode. Changing the amplitude primarily affects the energy distribution and also the released amount of electrons, because the RF field effectively reduces the cathode materials' work function [13].

The RF phase can be tuned freely over 360°, from which only a window of around 90° effectively allows for a bunch to form and exit the photoinjector. Changing the phase significantly impacts the bunch creation process, ultimately defining fundamental parameters

like its size, energy, charge or the energy allocation along the bunch length, commonly referred to as bunch chirp.

Another crucial parameter affected by the RF phase is the bunch emittance, it can be interpreted as a measure of "bunch quality" in either the horizontal, vertical or longitudinal axis. In this thesis, the term emittance refers exclusively to the transverse Root Mean Square (RMS) emittance of a particle distribution, calculated as:

$$\epsilon_{\text{RMS}} = \sqrt{\langle x^2 \rangle \langle x'^2 \rangle - \langle xx' \rangle^2} \,. \tag{1.1}$$

Here x is either the horizontal or verticle particle position, x' the according horizontal or verticle particle trajectory angle against the reference path and the brackets $\langle \rangle$ describe the variance calculated on the particle ensemble. The emittance therefore depends on the bunch size, its divergence and a link thereof. For a given emittance, the bunch size can only be reduced by increasing its divergence, hence in context of the TDS experiment, a small emittance is generally desirable. This consideration will be addressed during optimizations in subsequent chapters.

In the TDS experiment, the photoinjector's RF phase and field strength are dominant parameters for altering bunch parameters and therefore for selecting a good working point of the accelerator.

Electron energy gain: The electrons are released from the cathode on the laser impact. If the RF phase is set correctly, the electrons reach the first iris at the end of the first, truncated cell precisely when the RF-field transitions from an accelerating to a decelerating amplitude. Consequently, the electrons enter the second cell and again experience an accelerating field. This exact phase is labeled with zero degree in this thesis, it provides ideal acceleration conditions and leads to the highest possible bunch energy.

Fig. 1.2 illustrates the electric field at one particular time stamp, while fig. 1.3 (a) displays the electric field as experienced by two particles as probes: the first probe starts with the RF phase set to 0° for ideal acceleration (blue) and the second starts with the phase for maximum charge production (orange), the phase of −54° will be motivated in brief. The second subplot, fig. 1.3 (b), shows the energy gain through the photoinjector for both probes. One can see that the second probe experiences briefly decelerating fields, as shown in subplot (a), where the experienced field amplitude falls below zero. Consequently, the energy decreases at these positions.

These results were obtained through a numerical calculation based on the field distribution. For this specific calculation, the RF amplitude was set to 65 MV/m, resulting in a final electron energy of approximately 4.3 MeV for zero degrees.

Charge production: The RF field amplitude at the cathode surface reduces the copper work function, allowing the laser pulse to release more charge. Thus, the RF phase correlates with the charge production. A measurement of the bunch charge for a broad
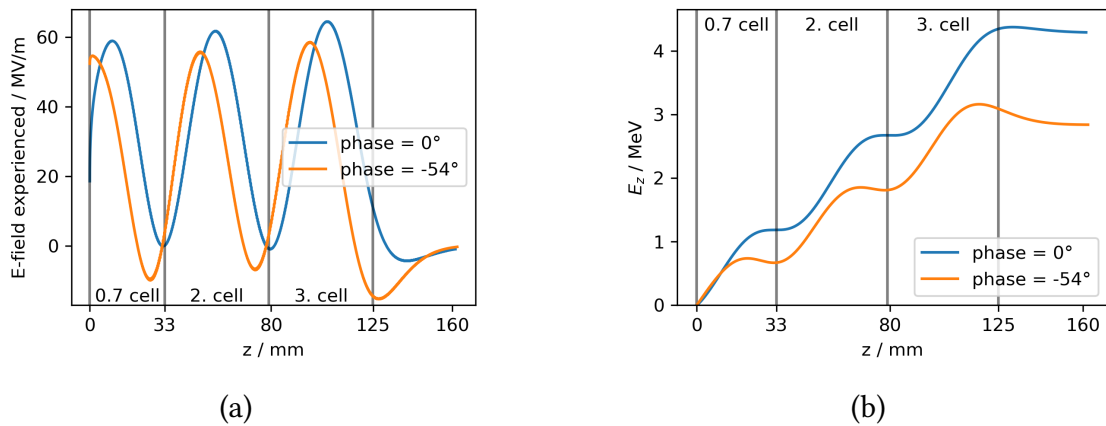
Figure 1.3.: Effects of the accelerating field inside the RF photoinjector on an electron probe, beeing released on either the RF phase for ideal acceleration (blue, 0°) or the phase for ideal charge production (orange, −54°). a) The experienced field for the probes as the field oscillates in time during the travel time. The subplot b) shows the energy gain for the probes in the RF photoinjector as a consequence of the experienced field. The RF peak field amplitude is set to 65 MV/m which leads to a final bunch energy of approximately 4.3 MeV.
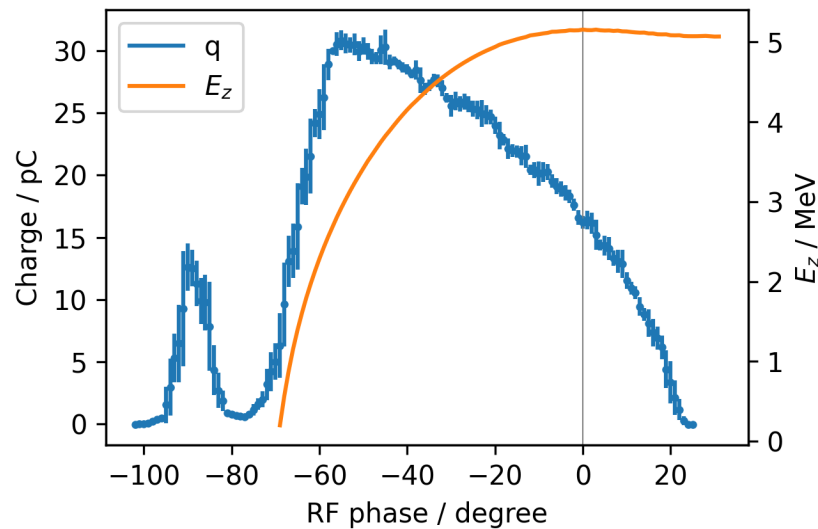
Figure 1.4.: Characteristic phase scan of an rf photoinjector, with the bunch charge (blue, measured) and energy (orange, simulated).

phase window is shown in fig. 1.4 (blue). Additionally the calculated bunch energy for this phase window is plotted too (orange).

For the phase of ideal acceleration, when the electron reaches the first iris, the RF field proceeds to its zero crossing and the amplitude is modulated to $\cos(\pi) = 0$ of its nominal amplitude. Because of the 0.7 cell design, the phase when the electrons were released from the cathode was 0.7π earlier, assuming the electron travels at the speed of light. This means, that the amplitude during the laser impacted was modulated by $\cos(\pi - 0.7\pi)$ in the case of ideal acceleration. For ideal charge production, the maximum possible

9
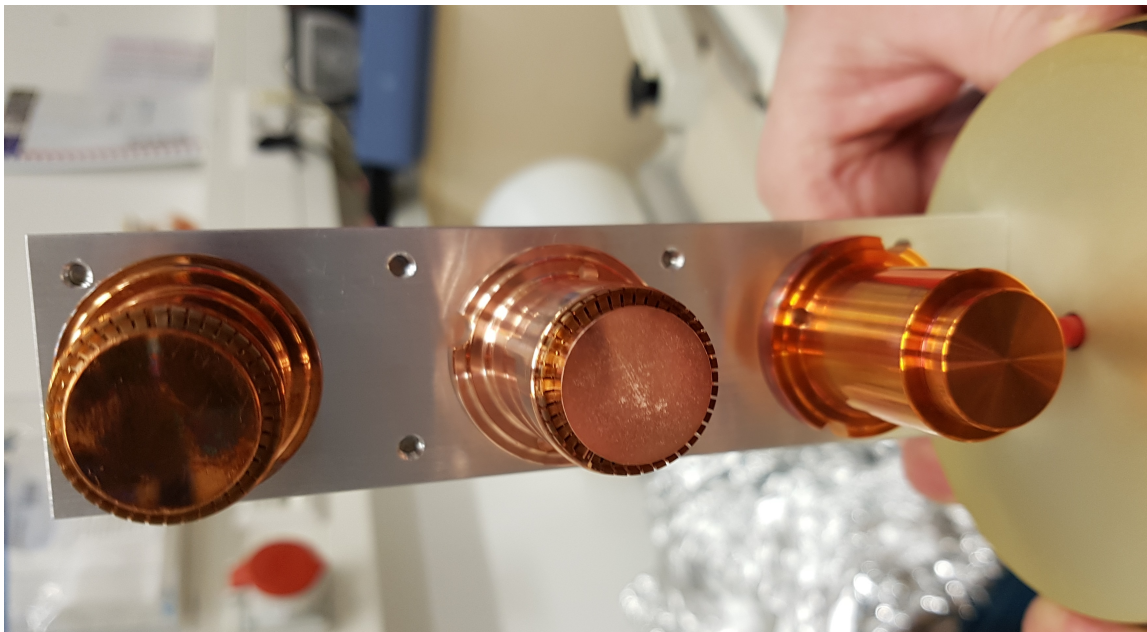
Figure 1.5.: Exchangeable Cu-cathodes for the FLUTE RF-photoinjector. The middle specimen exhibits damages caused by laser irradiation and RF breakdowns. Image from T. Schmelzer, IBPT.

amplitude $\cos(0)$ needs to be present during laser impact, which is the case for an RF phase $-0.3\pi = -54°$ below the phase for ideal acceleration. This can be seen also in the phase scan plot, as the bunch charge is highest at around $-54°$. For phases below $-54°$ and above $0°$, acceleration conditions become so bad, that less and less electrons exit the photoinjector, causing a rapid drop in the measured charge.

Another prominent feature in this plot is the "side bump", where bunched charge leaves the photoinjector in a second phase window of $[-100°; -80°]$ with a clear peak at $-90°$. This is a prominent feature across several different RF photoinjector based accelerators, see [14, 15]. In this regime, the electron experiences accelerating forces only up to the first half of the 0.7 cell, followed by deceleration, preventing it from leaving the first cell. Eventually, the electron turns around, colliding with the cathode again and releasing secondary electrons. These secondary electrons are generated at just the right time to experience accelerating RF fields again, forming a secondary bunch that leaves the photoinjector. However, these sidebump-generated bunches are diffuse and unsuitable for experiments. Nevertheless, the conditions for creating these bunches are so specific that the sidebump charge maximum serves as a fixed point in the experiment. This maximum can be experimentally found fairly quickly and precisely, indicating the characteristic phase of $-90°$.

Cathode: FLUTE uses interchangeable copper cathodes, which is essential due to occasional damage to the surface during operation, three specimens are depicted in fig. 1.5. At the beginning of this thesis measurement campaign, it was observed that the installed cathode had experienced damage from the previous experiments, it is the central specimen

in the picture. This damage resulted in a 10 % variation in the bunch charge depending on the laser impact point [16]. Subsequently, the cathode was replaced with a new one, thereby enabling ideal conditions for the TDS experiment.

To maintain consistent conditions throughout the experiment, we determined the limit of laser power density for non-destructive operation experimentally. Detailed information regarding this is provided in the appendix A.1.

1.1.2. Solenoid

The solenoid has a focusing effect on the electron bunch, the field distribution is illustrated in fig. 1.2. Its approximately homogenetic field strength increases linearly with the current passing through with an upper limit of roughly 400 mT .

Focusing dynamics within the solenoid are relatively complex [17]. In simple terms, off-axis electrons are compelled to follow a helical trajectory parallel but offset from the magnetic axis. This helical motion is initiated by the first and stopped by the second fringe field. As a result, two effects will occur. First, electrons are brought closer to the magnetic axis within the solenoid. Secondly, upon exiting the solenoid, they retain a residual radial momentum directed toward the central axis. Then the bunch has to travel further for the focal length to become ideally focused. These dynamics are radially symmetric, in contrast to a quadrupole.

To facilitate beam alignment in the single digit micrometre-level, the entire solenoid is mounted on a motorized stage, offering adjustments for x, y, tilt, and pivot. This setup, combined with the corrector magnets allow for accurate beam-based alignment.

In the experiment the solenoid is mostly set to focus the bunch on either the TDS resonator gap or on the forward screen for e.g. a profile or emittance measurement.

1.1.3. Quadrupole

One quadrupole is installed before the TDS chamber. It can be powered to yield a field gradient of up to $G = \pm 0.3385$ T/m. As common in the field of accelerator physics and explained in various books like [18] the field gradient usually is expressed as a multipole strength $k1 = e/p_0 * G$ and reaches up to 20 1/m^2 for a bunch momentum of $p_0 = 5$ MeV/c. For the low energy section this gradient is strong enough to reach even over focusing until the beam screen stations.

In the experiment, the quadrupole is used for the emittance measurements [19]. By monitoring the bunches reaction on different quadrupole strenghts, the transverse emittance can be extracted.

In addition, it may be used for an improved vertical focusing during streaking experiments in the future. However, this option could not be tested successfully within the experiments done in this thesis.

1.1.4. Dipole

A dipole is located immediately after the TDS chamber. It serves the purpose of deflecting the electron beam towards the spectrometer arm, which is displayed in fig. 1.1. The dipole is not regarded as an open degree of freedom, it functions as a selector with two states. It eiter has no effect on the bunch and the bunch flies straight through towards the forward beam screen or the spectrometer is powered to deflect the bunch by 30°, guiding it through the spectrometer arm. Due to hysteresis effects, the dipole requires cycling after each use to achieve a field free state.

In the experiment it was used for measuring the energy and energy spread by deflecting it into the spectrometer arm and studying the transverse beam profile via the beam monitor at the end of the spectrometer.

1.1.5. Corrector magnets

FLUTE also features three corrector magnets positioned along the beam path. The first corrector is located after the solenoid, the second before the quadrupole, and the third after the dipole in the forward arm. Each corrector magnet consists of two individual dipoles, one for each transverse plane. Each corrector can induce an angular kick of up to $\alpha_{x,y} = \pm 30.1\,\text{mrad}$.

These kicks play a crucial role in the beam-based alignment processes that was performed in every run of the streaking experiments.

1.2. Diagnostic devices

1.2.1. Charge measurement devices

Two distinct methods are employed for the measurement of the bunch charge: the non-destructive turbo Integrated Current Transformer (ICT) and the destructive Faraday Cup, both are displayed in fig. 1.1.

Turbo ICT: The tubo ICT[3] operates downstream of the solenoid. The ICT is capable of capturing bunch charges up to 3200 pC. The absolute signal to noise ratio ratio is best for low bunch charges and gets worse for increasing charges in a non-linear way, for simplification one can state, that for all charges relevant in this dissertation, the absolute noise level lies below 0.2 pC. The inductance coil within the device detects the induced current and subsequent readout electronics interpret these readings as corresponding to electric charge. Notably, the turbo stands for a specific system that includes an integrated

---

[3] Bergoz ICT-CF4.5"-38.0-40-UHV-Turbo2

band-pass filter within the induced frequency spectrum, thereby the constant dark current is automatically excluded from the short pulse from the bunch charge measurement.

Faraday cup: The second approach involves employment of the Faraday Cup from Radia Beam, installed at the end of both the forward and the spectrometer arm. Central to its design is a cylindrical aluminum plug with a diameter of 26.1 mm and a length of 145 mm. Electric charge captured within this central cylinder contributes to the measurement, including both dark current and beam current. A diffuse or significantly misaligned beam could potentially miss the stopper plug partially, leading to measuring only a fraction of the total charge. Also beam losses during the transport from e.g. the inserted TDS resonator or the beam screens further reduce the measured charge.

Consequently, the absolute charge measurement is consistently conducted using the ICT due to these limitations, as well as the advantageous feature of non-destructive measurement.

1.2.2. Beam screen stations

The beam screen stations (also called profile monitors) reveal the bunch size and shape, their locations are displayed in fig. 1.1. The energy and energy spread are also resolved via the beam profile in the spectrometer arm screen station. Further, the transverse emittance can be extracted from the beam shape, as it changes during a scan of the quadrupole field strength, called a quadrupole scan [19]. Yet most important, the streaking phenomena is revealed too via the profile monitors, rendering them the most essential diagnostic device in the current setup.

FLUTE incorporates three profile monitor stations, positioned within the TDS chamber and at the end of both the spectrometer and forward arm, upstream of the Faraday Cups. A motorized target can be driven into the beam path. Upon interaction with the electron bunch the targets will emit light, which subsequently is observed by an externally positioned diagnostic camera.

Target types and functionality: Both the forward and spectrometer stations are equipped with three different target types:

- A calibration screen, used for the correct pixel-to-size alignment.

- A metal screen that generates Optical Transition Radiation (OTR) for electron energies above 70 MeV[20], yet these energies are not reached within this thesis.

- A scintillation screen made of Cesium doped Yttrium Aluminium Garnet (YAG).

In the TDS chamber only a YAG screen is used. YAG screens prove more effective at lower charge densities and lower energies [20], making them the exclusive choice in this thesis.

Charge density limitations: The light yield of the YAG material can saturate for a given charge density. The actual value depends on multiple parameters such as material age or electron energy. A comparable experiment found a saturation charge density of around $1.5\,\text{nC/mm}^2$ [20]. In the context of this study, the charge density remains an order of magnitude below this critical threshold.

The lower limit of a detectable charge density depends also on the setup of installation. The camera setup, ambient lights and the data processing all play a role. The lower limit in the FLUTE setup was tested out by simply recording low charge bunches with the forward screen station. To do so the solenoid was detuned stepwise 7ufor defocusing the bunches more and more, thereby effectively reducing the charge density on the screen. The implemented control software was able to read out a charge density of up to $1.89\,\text{pC/mm}^2$. By limiting the camera field of view to a Region of Interest (ROI) around the bunch impact, the charge density limit can be pushed further down to $0.26\,\text{pC/mm}^2$, before the camera readout saturates. Since a bunch with lower charge is easier to focus, the lower limit will be of interest later.

YAG screen falsifications: A YAG screen is subject to several systematic uncertainties: Multiple scattering within the material leads to a luminous corona effect and with that an increase of the detected image size. The material thickness of $200\,\mu\text{m}$, combined with the $45°$ rotation around the y-axis, causes a $283\,\mu\text{m}$ travel distance through the YAG screen, which subsequently becomes illuminated and results in a horizontal smearing of the image.

Multiple publications [21, 22, 23, 24] discuss the systematic falsifications of an electron profile measurement with a YAG screen and find dependencies on several beam parameters (energy, charge, size) on the screen thickness and the screen and camera angles.

Although no publication covers the parameter regime of FLUTE, an assumption could be extrapolated from the publications. For the purposes of this thesis, a static, systematic overestimation of $40\,\mu\text{m}$ in each profile measurement is assumed [25]from transfering the findings of the mentioned publications onto our setup. However the uncertainties should be investigated further as the high-energy section goes into operation and a cross check with the OTR screens will become possible.

Scheimpflug angle: The targets are positioned at a rotated angle of $45°$ around the vertical axis. A conventional camera setup would suffer from having the screen center in the focal plane, one edge in front of the focus plane and the other edge behind it. To accommodate this angled setup, the camera is installed with the Scheimpflug angle [26], meaning the camera is not placed perpendicular to the viewing axis but slightly tilted off. This configuration effectively aligns the image plane (beam screen) with the focal plane, eliminating image distortion.

Camera system: Each beam screen station uses a camera[4] to observe the screen target from outside the accelerator, the light is transported through a window, a mirror and an objective[5] to the camera's sensor[6]. To prevent CCD saturation, a set of five distinct filters is employed, adjusting the light intensity reaching the sensor. The filters can be controlled remotely, allowing for their insertion and retraction as necessary. The illumination of a YAG screen decays within 70 ns [27]. The cameras operate at a minimal exposure time of 10 μs, and with that catches all the light emitted. The setups vary slightly, the individual screen resolution is measured with the calibration targets and are 28 μm per pixel for the forward screen, 30 μm per pixel for the spectrometer screen and 13 μm per pixel for the TDS screen. The higher resolution allows to visualize the TDS resonator more clearly which is necessary for a precise alignment.

1.2.3.   Spectrometer

Setup: The spectrometer consists of the 30° dipole described in section 1.1, the spectrometer screen station and in between a drift section with $L_D = 0.609$ m. The dipole and the angled spectrometer arm and screen station are displayed in fig. **??**. On identifying the Lorentz force as the acting centripetal force one finds

$$r = p/(Bq) \tag{1.2}$$

with the deflection radius r, the particle momentum p, the magnetic field B and the electric charge q.

As the deflection radius is linearly proportional to the momentum, the bunch spreads in the horizontal plane due to its momentum spread,. Upon exit of the sector dipole, the bunch is therefore divergent and spreads further by traveling through the drift section.

Mean momentum measurement: In order to measure the mean momentum of the bunch, the center of the charge distribution in the screen image has to be identified. By adjusting the electric current that powers the dipole, the bunch can effectively be shifted horizontally over the YAG screen and with that it becomes aligned with the screen center. This ensures a deflection of 30° and equ. 1.2 can be applied to calculate the mean momentum.

A prerequisite of this method is a beam alignment without offset or angle at the spectrometer entrance. This can be achieved by a beam based alignment procedure.

---

[4] Basler acA1300-60gm camera
[5] Nikon PC-E Micro Nikkor 85mm 1:2.8D objective
[6] CCD sensor with 1282 × 1026 pixels and 12-bit depth

Momentum spread measurement   Unfortunately, precise measurement of the momentum spread is not straightforward. The momentum spread is derived from the beam width at the spectrometer screen.

A potential solution to this issue could involve transforming the horizontal axis of the screen, such that each screen position corresponds to a unique momentum value. The charge distribution on the screen could then be interpreted as the momentum distribution. However, due to the finite bunch size and divergence, this approach holds only in a first-order approximation. This concept is discussed in detail in the appendix A.3.

Nonetheless, it is feasible to conduct a simple measurement to determine the lowest and highest momenta within the bunch. For this, the momenta of both horizontal ends of the distribution are measured by shifting them to the screen center as discussed for the mean momentum measurement before. This directly gives insight into the momentum range. Also the charge profile can be mapped with a minimum and maximum momentum and a spread can be estimated.

The single measurements are especially accurate since the bunches follow the design path. Yet this procedure requires at least two additional measurements of subsequent bunches, therefore this measurement accuracy is limited by the machine shot to shot stability.
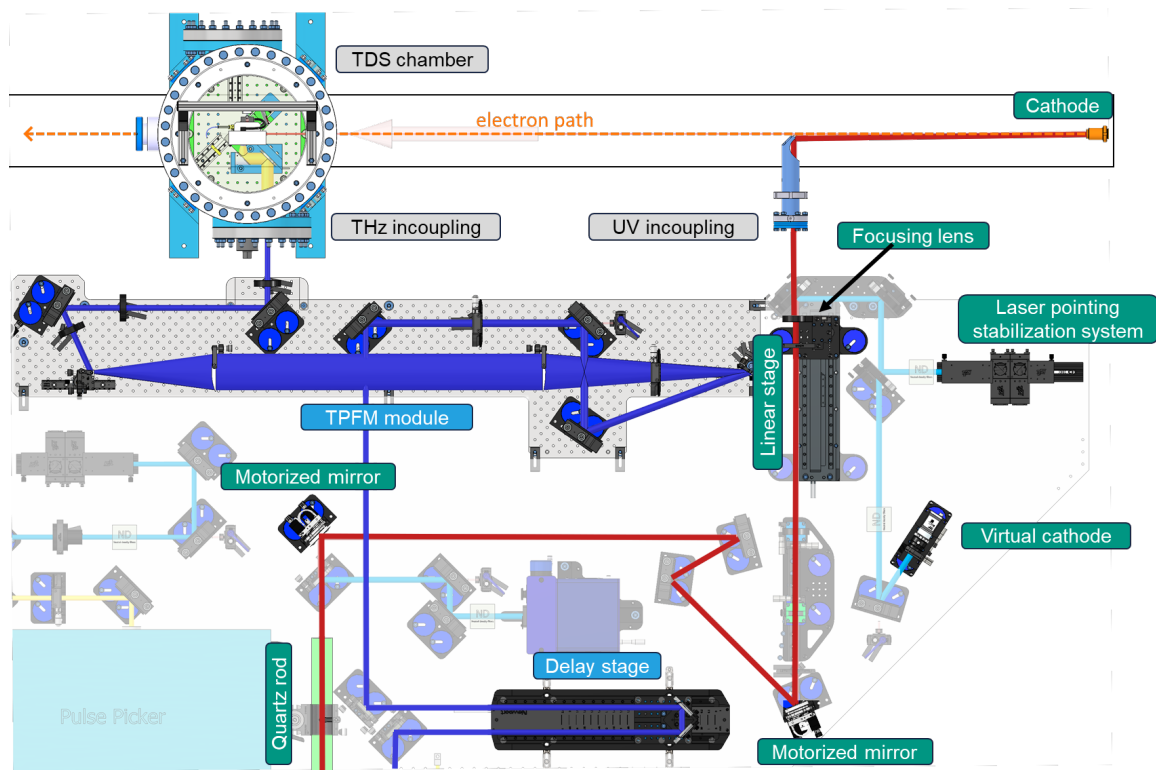
Figure 1.6.: Selection of actively used components in the two laser arms, the UV arm (green labels, red line) and the THz arm (blue labels, blue line). Both arms end with a window for incoupling into the accelerator. Figure based on a CAD drawing from S. Schott, IBPT.

1.3. Laser system

The FLUTE laser system is a vital part of the electron generation but also directly for powering the TDS streaking experiment. The complete system starts in the clean room with a single, pulsed infrared (IR) laser source. This main laser emits pulses that are transported over around 30 m to the experimental hall where FLUTE is located. Upon reaching the optical table next to the accelerator, the laser beam is divided into two distinct branches. The first branch is devoted to the conversion into UV pulses, which are used for the generation of the electron bunches. The second branch is responsible for powering the Terahertz (THz) experiments. This configuration inherently ensures synchronization between the electron bunches and the THz experiments. Further fine tuning is possible through the utilization of a motorized delay stage situated within the THz arm.

Figure 1.6 illustrates the final stages within the two laser arms. Specific components have been highlighted: the THz arm's elements are labeled in blue and the UV arm's elements in green.

1.3.1. THz arm

The THz pulses are generated using a Tilted-pulse-front modulation (TPFM) module. This module has been optimized specifically for the purposes of the TDS streaking experiment [28, 29]. These THz pulses then enter the experimental chamber of the TDS setup through a glass window and excite TDS resonator. The properties of the thereafter created EM streaking field within the resonator depend on the THz pulse characteristics. The discussion concerning the THz pulse is interwoven with the discourse on the streaking field in the subsequent chapter (2).

1.3.2. UV arm

The UV pulse is necessary for releasing the electrons via the photoelectric effect from the cathode. Along it's optical path, the UV pulse is modified by multiple components that influence the pulse parameters beyond the mean of transporting it. Most of the controllable components are highlighted in fig. 1.6 and discussed hereafter.

Pulse power: The share of power transmitted into the UV arm can be tuned by an attenuator at the beginning of the optical table (not displayed in fig. 1.6). A rotating $\lambda/4$-wave plate allows to set the power, up to 17 μJ on the cathode surface. This power would be enough to damage the cathode if focused to a small spot size, the limits for safe operation are discussed in the appendix A.1.

Currently, live monitoring of the power has not been implemented. However, a reference measurement correlates the configured attenuator position with a predefined reference value.

Pulse length: A mount for the installation of a quarts rod is located in the optical path. The high optical density of quartz introduces a dispersive frequency-depending delay. This effectively stretches the pulse depending on the rod length.

A longer pulse creates also a longer electron bunch and thus spreads out the charge over a larger volume. This reduces the destructive space charge effects that limit the possibilities of focusing the bunch into the spatially limited streaking field. Therefore the longest available quartz rod with a length of 330 mm was chosen for all discussed experiments. This choice stretches the UV pulses to the maximum available length of 2.31 ps (FWHM).

Transverse spot size: The pulse cross section directly equals the surface area where charge is released from the cathode. Therefore the spot size determines the initial electron bunch size and with that also the density of the charge that eventually leads to the initial bunch divergence due to the repelling space charge effects. Hence the spot size is one major factor influencing the entire beam dynamics in the accelerator.

The transverse pulse size can be tuned via the position of the final focusing lens, located right before the UV incoupling window. The lens is mounted on a motorized linear stage. With this tool, the spot size can be adjusted between the lower limit with $\sigma_{\mathrm{hor}} = 47.7\,\mu\mathrm{m}$, $\sigma_{\mathrm{vert}} = 45.1\,\mu\mathrm{m}$ and the upper limit of $\sigma_{\mathrm{hor}} = 130\,\mu\mathrm{m}$, $\sigma_{\mathrm{vert}} = 210\,\mu\mathrm{m}$. What stands out is the ellipticity of the pulse, which reverses by moving the focusing lens. This effect probably occurs from astigmatism by trespassing the final focusing lens off-center. The elliptic laser spot causes an suboptimal, elliptic electron bunch, yet the small extend does not yield an actual problem in the experiment.

The spot size can be monitored live with the so-called virtual cathode. Right in front of the incoupling window a 90/10 beam splitter is installed that inserts 90% of the power into the accelerator and onto the physical cathode. The remaining 10% are transported for the same optical path length and lit on an illuminating screen, that is called virtual cathode. A camera observes this screen and gives insight into the spot size, shape and position on the real cathode.

Spot position: Finally the spot position can be fine adjusted. Therefore two mirrors, each with a motorized pitch and yaw axis to control the pulse elevation and azimuth direction are utilized. This allows to offset the pulse horizontally and vertically and compensate the therefore introduced angles. The spot position is also monitored via the virtual cathode.

1.4. TDS chamber

The TDS chamber is the location where the TDS streaking, the primary experiment of this thesis is conducted. This chamber has previously been presented in the context of the adjacent accelerator components (see fig. 1.1) and in conjunction with the surrounding laser equipment (see fig. 1.6). In the current discussion, we delve into the interior of the chamber, providing an inside view as depicted in fig. 1.7.

1.4.1. Coordinate System

Throughout this thesis, a consistent coordinate system is maintained, as introduced at the beginning of this chapter. Given the evident intersection of the electron beam and the THz pulse within the TDS chamber, in addition with the presence of various motor axes oriented in different directions, this aspect is reiterated for clarity.

Explained with the specified directions in fig. 1.7, the uniform axes are as follows:

- The x-axis is aligned horizontally and follows the "CH5" motor axis. "CH5" shifts the aperture plate together with the "CH4" motor.

- The y-axis is aligned vertically and follows the "CH2" as well as the "CH4" direction.
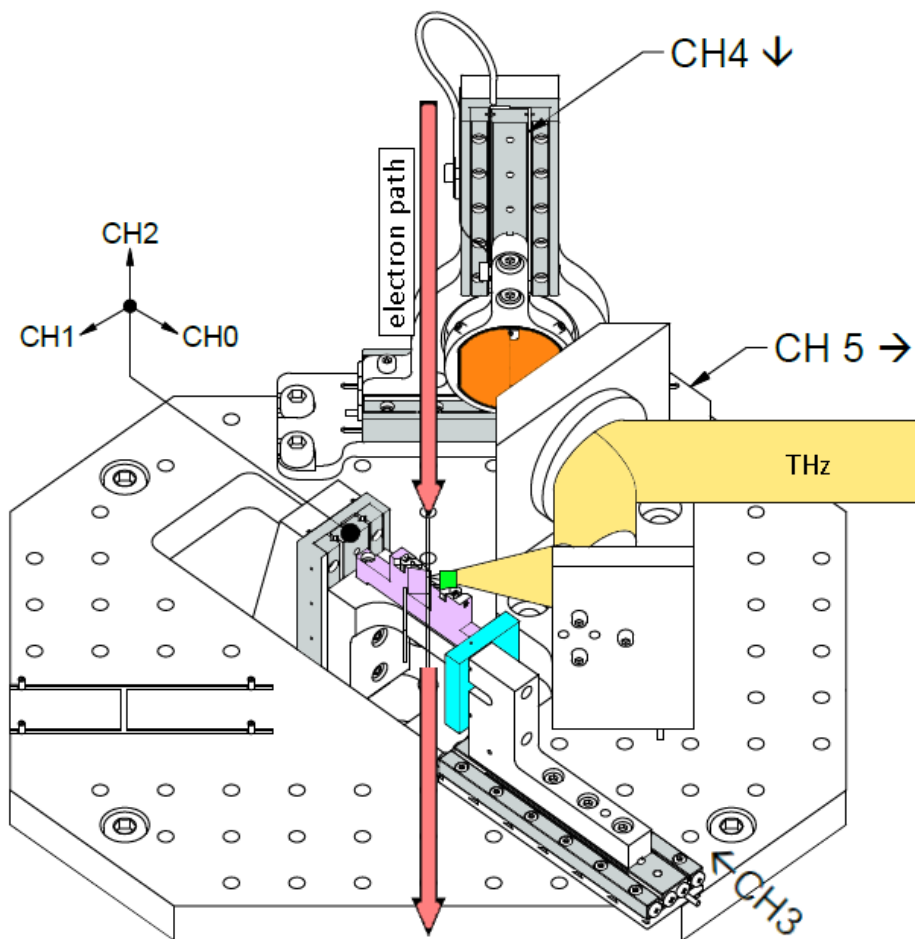
Figure 1.7.: motor stages (gray) with the indicated motor channel name "CH1" to "CH5". thz pulse (yellow) aperture plate (orange) electron path (red) holder (pink) for TDS resonator (too small for depiction) and YAG screen (green) mirror (blue). Figure based on a CAD drawing from S. Schott, IBPT.

- The z-axis is oriented longitudinally and follows the electron path indicated by the red arrow.

1.4.2. Aperture

A copper plate featuring apertures of varying sizes is affixed to a motorized holder, as illustrated in fig. 1.8. The different apertures span diameters between 1.5 mm and 50 μm. Two stepper motors, framed as CH4 and CH5, facilitate horizontal and vertical movements of the holder, enabling precise alignment of the desired aperture with the beam axis or removal of the entire structure out of the beam path. The 5 mm thick copper plate completely blocks a 5 MeV electron and thereby eliminating excess particles.

The aperture was employed to define the position and dimensions of an enlarged electron bunch and thereby mitigating shot-to-shot variations in the beam.
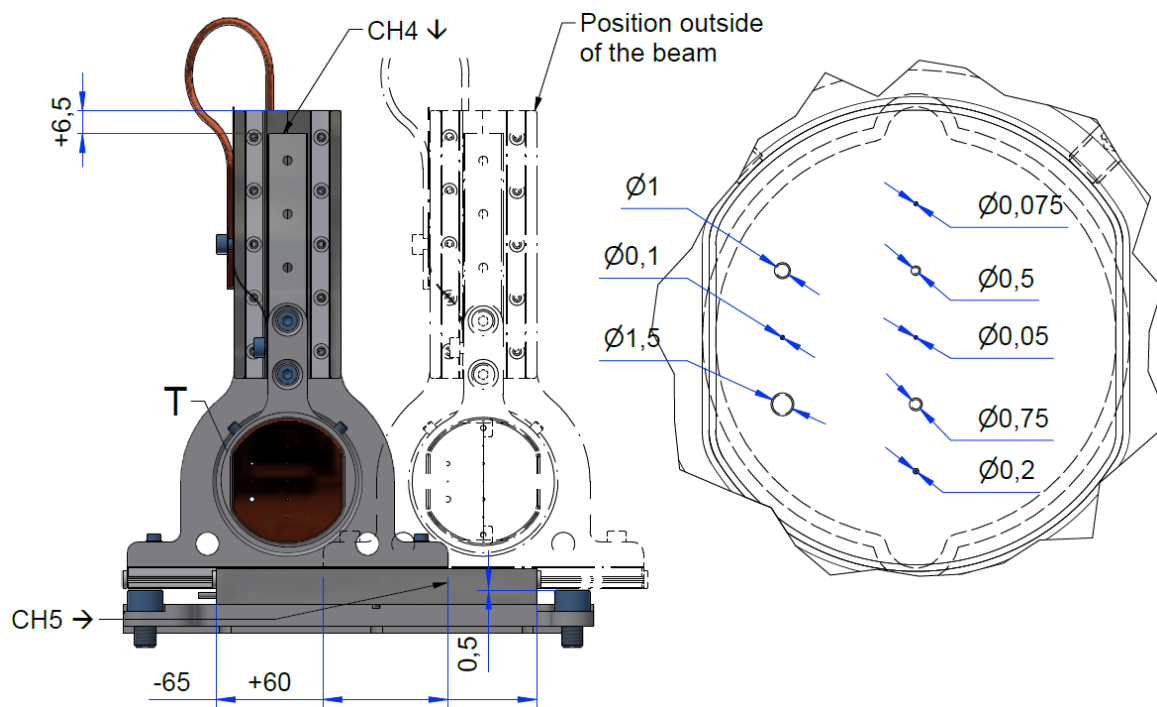
Figure 1.8.: Technical drawing of the aperture (right) and its holder (left), dimensions in millimeter. The holder is motorized to move in the vertical (CH4) and the horizontal axis (CH5). The 5 mm thick copper plate holds aperture holes with different diameters between 1.5 mm and 50 μm. CAD drawing from S. Schott, IBPT.

1.4.3. Diagnostic imaging system

The TDS chamber is equipped with a beam screen station similar to the screen stations detailed in section 1.2.2. The camera setup offers a resolution of 13 μm per pixel.

Mirror: The camera's field of view is aligned with the direction of the beam pipe through the use of a mirror and is depicted in fig. 1.7 in blue. Motor CH3 allows the retraction of this mirror, thereby modifying the camera's field of view and also shifting its focal plane. Additionally, the mirror has a hole that serves as an additional aperture, although it remained unused within this thesis. However it is visible in several of the following images.

SRR and YAG Screen: The holder for the Split-Ring resonator (SRR) and a YAG screen is shown in fig. 1.7 in purple and the YAG screen is depicted in green. The SRR finds itself also on the holder directly in the electron beam path but it is too small to be visible in this image. The holder is movable alogn three axes, driven along the motor axes CH0, CH1, and CH2. In conjunction with the retractable mirror, the SRR and also the YAG screen can be positioned on the electron path within the camera's focal plane.
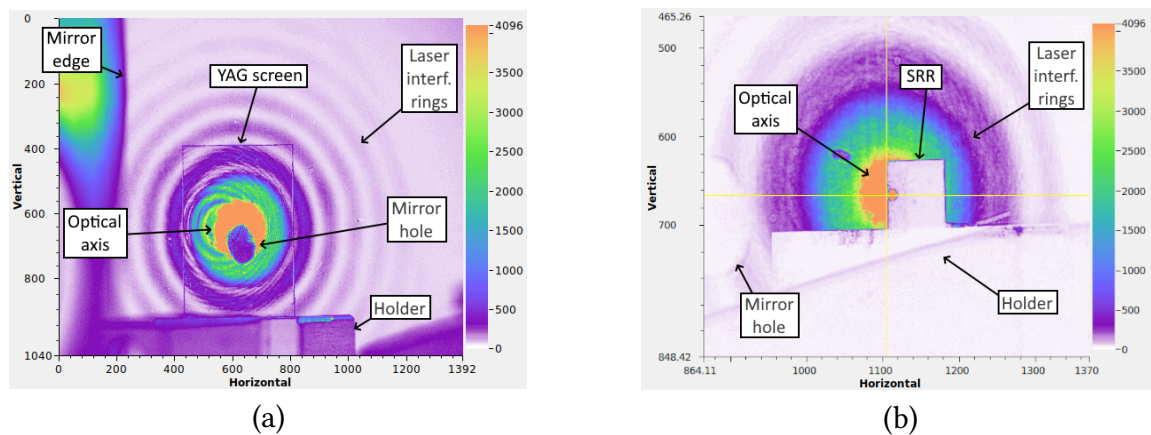
Figure 1.9.: TDS diagnostic camera targeting a) the YAG screen and b) the Split-Ring resonator. The field of view covers also the holder of both items, the hole in the mirror and in case a) also the edge of the mirror. The image was created during alignment with a visible alignment laser, the laser center and interference rings are visible.

Both the SRR and the YAG screen are captured by the camera, as demonstrated in fig. 1.9. These images were generated during an alignment procedure in which an optical laser was projected along the beam pipe. The laser axis together with the surrounding interference pattern illuminate the images prominently. Additionally, the mirror hole and the SRR holder are visible in both images, and even the edge of the mirror can be seen in subfigure (a). The SRR and its circular cutout are visible in subfigure (b), while the 20 µm gap is not resolved.

1.4.4. Split-Ring resonator

This initial layout of the Split-Ring resonator (SRR) was designed and manufactured by T. Feurer and Z. Ollmann[7].

Position: The resonator itself is mounted such that it can be driven out of the electron path or into the Interaction Point (IP). The IP is the design position, where the electron path crosses the resonator gap where the streaking field is centered around. Aligned to this IP is also the introduced THz pulse that drives the resonator to build the streaking field.

Dimensions: Multiple different THz resonator designs are possible. The specimen tested at KIT is designed in the so called Split-Ring resonator geometry[8], it is displayed in fig. 1.10

---

[7] Prof. Dr. Thomas Feurer and Dr. Zoltan Ollmann, Institute of Applied Physics - University Berne, Schwitzerland

[8] In some publication this design is also called inverse Split-Ring resonator (iSRR).
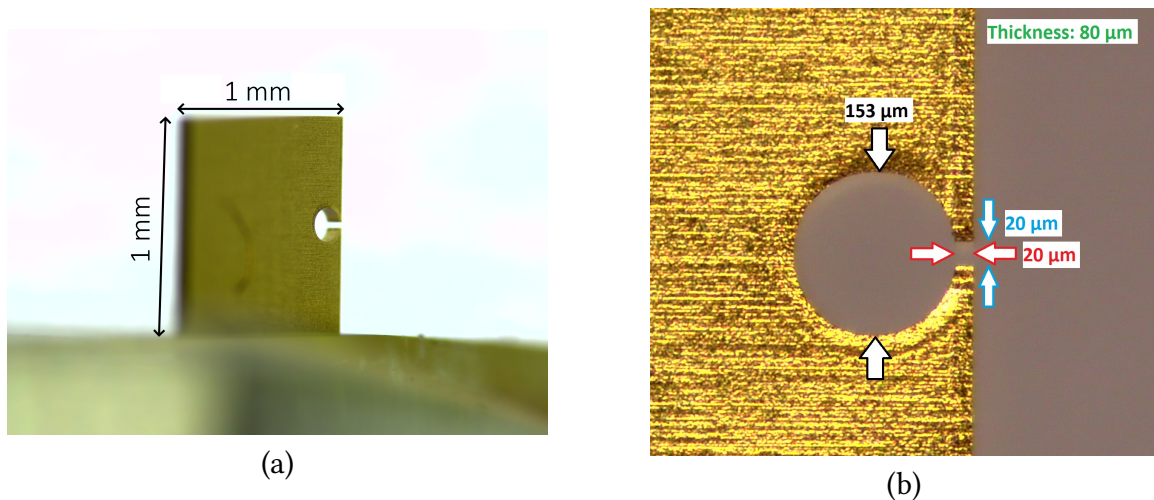
Figure 1.10.: Resonator geometry, a) shows the full resonator body, recorded with a light microscope by M. Nabinger and b) a zoom onto the gap region.

Table 1.1.: SRR geometric properties

| Parameter	value	unit
Length	1000	μm
Depth	80	μm
Gap height	20	μm
Gap width	20	μm
Cutout diameter	153	μm

and its dimensions are summarized in tab. 1.1. This design produces the highest field strengths, for the sake of simplicity, omitting the stacking of multiple resonators.

Here the streaking field is restricted into the tiny $20\,\mu m \times 20\,\mu m$ gap, the field properties are discussed in the following chapter. Electrons that miss the gap and collide with the material are basically lost as discussed in the following.

Collision with the resonator: It is inevitable that parts of the electron beam will collide with the resonator body. The physical effects involved in this phenomenon were investigated in collaboration with A. Ferrari[9], using the simulation software Fluka [30]. The study is extensively discussed in the appendix A.2.

The conclusion of the study is as follows: Electrons that strike the resonator body pass through it and undergo scattering. The scattering distribution has a $1\,\sigma$ width of 81 mrad, which is significantly larger than typical divergence values of below 20 mrad in the drift section after focusing on the SRR. Consequently, colliding particles, due to their significant

---

[9] Alfredo Ferrari, IAP & IBPT - Karlsruhe Institute of Technology
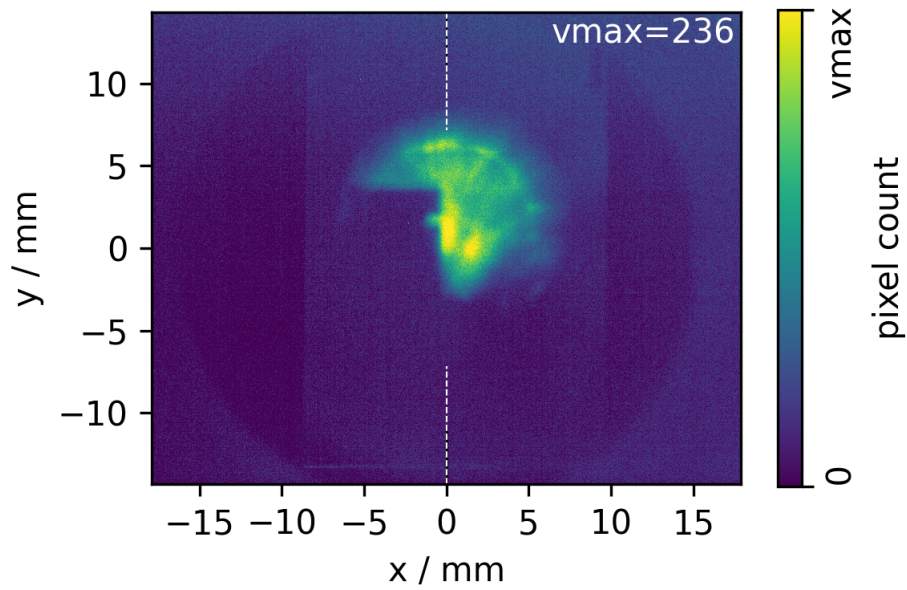
Figure 1.11.: YAG screen image of the electron bunch with the resonator shadow visible. The shadow is a result of the scattering of electrons flying through the resonator material. The color map upper limit, vmax, is set to the 99.9 % quantile of all pixel counts in this image.

scattering will contribute to the background, effectively forming a shadow created by the resonator body.

These findings are supported by actual experimental YAG screen images, where the impression of the resonator is clearly visible, as shown in fig. 1.11. This screen image is taken from the later explained *brightness* experiment, where it will be displayed again.

2. TDS - model and application

This chapter formulates generic expectations on the TDS experiment at the FLUTE setup. The experimental working principle is sketched in fig. 2.1. The electron bunch is focused and threaded through the SRR gap, where the streaking field is located. While traveling through the SRR gap, the electrons experience the oscillating streaking field, resulting in a vertical kick on the electrons. Synchronized correctly, the bunch center will pass the streaking field in the oscillation's zero crossing. Then the bunch head experiences a downwards force and its tail an upwards force. Subsequently, after passing the SRR gap, the bunch traverses a 1 m long drift section. The drift length is required for the bunch to evolve a vertical spread from the kick. The so streaked bunch finally reaches the scintillating YAG screen, where the bunch length can be measured from the streaked bunch height.

The impact of the streaking field on the electron bunch, and consequently the measurement resolution, is determined by the streaking field amplitude and frequency. Due to
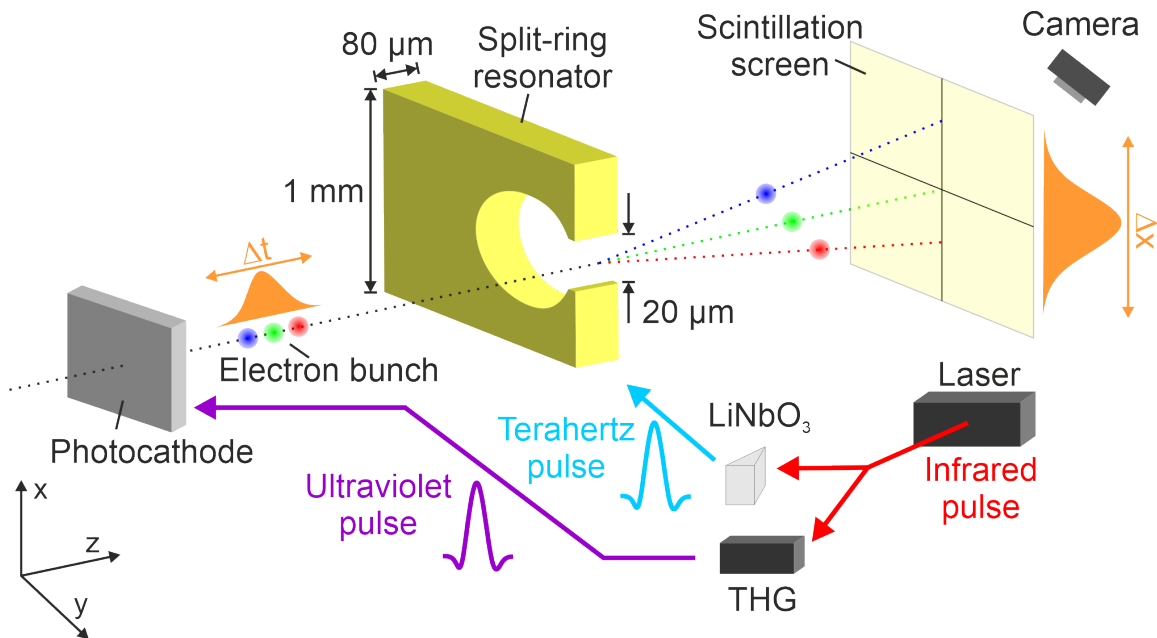
Figure 2.1.: The principle of the bunch length measurement with the SRR. The electrons are focused on the SRR gap. Simultaneously, the "drive" laser creates a THz pulse that powers the SRR. The resulting streaking field kicks the bunch head downwards and the tail upwards. The streaked image on the scintillating screen contains then the information of the bunch profile. Illustration from M. Nabinger, IBPT, adapted from [6].

the streaking field's spatial confinement within the tiny resonator gap, a direct measurement of the field properties is technically not possible. However, its properties can be computed by analyzing the THz pulse that excites the field and considering the resonator characteristics.

The electro-magnetic field in the incident pulse front with a peak frequency of 258 THz moves the electrons within the resonator body. The resonator's c-shape is designed such, that electrons group on one side of the slit geometry. The gap surfaces act like a parallel plate capacitor with C_{gap}, building up the electric streaking field inside in between them. As the THz pulse's electromagnetic wave oscillates, electrons traverse the resonator surface and group up on the opposing gap surface, causing an inversion in the streaking field polarity. The corridor wherein the electrons travel acts similar like an inductance L. With that, the scenario describes an oscillating system with an eigenfrequency f expressed analogously to a regular LC-circuit:

$$f = \frac{1}{2\pi\sqrt{LC}} \tag{2.1}$$

The description of the SRR resonator as an LC-circuit, the derivation of L and C_{gap} and additionally a capacitance contribution from the surface is detailed in [31].

In reality, the THz pulse excites the system not solely with the resonator's eigenfrequency but with a spectrum, leading to a spectrum in the streaking field. A Computer Simulation Technology Studio Suite (CST) simulation allows to compute the EM-dynamics considering the pulse spectrum. The CST simulation was carried out by our collaborative partner, S. Glukhov[1]. The simulation solves the Maxwell equations in temporal steps of 20 fs for each grid point within a sufficient large volume, utilizing a dynamic, hexahedral mesh. The volume covers a margin around the resonator of ±2 mm in x, y and z. The grid spacing was set to 13 cells per wavelength. The excitation signal was modelled as a plane wave, sweeping through the simulation region, with a temporal Gaussian structure. This simplification is valid as the resonator is positioned within the pulse waist where the pulse front propagates similar to a plane wave.

The modeled field characteristics depend upon the resonator geometry, as detailed in the preceding chapter, and the properties of the incident THz pulse, this topic is discussed in the upcoming section 2.1. The influence of the streaking field on the electron bunch follows in section 2.2 followed by the measurement limits and resolution in section 2.3.

2.1. Modelling of the streaking field

The streaking field of the SRR is represented with a simulated, complex model. This model comprises the temporal evolution of both the real and imaginary parts of the 3D vector field for the electric (E) and magnetic (B) components.

---

[1] Dr. rer. nat. Sergei Glukhov, TEMF - Technical University Darmstadt, Germany
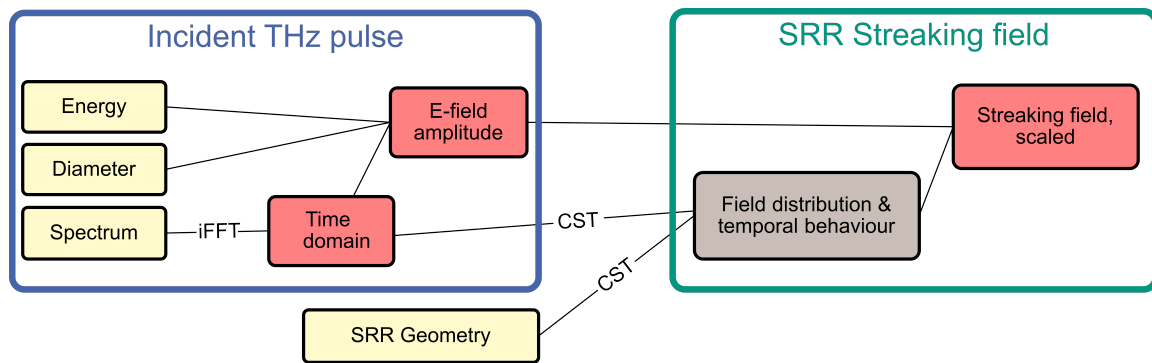
Figure 2.2.: Dependencies of the streaking field model, showing relations between measurements (yellow), calculations (red) and simulations (gray).

The necessary steps for modeling the field are illustrated in fig. 2.2. The measured parameters (yellow boxes) act as the basis for calculations (red) and the CST simulation (gray) [32]. Certainly, a project of this nature is not a solo endeavor. The tasks within the yellow boxes were primarily executed by M. Nabinger[2], whom I had the opportunity to assist. The content of the gray box was contributed by S. Glukhov.

The discussion starts with characterizing the incident THz pulse (blue block) in section 2.1.1. With that the actual streaking field can be modeled (green block), the model is discussed in its different aspects in section 2.1.2.

The aforementioned discussions are based on our current experimental geometry, which has been thoroughly tested in the laboratory. The streaking field properties are a direct outcome of this specific discrete geometry. The effects of an altered geometry on the field are discussed in section 2.1.3.

A direct measurement of the streaking field is technically challenging due to the limited spatial field distribution within the SRR gap. The size of THz antennas prevents their placement within this confined volume. Although various experimental techniques have been considered to indirectly measure the field, they could not be implemented within the time frame of this study.

2.1.1. Incident THz pulse properties

The goal of this section is to compute the E-field amplitude of the THz pulse, wherein, to put it simply, the pulse energy is related to the pulse volume. Determining the spot diameter and length involves interpreting these quantities from a measured, continuous distribution. The energy on the other hand can be completely measured using a probe.

Among the various options available for defining the size of a distribution, the $1/e^2$ measure is used in this chapter. It is equal to the distance of the two points, where a gaussian-like

---

[2] M.Sc. Matthias Nabinger, IBPT - Karlsruhe Institute of Technology

distribution falls below $1/e^2$ of the maximum value. This choice appears to be a reasonable compromise between counting in the vast amount of the pulse and not beeing falsified by long, less stable tails of a distribution. Further, this measure provides a good coverage for a spectral measurement, as emphasized in the dedicated spectrum discussion.

2.1.1.1. Energy measurement

For the measurement of the pulse energy U, the SRR was replaced with an energy sensitive probe, that measured a pulse energy of $U_1 = 142\,\mathrm{nJ}$ with an estimated uncertainty of 10%, taking into account the measurement fluctuation and the uncertainty of the measurement device. As the probe was placed on the resonator position, the losses from the transport optics and the incoupling window have been inherently included. Yet the measurement was conducted in the experimental chamber filled with air, where the streaking experiment takes place in vacuum. The decrease in power due to air absorption can be determined using the Lambert-Beer law [33]:

$$U_1 = U_0 e^{-\alpha d} \tag{2.2}$$

where U_1 represents the reduced power and $d = 0.215\,\mathrm{m}$ the transport distance. The absorption coefficient α for our THz pulse was measured by Matthias Nabinger [28]. Under laboratory conditions with normal air pressure and a relative humidity of 40%, an absorption coefficient of $\alpha = 0.87 \pm 0.32$ was found. Using the above equation, the pulse energy U_0 can be calculated (without attenuation by air losses) to

$$U_0 = (171 \pm 21)\,\mathrm{nJ}\,. \tag{2.3}$$

The given uncertainty incorporates the combined uncertainties from α and the power measurement

Recent developments at KIT showed great potential of reducing the huge transport losses of the THz pulse energy with in-house manufactured new
optics made of Ultra-high-molecular-weight polyethylene (UHMWPE). It could be shown, that a change to such an optics and an additional dehumidification of the TPFM setup does lead to an increase of the pulse energy at the SRR position of 88 % ± 40 % [34].

2.1.1.2. Laser spot size measurement

In order to measure the pulse diameter, the THz energy meter from the previous measurement was utilized again. To enhance spatial resolution beyond the detector's 10 mm diameter, we introduced an iris aperture into the resonator plane and positioned the energy probe behind it. Subsequently, we utilized the XYZ stage to maneuver the iris and probe combination, allowing us to map the energy distribution.

The smallest iris available had a diameter of 1.4 mm, which proved to be sufficient for the task at hand. In fig. 2.3 two representative profiles, covering the power distribution in the resonator gap position are shown. The pulse is shown in the electron beam coordinate
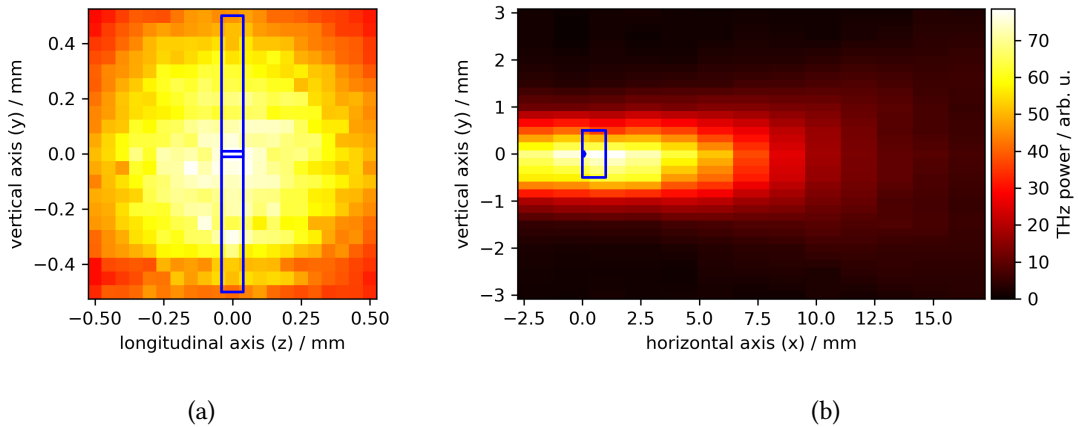
Figure 2.3.: Spatial THz power distribution at the SRR position with respect to the IP (0,0,0), shown in the electron bunch coordinate system. This was measured with the energy meter mounted on the XYZ motorstage. The outline of the SRR profile is shown in blue.

system, the horizontal axis therefore is parallel to the THz pulse direction. Subplot a) shows the pulse power distribution in the z-y plane, with $x = 0$ m, the horizontal position of the SRR. Subplot a) shows the power distribution in the x-y plane, with z beeing the longitudinal position of the SRR. The SRR position is visualized in both plots by the blue sketch.

To determine the pulse horizontal (x) and vertical y diameter, 1-D Gaussian fitting was performed on the measured data projected onto each axis.

$$x = (2112 \pm 22)\,\mu m\,; \quad y = (2040 \pm 20)\,\mu m \tag{2.4}$$

The uncertainties originate from the fitting algorithm.

The transverse measurement shown in fig. 2.3 reveals a slight change in intensity within the vertical plane at around $y = -0.4$ mm. The cause of this sudden shift remains unclear, but it has no significant impact on the final result.

2.1.1.3. Spectrum measurement

The temporal shape of the incident THz pulse is an important property that is required to obtain all properties of the expected streaking field, as shown previously in the overview graph, recalling fig. 2.2. The temporal pulse shape can be measured directly and very precise with an Electro-optical (EO) setup. Such an EO setup is foreseen for diagnosing various signals in the FLUTE laser system and is right now in the planning phase.

However, it is also possible to deduce the temporal shape from the pulse spectrum using an Inverse fast Fourier transform (iFFT). A basic spectrum measurement was performed by M. Nabinger by employing multiple Band pass filters and recording the remaining pulse energy. The primary objective of this initial measurement was to approximate the pulse

resonance frequency and not to provide a detailed profile, therefore a quick and simple measurement was sufficient.

Yet this measurement found another application. The CST simulation of the streaking field depends on a detailed spectral shape. In order to properly interpret the spectrum measurement, the filter's individual transmission widths and heights have to be addressed. The broad band pass filters transmit leakage power from frequencies beside the design frequency, leading to a systematic bias due to an overestimation of the power and a distortion of the spectrum. Therefore a careful analysis of how the employed Band pass filters had affected this measurement follows.

Measurement principle: To measure the spectrum, THz filters were utilized and the remaining power was recorded with a power meter. Each filter modulates the signal s with its frequency dependent transmission function $T(f)$. The modulated signal can by calculated by a convolution with the signal given in the time domain $s(t) * T(f)$ or respectively with a simple multiplication in the frequency domain $s(f) \cdot T(f)$ [35]. This discussion is held entirely in the frequency domain. The power meter collects the modulated signal and measures the integrated, remaining pulse power. For a correct measurement interpretation, the true signal was unconvoluted from the measured signal as discussed in this section.

Filters: Eight broad Band pass filters were used for this measurement, each with a different spectral width and transmission curve, as shown in fig. 2.4 [3]. The spectral width of the filters vary widely between 31 GHz and 196 GHz (Full width half maximum (FWHM)). This inhomogenity lead to individual distortions in every measurement point.

Raw measurement: Eight data pairs were measured, consisting of the design frequency F_i of the i-th filter, the measured power p_i as well as a statistical uncertainty from recording over several pulses. The raw data are shown in fig. 2.5 (black).

It is worth mentioning that the second-to-last data point (800 GHz) exhibits a significantly large uncertainty. This is because the laser cooling failed during that measurement and the slowly heating laser experienced increasing fluctuations in power. The last data point (1000 GHz) disappeared completely into the noise, resulting in a power value of 0, the uncertainty was set to the median of the other measurement noise level. In fact, the results of this section are only marginally affected by this data point.

The following error compensation describes the creation of a corrected data set $\tilde{p}_i$, it is also displayed in fig. 2.5 (violet). Note, that the error comprehension targets the shape of the pulse, not its absolute scale.

---

[3]   Quasi-Optical THz-Filter and transmission curves from NSU (Novosibirsk)
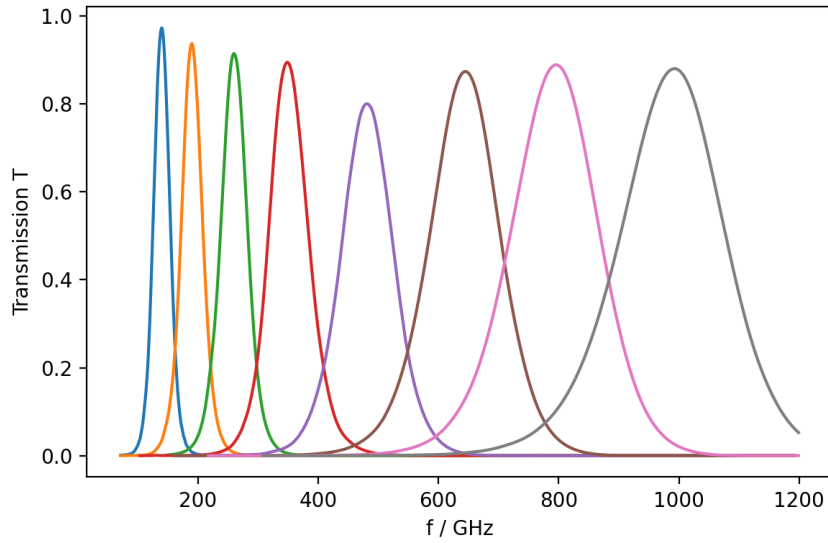
Figure 2.4.: Transmission of the THz filters used for measuring the incident THz pulse spectrum.
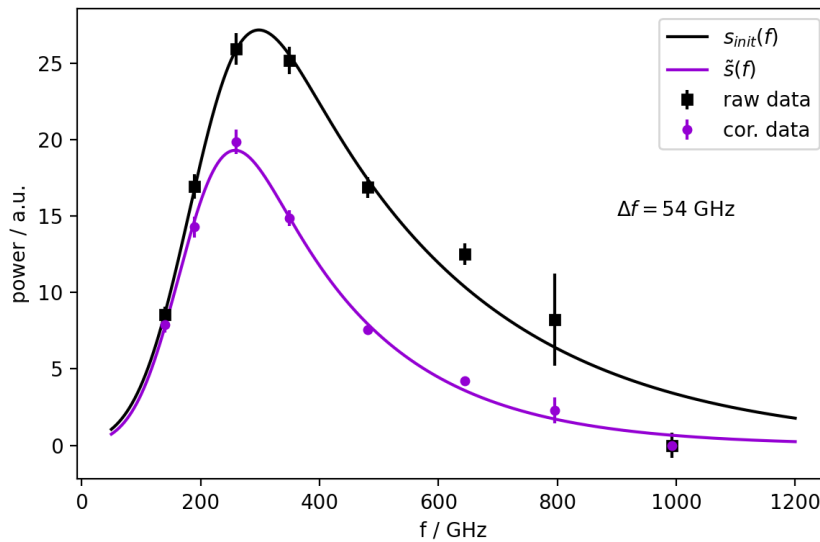
Figure 2.5.: Measured THz pulse spectrum and Exponentially modified Gaussian distribution (EMG) fit for the raw (black) and corrected (violet) data set. The data correction was performed with a frequence window of $\Delta f = 54\,\text{GHz}$.

Spectrum shape: Both discrete data sets shown in fig. 2.5 are complemented by a fitted EMG distribution, $s_{\text{init}}(f)$ (black) and $\tilde{s}(f)$ (violet). The EMG distribution is defined with the complementary error function

$$\text{erfc}(x) = 1 - \text{erf}(x) = \frac{2}{\sqrt{\pi}} \int_x^\infty e^{-t^2} \mathrm{d}t \tag{2.5}$$

as

$$f(x) = \frac{\lambda}{2} e^{\frac{\lambda}{2}(2\mu + \lambda\sigma^2 - 2x)} \text{erfc}\left(\frac{\mu + \lambda\sigma^2 - x}{\sqrt{2}\sigma}\right) \tag{2.6}$$

31
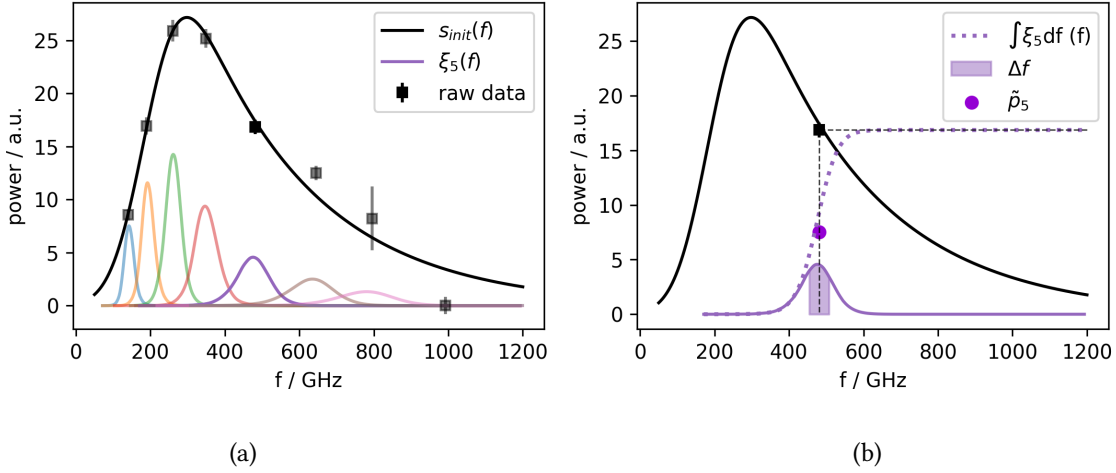
Figure 2.6.: Illustration of the spectrum correction. The raw data and EMG fit (black) and the associated help functions ξ (colored) are shown for all data points in subfigure (a). The correction is shown for the 5-th measurement in subfigure (b). The help function's integral (violet, dashed) is scaled to join the data point level (black, dashed). With a partial integral within the window Δf (violet area) the corrected data point $\tilde{p}_5$ can be calculated (violet, round marker).

with mean μ, variance σ^2 and exponential rate λ. This somewhat complicated function describes in principle the combination of a Gaussian distribution and an exponential decay.

The following correction mechanism requires a shape (instead of single data points), therefore an initial fit on the uncorrected data is performed.

To anticipate the result of the correction, one can already observe here, that the (corrected) data set is very well represented by the shape of such an EMG distribution.

Measurement correction: The principle of the data correction is graphically supported by fig. 2.6, the large amount of details in the figure will clear up throughout this paragraph. The black markers and curves again show the raw data set and the initial EMG fit $s_{\text{init}}(f)$.

For the $i-$th measurement point, the $i-$th filter is placed in front of the probe. The truncated spectrum reaching the measurement probe can be expressed by a help function $\xi_i(f)$ that is the product of the filter transmission curve $T_i(f)$ and the raw data model $s_{\text{init}}(f)$ with a scaling factor A_i:

$$\xi_i(f) = A_i\, s_{\text{init}}(f)\, T_i(f) \tag{2.7}$$

The different help functions are shown in subfigure (a), where the purple curve ξ_5 is carried on into subfigure (b) to illustrate the scaling procedure.

The measured power p_i equals the total power integrated over all frequencies reaching the measurement probe. The integration $\int \xi \mathrm{d}f$ is shown in subfigure (b) (dashed, violet), the correct scaling of ξ merges its integral with the level of the corresponding, raw
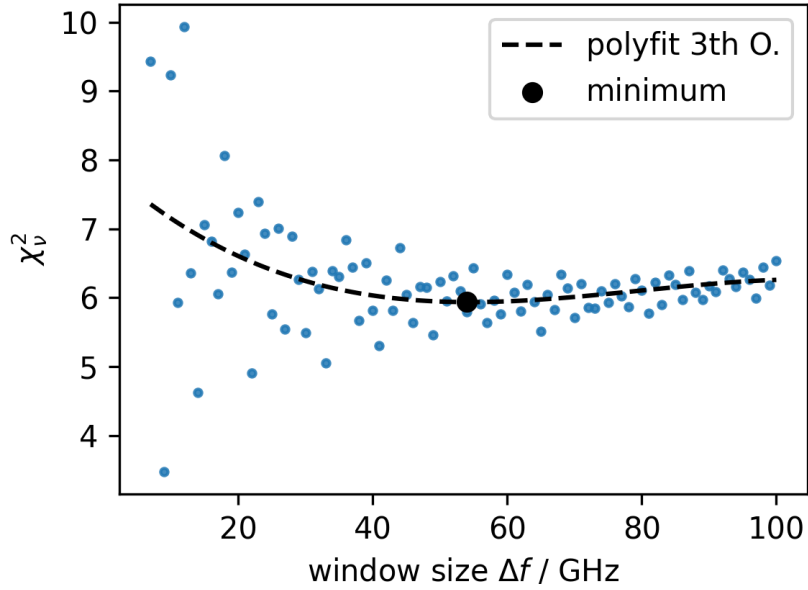
Figure 2.7.: Reduced chi square of the EMG fit on the corrected data set for different window sizes. The 3th order polynomial fit reveals a local minimum at $\Delta f = 54\,\text{GHz}$.

measurement point (black, dashed). The scaling factor A_i can therefore be calculated as follows:

$$p_i = \int_0^\infty \xi_i(f)\mathrm{d}f \tag{2.8}$$

$$A_i = p_i \left[\int_0^\infty s_{\text{init}}(f)T_i(f)\,\mathrm{d}f \right]^{-1} \tag{2.9}$$

The correct scaled help function can now be used to create a corrected data point $\tilde{p}_i$ by integration over a restricted frequency window Δf. This way the individual filter widths can be compensated.

$$\tilde{p}_i = \int_{F_i - \Delta f/2}^{F_i + \Delta f/2} \xi_i(f)\mathrm{d}f \tag{2.10}$$

The integral is represented by the colored area beneath ξ and the corrected data point by the colored, circular marker.

Doing so for the entire data set with one common Δf creates a whole corrected data set and effectively compensates for the falsification from the individual filters widths and transmission.

Decision on the frequency window width: In order to find the ideal window with, this procedure was repeated several times for different Δf. Each repetition yields a new data set and fit result. The agreement between a data set and its EMG model can be
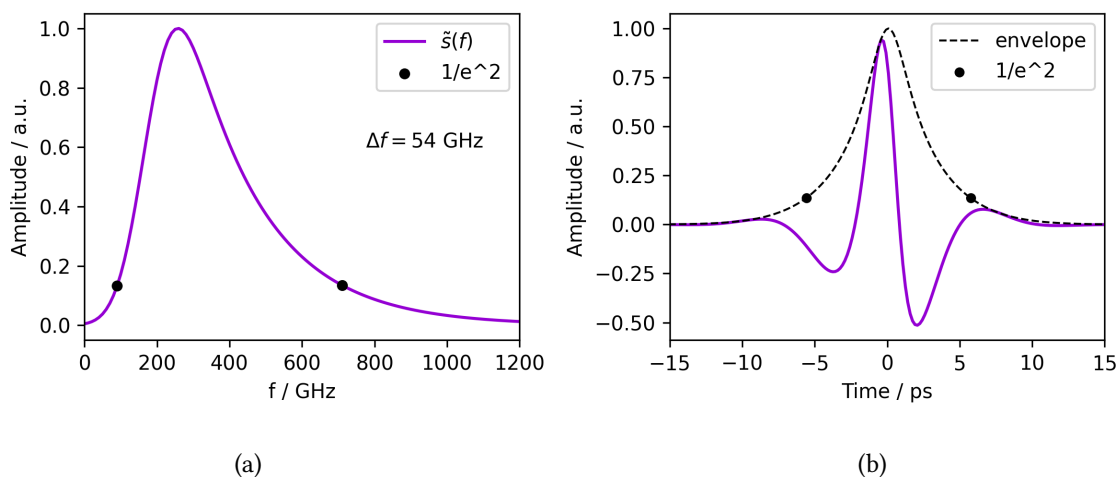
Figure 2.8.: Incident THz pulse spectrum (corrected) on the left, the inverse Fourrier transformed time domain on the right.

quantified by the reduced chi square value χ_v^2 of the fit routine. This χ_v^2 is plotted against the corresponding Δf in fig. 2.7. The ideal window size Δf lies in the minimum of this plot. For the evaluation of this very noisy χ_v^2-Δf plot a simple polynomial fit of 3th order was utilized. This process delivered an ideal window size of $\Delta f = 54$ GHz, this value lies within the actual filter band widths and appears reasonable.

Correction result: The discussed procedure effectively compensates the above mentioned systematic errors of the power measurement and creates a corrected pulse spectrum out of the original, raw data set. Therefore the individual influences of the differently broad filters have been reduced to filters of a common width of 54 GHz. The uncertainties on the corrected data set originate from the statistical measurement uncertainties, corrected by a multiplication with the same factor as the signal correction: $\tilde{p}_i/p_i$. A corrected EMG signal fit $\tilde{s}(f)$ is obtained, it was already shown in the previous section in fig. 2.5. Comparing the raw and the corrected data set reveals some relevant differences: The spectrum peak frequency $\hat{f}$ shifted from 298 GHz in the raw data set to 258 GHz and the spectral bandwidth shrunk from from 874 GHz to 619 GHz ($1/e^2$). The corrected data set and uncertainties are passed on to calculate the THz pulse shape in the time domain.

2.1.1.4. Time domain calculation

The time domain of the THz pulse is computed from the (corrected) pulse spectrum using an iFFT algorithm. The pulse shape in both, frequency and the time domain is shown side by side in fig. 2.8. Actually the iFFT algorithm delivers a complex solution, the presented pulse time domain is only the real part. The pulse envelope is plotted too (dashed, black), it is obtained by the absolute value of the complex solution that can be calculated as follows:

$$\text{envelope} = \sqrt{\text{Re}(E_y)^2 + \text{Im}(E_y)^2} \tag{2.11}$$

The black markers in the figure represent the $1/e^2$ level w.r.t the distribution maximum. Due to the discrete steps in this numerical result, the markers height differ slightly, yet this does not affect the final result in a significant manor. Here the reason behind the $1/e^2$ measure for the pulse dimensions becomes clear. This measure spans closely the spectrum range of the above used filters and therefore is expected to represent best the reality over larger measures that take the less stable, extrapolated distribution tails into account.

For the error propagation, a Monte Carlo method was employed. The (corrected) data points of the frequency domain were randomly modified within a standard deviation based on the (corrected) statistical spread. This process was repeated for a total of $n = 2000$ iterations. In each iteration, the randomized data set was fitted to a frequency spectrum, transformed to the time domain by an iFFT and the envelope was determined as described above. The width of each envelope was calculated, resulting in $n = 2000$ slightly different width values. From this data set, the mean width and standard deviation were computed and the final result is

$$11.39 \pm 0.48 \, \text{ps} \, . \tag{2.12}$$

Integral of normalized envelope square: In the next section the amplitude of the E-field component of the incident THz pulse is calculated. For this a last puzzle piece is still remaining. The integral of the pulse shape in time domain squared is required, it is calculated numerically from the pulse envelope shown earlier in fig. 2.8 with the $1/e^2$ definition.

The uncertainty for this integral is obtained identical as the uncertainties for the time domain over all: a Monte Carlo approach delivered a set of $n = 2000$ integrals, their mean and standard deviation are

$$\int_T E^2_{\text{norm}}(t) \mathrm{d}t := \xi_{int} = 122.6 \pm 4.9 \, \text{ps} \, . \tag{2.13}$$

For the following discussion, this property is framed as ξ_{int}.

2.1.1.5. Calculation of the THz pulse E-field amplitude

The THz pulse can be expressed as a time-dependent EM traveling wave. The peak amplitude of the E-field component is required to calculate the expected peak E-field amplitude in the streaking field. The peak field component of the incident pulse is therefore calculated in the following pages.

In order to estimate the electric field amplitude, we calculate, in figurative terms, the energy density in the pulse by considering the pulse volume.

We consider a time-dependent electric pulse, which is focused so that the field is uniform in the transverse coordinates (x,y):

$$\vec{E}_{\text{THz}}(x, y, t) = \vec{E}_{\text{THz}}(t) \tag{2.14}$$

The energy density $\mathrm{d}U$ per unit volume $\mathrm{d}V$ of the E-field can be described as

$$\mathrm{d}U = \frac{\epsilon_0}{2}\vec{E}_{\mathrm{THz}}(t)^2\mathrm{d}V = \frac{\epsilon_0}{2}E_{\mathrm{THz}}(t)^2\mathrm{d}V, \tag{2.15}$$

with ϵ_0 the vacuum permittivity and $E_{\mathrm{THz}}(t)$ the amplitude of the electric field in time domain. This equation is found in various pieces of literature, for example [14, Chapter 8.1].

The E-field propagates with c and the unit volume can be expressed as

$$\mathrm{d}V = c\,\mathrm{d}t\,\mathrm{d}A, \tag{2.16}$$

where a constant transverse unit area $\mathrm{d}A$ is assumed. The total energy U of the E-field then is

$$U = \int_V \mathrm{d}U = \int_V \frac{\epsilon_0}{2}E_{\mathrm{THz}}(t)^2\mathrm{d}V. \tag{2.17}$$

Inserting equ. 2.16 and integrating over the transverse area A as well as the pulse duration T, the total energy is then

$$U = \frac{\epsilon_0 c}{2}\int_A \mathrm{d}A \int_T E_{\mathrm{THz}}(t)^2\mathrm{d}t = \frac{\epsilon_0 c}{2}A\int_T E_{\mathrm{THz}}(t)^2\mathrm{d}t. \tag{2.18}$$

Further the E-field can be separated into amplitude and a normalized pulse shape, the integral can be rewritten as

$$\int_T E_{\mathrm{THz}}(t)^2\mathrm{d}t = \hat{E}_{\mathrm{THz}}^2\int_T E_{\mathrm{norm}}(t)^2\mathrm{d}t = \hat{E}_{\mathrm{THz}}^2 \cdot \xi_{int}. \tag{2.19}$$

With the horizontal and vertical diameter x, y of the pulse determined in the $1/e^2$ definition, the pulse cross-section leads to an elliptic area of

$$A = \frac{\pi}{4}x\,y \tag{2.20}$$

with that, equ. 2.18 can be solved for the peak electric field in the THz pulse front as:

$$\hat{E}_{\mathrm{THz}} = \sqrt{\frac{8}{\pi\epsilon_0 c}}\sqrt{\frac{U}{x\,y\,\xi_{int}}} \tag{2.21}$$

The uncertainties are treated as independent, they are combined with the variance formula:

$$\delta\hat{E}_{\mathrm{THz}} = \sqrt{\left(\frac{\hat{E}}{2U}\delta U\right)^2 + \left(\frac{-\hat{E}}{2X}\delta X\right)^2 + \left(\frac{-\hat{E}}{2Y}\delta Y\right)^2 + \left(\frac{-\hat{E}}{2\xi_{int}}\delta\xi_{int}\right)^2} \tag{2.22}$$

All numerical values for this calculation have already been introduced, a summary is collected in tab. 2.1. Using these lead to the value for the amplitude of the electric field component in the incident THz pulse as

$$\hat{E}_{\mathrm{THz}} = 0.552 \pm 0.036\,\mathrm{MV/m}. \tag{2.23}$$

Table 2.1.: Calculation values for the E-field amplitude of the incident THz pulse. Used width definition is $1/e^2$.

Parameter		Value	Unit
Energy	U	171 ± 21	nJ
Horizontal diameter	x	2112 ± 22	μm
Vertical diameter	y	2040 ± 20	μm
$\int_T E_{\text{norm}}(t)^2 dt$	ξ_{int}	124.9 ± 5.0	ps

(a)

(b)
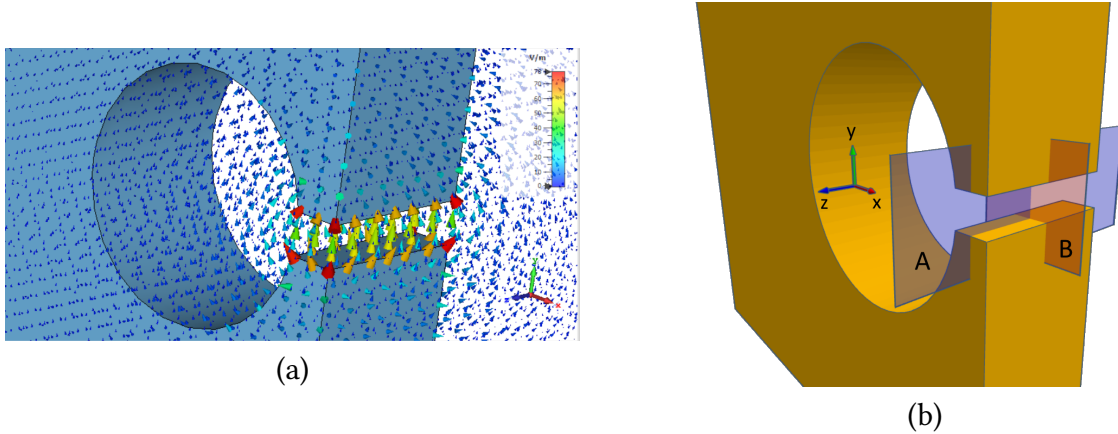
Figure 2.9.: (a)CST simulation result of the EM-vector field in and around the SRR gap. (b) The planes for the cross section 2D field maps.

2.1.2. Streaking field properties

Referring to fig. 2.2, the prerequisites for modeling the streaking field are now complete. A CST simulation was performed by S. Glukhov [36], based on the resonator geometry and the time-domain characteristics of the incident THz pulse. This model comprises both the real and imaginary parts of the 3D vector field for the electric and magnetic complex components. Of course the entire model can be used for calculating the streaking effect on the electron bunch. Yet the model can be simplified and narrowed down tremendously, that helps for a better understanding of the dynamics and also for speeding up simulation and computation time.

The electric vector field spatial distribution is sketched in fig. 2.9 (a). The streaking field density is highly concentrated within the gap volume of the SRR, with a rapid decay in amplitudes outside the gap. Therefore it is sufficient to evaluate this model in a small volume around the SRR gap of $(60 \times 60 \times 160)\,\mu m^3$ where the physical gap dimensions are $(20 \times 20 \times 80)\,\mu m^3$ with a spatial resolution of $1\,\mu m$.

In fig. 2.9 (b) the two planes A, B are introduced.
Plane A spans a cross section in the vertical (y) versus the longitudinal (z) plane, the shown example plane is horizontally centered in the gap: $x = 0\,\mu m$.
Plane B spans a cross section in the vertical (y) versus the horizontal (x) plane and sits in

Table 2.2.: Figure labels of field cross sections in the appendix for different fields and cross section planes.

	cB_x	cB_y	cB_z	E_x	E_y	E_z
Plane A	A.3	A.5	A.7	A.9	A.11	A.13
Plane B	A.4	A.6	A.8	A.10	A.12	A.14

the longitudinal center of the gap: $z = 0\,\mu m$.

Multiple cross sections in plane A at several x-positions and in plane B at several z-positions are shown in the appendix for each real field component, the figures are referenced in tab. 2.2. In order to compare the influence of the E- and B-field, the B-field fields are multiplied by the speed of light c, the underlaying thoughts for this representation are discussed in section 2.1.2.2. Luckily this bulk of plots and information serves as argument to reduce the complexity of the streaking field.

Upon analysis, it becomes evident that the streaking field model can be significantly simplified. Especially, it is feasible to condense the entire imaginary fields into the field behavior in the time domain. It is not even necessary to distinct the six field components in the time domain since all components oscillate synchronously. This reduction is elaborated upon in section 2.1.2.1. Additionally, the magnetic components are much weaker than the electric ones and can be neglected entirely, as discussed in section 2.1.2.2. Consequently, the focus narrows down to the spacial distribution of the three electric field components, these are described in section 2.1.2.3.

2.1.2.1. Imaginary fields and time domain

To begin with, the imaginary parts determine the temporal evolution of all field components. As the amplitude of the electric field changes over time, the magnetic field is invoked, according to the Maxwell-Ampère law:

$$\nabla \times \vec{B} = \mu_0 \vec{J} + \mu_0 \epsilon_0 \frac{\partial \vec{E}}{\partial t} \tag{2.24}$$

All three components of the electric field change synchronously with each other over the entire simulated volume. Similarly, all components of the magnetic field are synchronized with each other too, but with a phase shift of 90° compared to the phase of the electric field. With this understanding, we can simplify the comprehensive imaginary information by formulating the evolution of all fields in the time domain, rather than formulating the explicit information for each field in every grid point of the simulation volume.

The streaking field in time domain is shown in fig. 2.10 (a). As all field components oscillate synchronously, it does not matter which field was probed for the time domain, nor where the probe is located exactly. However the field was examined for the vertical electric field component and probed in the SRR gap center. The plot reveals an overdamped oscillation pattern. The amplitude builds up over a few cycles and then decays over the next 3-4 cycles.
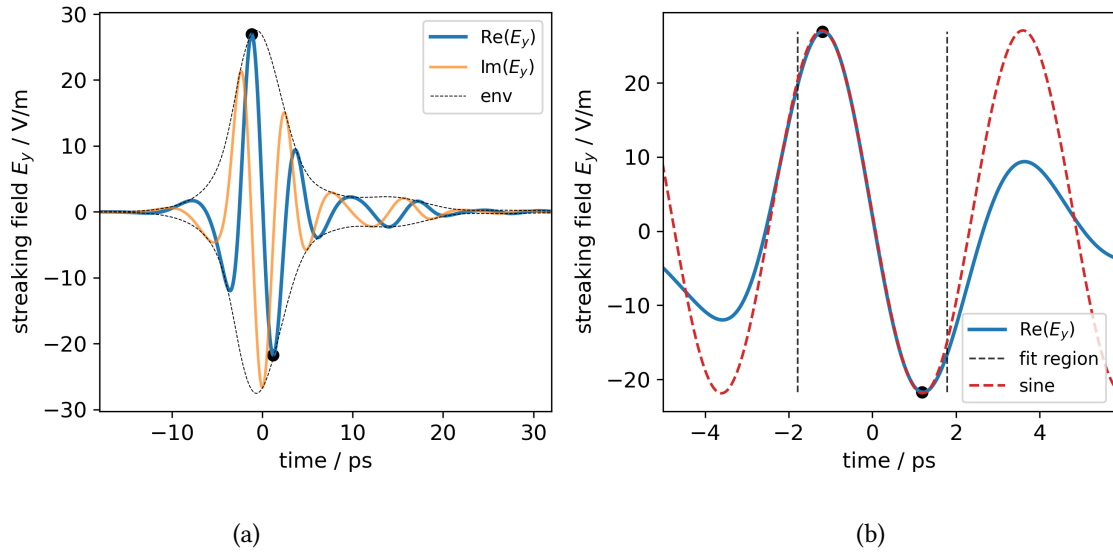
Figure 2.10.: The streaking field time domain (a) and zoomed into the region around the main zero crossing (b). The real and imaginary parts are shown together (colored) with the field envelope (dotted). The real part extreme values are marked by black dots. In (b) the signal approximation with a sine curve is added to the graph. The dashed lines visualize the data cut used for the sine fitting routine. All signal were probed in the SRR gap center. The signals amplitudes originate from a simulation with an incident THz pulse with $\hat{E}_{THz} = 1\,V/m$.

Damping time: Over the time domain, the signal time envelope can be calculated by the absolute value of the complex solution, this was shown already in equ. 2.11. The envelope fit is shown in fig. 2.10 (a) (black, dotted). From the envelope, the damping time can be calculated numerically as the time during which the signal exceeds $1/e$ of its maximum value. With this definition the damping time is found to be $\tau = 4.3\,ps$.

Streaking window: The streaking effect is directly related to the rate of change of the electric field over time and to the field amplitude. For ideal streaking conditions, the bunch must pass the streaking field within the main cycle between its highest maximum and lowest minimum values. This time window from peak to minimum spans $T_{strk} = 2.38\,ps$ and will be called the streaking window from now on.

Sine approximation: To discuss these ideal synchronizations, the time domain of the streaking field can be simplified within the main cycle to a sine curve. The time domain zoomed into the streaking window (blue, solid) and the sinusoidal approximation (orange, dashed) are shown in fig. 2.10 (b). For the sine fitting routine, a data subset with a length of 4/3 the streaking window was used, the subset is visualized by the plotted markers (black, dashed). Considering the subsequent discussion of simulation scenarios, computational speed is of importance. The sinusoidal approximation offers the advantage of performing quick computations while serving as a reasonably accurate representation of the field dynamics. However, for bunches longer than the streaking window or those that are not

synchronized correctly and arrive partially outside the streaking window, it is necessary to consider the actual time domain instead of the sine approximation.

The sine model is parameterized as follows:

$$E_{\text{strk}}(t) = -\hat{E}_{\text{strk}} \sin(2\pi f_{\text{strk}} t) + C \tag{2.25}$$

The found parameters are

1. $f_{\text{strk}} = 208.3\,\text{GHz}$, the frequency in the main cycle is higher than the peak frequency of the entire spectrum,

2. $-\hat{E}_{\text{strk}} = 24.47\,\text{V/m}$, the amplitude of the oscillation. With the negative sign and $t = 0$ is set to the center of the streaking window the sine function does not need an additional phase offset.

3. $C = 2.60\,\text{V/m}$, since the oscillation is damped, the maximum and minimum values are not symmetric around $E_y = 0$. The fitting algorithm optimized for an undamped sine oscillation and found therefore the offset $C \neq 0$ for the best representation within the given window. This small offset would not change the dynamics other than deflecting the entire, streaked bunch upwards by an insignificant amplitude. Therefore this offset will be ignored.

The time axis is defined with $t = 0$ at the time of the main zero crossing.

Frequency domain: In fig. 2.11 the fields frequency domain corresponding to the discussed time domain is illustrated in both, logarithmic (a) and linear scale (b). The frequency distribution exhibits some broadness and is not sharply defined, but it does show a clear peak at 166.6 GHz. On the other hand, the sine approximation reveals the streaking frequency of 213.7 GHz. The discrepancy can be explained with the circumstance, that the time domain is a result of all contributing frequencies. The resulting oscillation in the streaking window, between the extreme peak values is not oscillating solely in the resonance frequency but on the center of gravity in the frequency realm. Therefore one has to distinguish between two frequencies:

1. $f_{\text{res}} = 167.2\,\text{GHz}$: The extreme value of the streaking field frequency domain.

2. $f_{\text{strk}} = 208.3\,\text{GHz}$: The streaking frequency as the fitting result of the streaking field within in the streaking window.

The frequency center of gravity can also be calculated numerically as discussed in [37] as

$$f_{CG} = \frac{\sum_i^n |f_i E_{\text{strk}}(f_i)\Delta f|}{\sum_i^n |E_{\text{strk}}(f_i)\Delta f|} . \tag{2.26}$$

This calculation leads to the found streaking frequency, yielding a discrepancy of just 3 GHz.
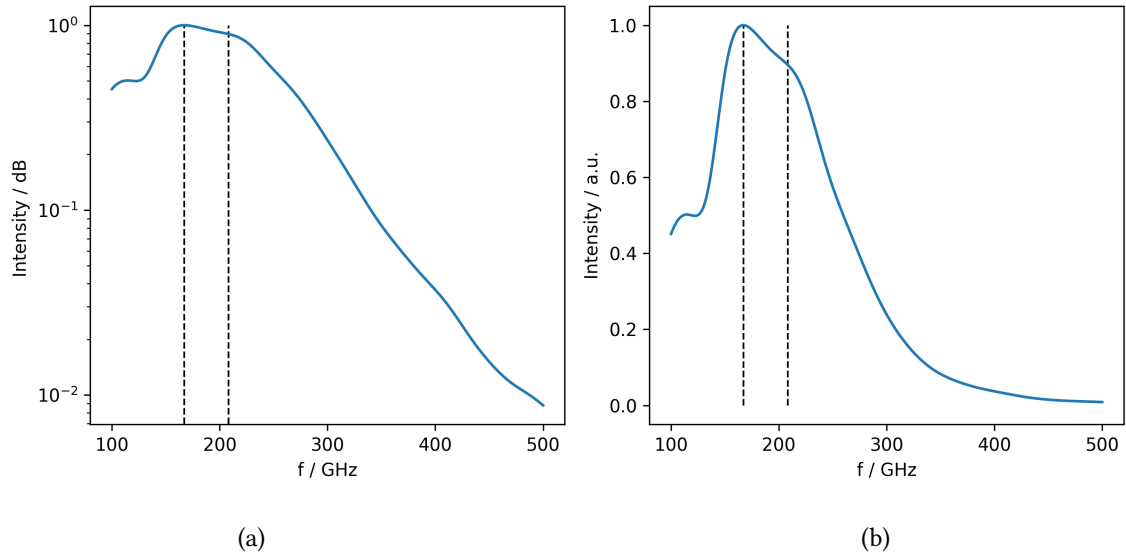
Figure 2.11.: Streaking field frequency domain, plotted in logarithmic (a) and in linear scale (b). The dashed lines mark the resonance frequency $f_{\text{res}} = 167.2\,\text{GHz}$ and the streaking frequency $f_{\text{strk}} = 208.3\,\text{GHz}$.

Table 2.3.: extreme values of E and cB for each direction. Values for an incident pulse E-field of $1\,\text{V/m}$, for correct scaling the table values need to be multiplied by the incident pulse E-field calculated in equ. 2.23.

Field	dimension	range	Unit
$\vec{E}$	x	[-73;+73]	V/m
	y	[0;+82]	V/m
	z	[-68;+68]	V/m
$\vec{B}$	x	[-25;+25]	nT
	y	[-11;+11]	nT
	z	[-5;+38]	nT
$\vec{v} \times \vec{B}$	x	[-3.2;+3.4]	V/m
	y	[-7.5;+7.3]	V/m
	z	[-0.1;+0.1]	V/m

2.1.2.2. Magnetic field component

In the streaking field, the magnetic components are weak in comparison with the electric ones and can be disregarded. The force acting on an electron by both the electric and the magnetic field can be described by the Lorentz force:

$$\vec{F_L} = e(\vec{v} \times \vec{B} + \vec{E}) \tag{2.27}$$

The extreme values of the field components for each dimension are collected in tab. 2.3 for the electric field followed by the values for the plain magnetic field. In order to estimate the magnetic force, the cross product with the electron velocity needs to be calculated. The forward velocity (v_z) can be approximated by the speed of light. The transverse velocity of

the electrons strongly depend on the machine settings, for an estimation one can assume a bunch divergence of 20 mrad, this value will be motivated in later chapters, for now it serves as a vague order of magnitude. Then the electron velocity can be expressed as

$$\vec{v} = \left(v_x, v_y, v_z\right) = c \left(0.02, 0.02, 1\right),$$ (2.28)

and the cross product in the Lorenz force follows:

$$\vec{v} \times \vec{B} = \begin{pmatrix} v_y B_z - v_z B_y \\ v_z B_x - v_x B_z \\ v_x B_y - v_y B_x \end{pmatrix}$$ (2.29)

The numeric results are added to above table and can be directly compared to the electric field components. It is directly obvious, that the $\vec{v} \times \vec{B}$-amplitudes are an entire order of magnitude below the E-amplitudes.

Yet the absolute influence on an electron is not directly the peak field amplitude but the force integrated along the electron path through the field. For this a quick glens on the B-field cross sections in the appendix is already sufficient (see tab. 2.2 for the discrete figure labels). The magnetic field distributions for the B_x and B_y component actually peak within the SRR geometry. The remaining (relative) high values are located sharply around the SRR corners, this distribution will not lead to a relevant integral over a straight electron path. The B_z component has a much larger distribution of (relative) high field amplitudes. Especially the circular SRR cutout houses a homogeneous B_z field. Only the B_z component would then lead to a relevant large path integral. However, the electron velocity mainly follows the z direction, making the cross-product of $(\vec{v} \times \vec{B})_z$ irrelevant.

In conclusion, all B-field components can entirely be neglected in their integrated influence on the electron bunch.

2.1.2.3. Electric field component

The remaining details to look into are the three E-field components. Analogue to the B-field, a detailed mapping of the E-field components are shown in the appendix. The figure labels are organized in the appendix using the structure shown in tab. 2.2. Apart from the detailed mapping, one can discuss the fields by only few cross sections.

In fig. 2.12 (a), the E_x component is shown in the vertical-horizontal plane. The field distribution is shown in the longitudinal position of $z = 0\,\mu m$, but the pattern remains consistent along the entire z-range. The field exhibits moderate amplitudes that are concentrated closely around the edges and corners of the resonator gap, while the gap center remains almost field free. Although the electric field pattern reminds of that of a magnetic skew quadrupole, the effects are different. As the magnetic field applies a Lorentz force perpendicular to the field lines, the force from the E-field follows its field lines. Consequently, the E_x component causes defocusing of the upper half of the electron bunch and focusing of the lower part. As the bunch travels through the SRR, the EM fields
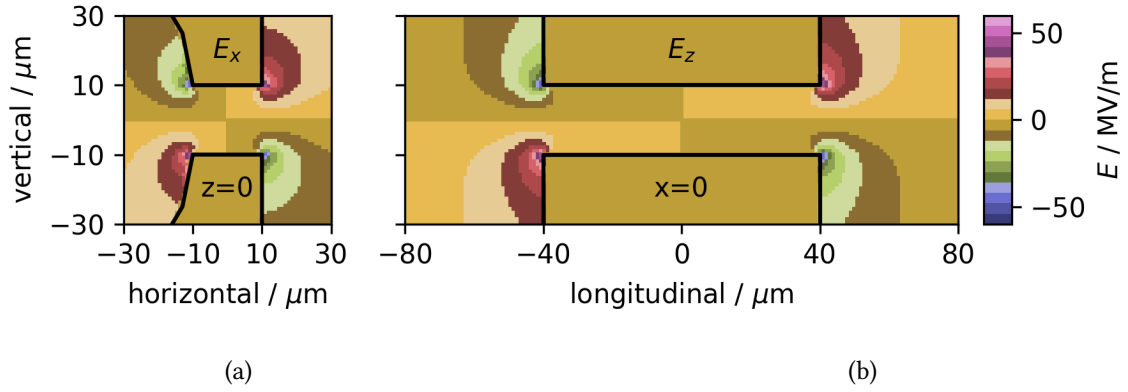
Figure 2.12.: Distribution of the E-field in the streaking field model. (a) shows the E_x component in a vertical-horizontal cross section at $z = 0\,\mu$m. (b) shows the E_z component in a vertical-longitudinal cross section at $x = 0\,\mu$m. The black lines show represent the SRR edges.
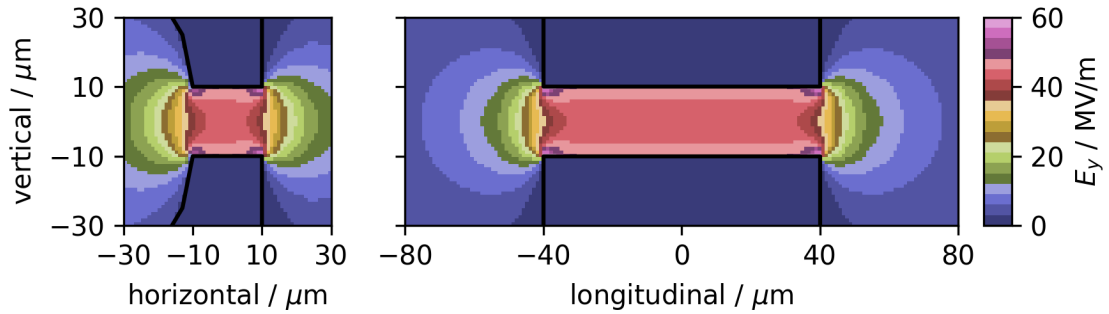
Figure 2.13.: Distribution of the vertical E-field component E_y in the streaking field model. Two cross sections are shown: the vertical-horizontal (left) at $z = 0\,\mu$m and the vertical-longitudinal (right) at $x = 0\,\mu$m. The black lines show represent the SRR edges.

oscillate, the phase advance causes the E_x field to flip sign. Therefore in the upper half, the at first focusing E_x component when entering becomes defocusing when leaving the SRR gap (and analogue for the lower half). This further reduces the influence of the E_x component.

The E_z component appears very similar to the E_x component but in the vertical-longitudinal instead of the vertical-horizontal plane. The field is shown in fig. 2.12 (b) at $x = 0\,\mu$m but remains consistent along the entire x-range. This field reaches also moderate field amplitudes closely bound to the structure edges and corners while the gap center remains almost field free. The Lorentz force applied from this field modulate the longitudinal bunch momentum, that of course is orders of magnitudes larger than transverse electron momenta. Therefore the influence of the E_z field is negligible. Note, that both, the E_x and the E_z fields barely penetrate the gap center where the dynamics are dominated by the remaining E_y component.

43

The final and most relevant component of the streaking field is the vertical electric field component E_y. It is shown in two cross sections, vertical versus horizontal, respectively versus longitudinal in fig. 2.13. Also this field is plotted in the gap center, with $x = 0\,\mu m$ and $z = 0\,\mu m$. It keeps its shape over the x-range and also over the z-range. The field has fringe fields outside the gap and high amplitude spikes on the corners, apart from that the field is distributed very homogeneously inside the gap. The plot reveals the dipole-like field distribution, yet it is important to remember the temporal oscillation that flips the all positive E_y component into all negative.

The E_y field component is the dominant field in the complex 3D EM streaking field model in the SRR gap. The simulated model shows, that the SRR geometry effectively creates the desired oscillating, vertical streaking field. Henceforth, the E_y component is ment when referring to the streaking field.

2.1.2.4. Streaking field amplitude

The streaking field amplitude refers to the maximum value of the vertical electric field component during its temporal evolution. In the conducted CST simulation, a $\hat{E}_{THz} = 1\,V/m$ incident THz pulse was used. The simulation result revealed a greater amplitude in the streaking field, it was analyzed by the sine approximation given in equ. 2.25, the amplitude of the streaking field is $\hat{E}_{strk} = 24.47\,V/m$. The ratio between the incident THz pulse and the streaking field peak value is termed the enhancement factor:

$$X = 24.47 \tag{2.30}$$

One notable outcome of the CST simulation is the observed linear relationship between the incident THz pulse and the streaking field amplitude. Based on the calculation in section 2.1.1.5, the actual THz amplitude is determined to be $E_{THz} = 0.552\,MV/m$. Consequently, the anticipated streaking field is

$$\hat{E}_{strk} = \hat{E}_{THz} \cdot X = 13.5 \pm 0.9\,MV/m. \tag{2.31}$$

2.1.3. Resonator geometry effects on the streaking field

The geometry of the resonator body affects the streaking field. The streaking field discussed so far is an outcome of the discrete geometry that was tested and examined in the experiments. Yet for future optimizations the geometry can be changed to alter deliberately some field parameters. For this purpose, S. Glukhov conducted a CST simulation based study on the influence of several geometric parameters [36]. A few of which show great potential for designing a resonator geometry with optimized field properties and are discussed in the following.
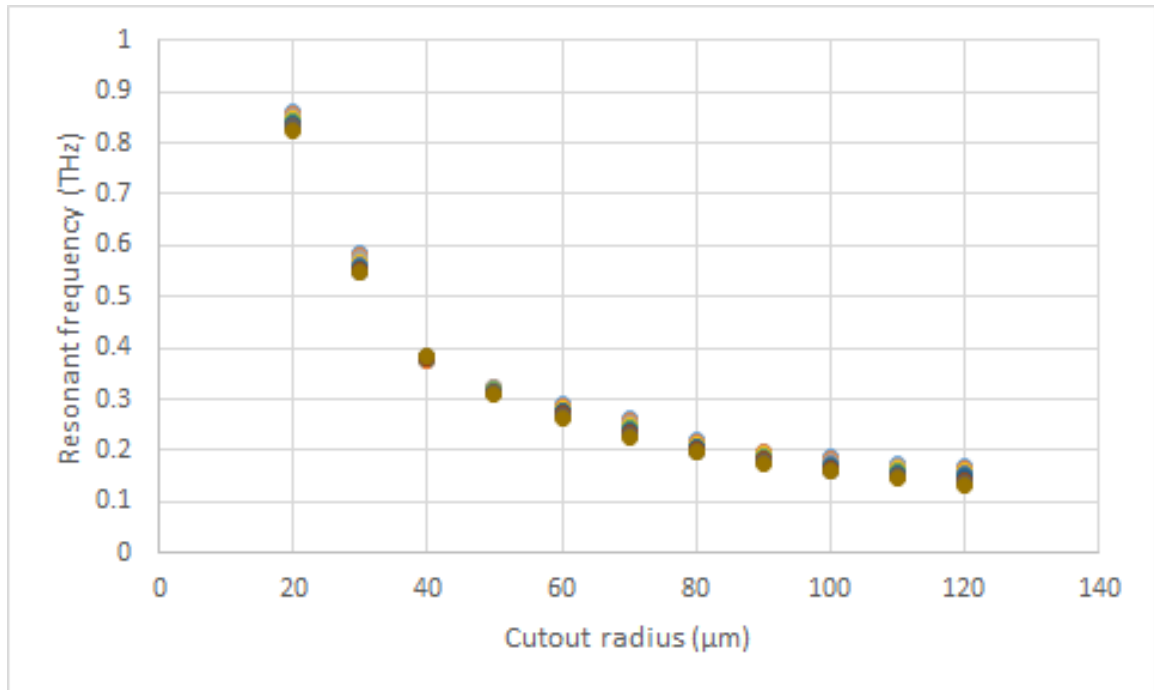
Figure 2.14.: SRR cutout diameter effect on the streaking field resonance frequency. The different colors represent different resonator thicknesses between 80 and 400 μm. This figure was kindly provided by S. Glukhov.
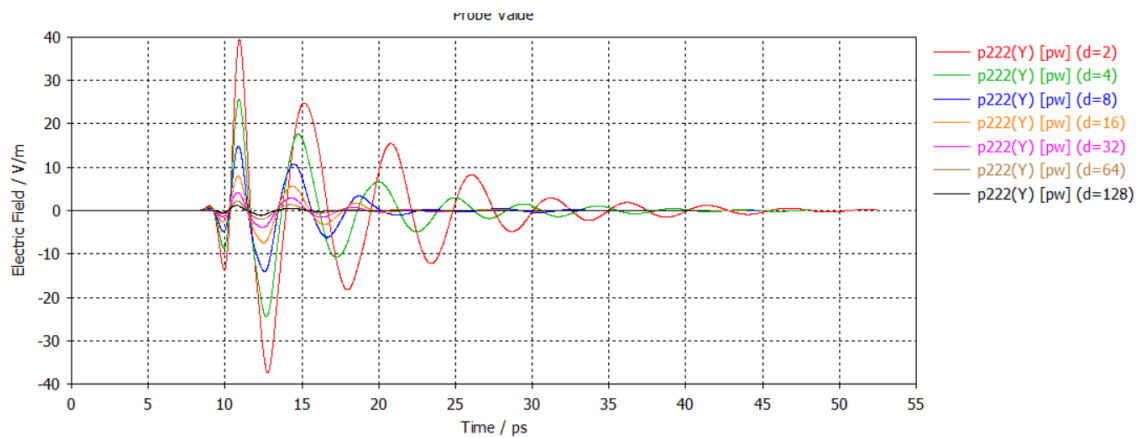
Figure 2.15.: SRR gap size effect on the streaking field E_y amplitude. The different colors represent different square gap sizes. This figure was kindly provided by Sergei Glukhov.

Resonance frequency: Increasing the circular cutout diameter leads to a reduction in resonance frequency, as depicted in fig. 2.14.

With the cutout diameter one can therefore improve the temporal resolution of the diagnostic tool. A higher resolution on the other hand implies a reduced bunch length acceptance.

Enhancement factor: Decreasing the square gap size increases the enhancement factor and thus the streaking field amplitude, as shown in fig. 2.15. The larger enhancement factor increases the streaking kick and therefore the measurement signal. Yet a smaller gap size requires even stronger bunch focusing and a higher precision on aligning the bunch with the gap, making the whole experiment more challenging.

Integrated streaking kick: A thicker resonator generates the same streaking field for a larger gap volume, the thickness does not affect the field's amplitude. Consequently, there is an overall increase in the streaking effect since the electrons experience the streaking field for a longer duration. However, this augmentation is limited due to the phase shift advance from the electrons time of flight. It reaches a maximum when the phase advance equals 90°, which occurs when the thickness reaches

$$d = c/(4 f_{\text{strk}}) = 360\,\mu\text{m}\,. \tag{2.32}$$

Accounting for the bunch length, the optimal resonator thickness is even thinner.

While the field's amplitude remains constant, a consequence of this is that the field contains more energy. This is possible due to the fact, that the thicker resonator absorbs more energy from the THz pulse.

A draw back is, that a thicker resonator means a "longer gap tunnel", this tightens the boundary conditions of divergence for the electron bunch.

2.2. Streaking field impact on the electron bunch

The impact of the streaking field on the electron bunch is discussed in this section. The streaking field properties have been discussed in detail in the last section, a summary of the findings are summarized in tab. 2.4. For an estimation, the effect is first calculated analytically. Therefore the effect of only the E_y component on a single electron is calculated in section 2.2.1. Then a numerical tracking simulation that considers all six field components acting on an entire electron bunch is discussed in section 2.2.2. Both approaches address the vertical momentum gained from the field and the thereafter developed vertical offset by reaching the beam monitor. In the last subsection 2.2.3 the results are compared and discussed.

Both approaches discuss the same scenarios. The simulated bunch properties are as follows:

- The distribution follows a Gaussian shape in every axis with $\sigma_x = \sigma_y = 5\,\mu m$ and $\sigma_z = 200\,\mu m$ with a cutoff at $4\,\sigma$.

- The bunch forward momentum is $p_z = 5\,MeV/c$, the bunch has no transverse momenta and zero momentum spread in every axis.

- The drift length between the streaking field and the beam monitor is $d_{drift} = 1.126\,m$ like in the experiment.

- The bunch was simulated without intra-beam charge effects, $q = 0\,pC$.

- $N = 10.000$ macro particles were used.

For the analytical calculation only the on-axis reference particle is used. In order to understand the temporal dynamics different entrance times into the streaking field where assumed within $t_0 \in [-1.5; +1.5]$ ps. The bunch parameters and some calculation results from the following discussion are summarized in tab. 2.5.

The streaking field is modeled for a volume of $40 \times 40 \times 160\,\mu m$ with the sinusoidal approximation that is again shown in fig. 2.16. The colored marker represent different electron entry times t_0 considered in the analytical calculation. The simulated bunch

Table 2.4.: Streaking field parameter

Parameter		value	unit
THz pulse amplitude	$\hat{E}_{y,THz}$	0.552±0.036	MV/m
Streaking field amplitude	$\hat{E}_{y,strk}$	13.5 ±0.9	MV/m
Enhancement factor	X	24.47	-
Streaking frequency	f_{strk}	208.3	GHz
Streaking window	T_{strk}	2.38	ps
Life time (1/e)	τ	4.3	ps

Table 2.5.: Electron bunch parameters for the simulation of the streaking effect.

Parameter		value	unit
momenta	p_x, p_y, p_z	0,0,5	MeV/c
momenta spread	$\Delta p_x, \Delta p_y, \Delta p_z$	0,0,0	MeV/c
bunch length	$\sigma_y, \sigma_y, \sigma_z$	5,5,200	μm
charge	q	0	pC
lorentz factor	γ	0.995	
time of flight	t_{ToF}	0.534	ps
phase advance	θ	40	degree
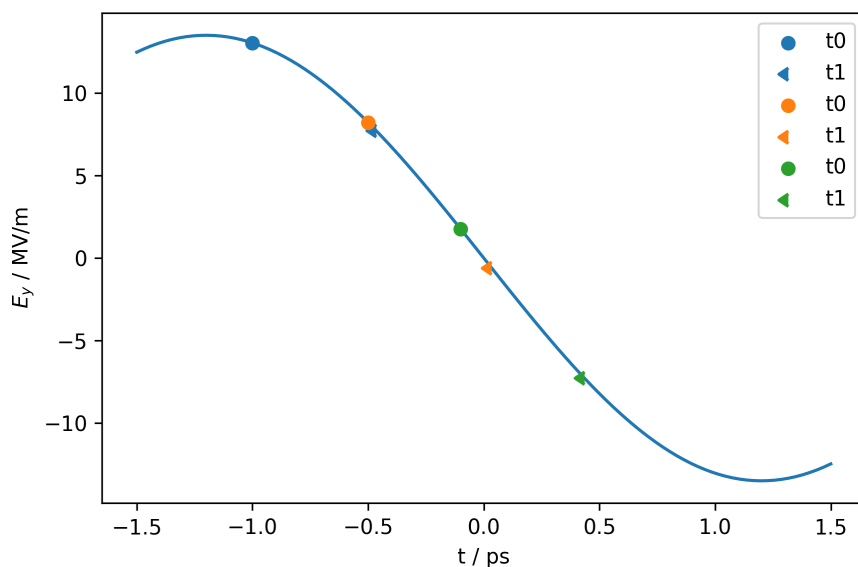
Figure 2.16.: Streaking field in sinus approximation represented in time domain. The marker represent different electron entry times t_0 and after the time of flight the exit time t_1 when the electron is leaving the streaking field.

on the other hand is modeled with a bunch length of $\sigma_z = 200\,\mu$m and a 4 sigma cutoff, effectively spanning 115% of the streaking window.

2.2.1. Analytical estimation

This subsection explains the calculation of the vertical momentum for a single electron after passing the streaking field. As the electron travels, the streaking field proceeds in phase.

Phase advance: With the momentum of 5 MeV/c, the electron's relativistic gamma is

$$\gamma = \sqrt{1 + \left(\frac{p_z}{m_e c}\right)^2} = 0.995\,,$$ (2.33)
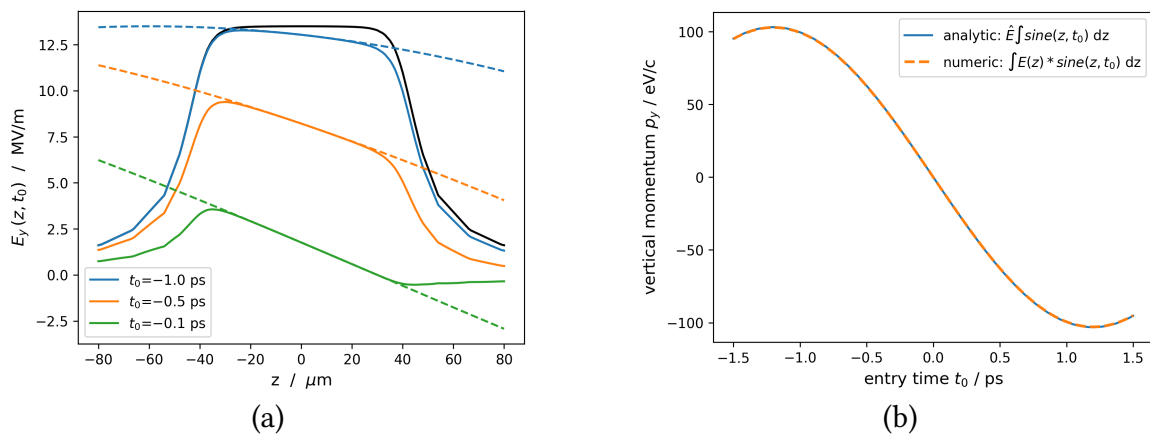
Figure 2.17.: A) Illustration of the vertical electric field along the z-axis. The streaking field (black) and the experienced field, modulated by the temporal phase progress during the time of flight (colored, solid) are shown. The experienced field is the product of the streaking field (black) with the segment of the sinusoidal temporal aspect (colored, dashed). The colors represent different entrance times. B) Illustration of the final vertical momentum as function of the electron entrance time. The analytical approach is represented as the solid, blue line while the more precise, numerical result is shown by the orange, dashed line.

therefore the approximation of $v \approx c$ can be made. The electron passes the $d = 160\,\mu m$ deep streaking field model within the time of flight:

$$t_{\mathrm{tof}} = d/c = 0.534\,\mathrm{ps} \tag{2.34}$$

By this time, the streaking field proceeds by the phase advance

$$\theta = 360° \, t_{\mathrm{tof}} \, f_{\mathrm{strk}} = 40° \, . \tag{2.35}$$

Streaking field witnessed by the electron: Because of the streaking field phase advances during the time of flight, each electron experiences the discussed streaking field modulated by its temporal oscillation. As the electron travels along the beam axis $\vec{z}$, the experienced field is given by:

$$\tilde{E}_y(z, t_0) = E_y(z) \, \sin((z/v - t_0) \, 2\pi f_{\mathrm{strk}}) \tag{2.36}$$

as a function of the entrance time t_0. The experienced field $\tilde{E}_y(z, t_0)$ will be discussed as a function dependent on the position z rather than in the elapsed time. This makes it easier to differentiate the dependent parameters from different starting times t_0.

The streaking field $E_y(z)$ without any time dependencies is shown in fig. 2.17 (a) as profile along the z-axis by the solid black line. Also added in the graphic are the experienced streaking fields $\tilde{E}_y(z, t_0)$ for a single electron with three different discrete entry times as solid, colored lines. The according underlying sinusoidal phases that modulate the streaking field are represented by the dashed lines.

49

Integrated vertical kick: The vertical momentum collected by the electron from the electric field is given by the integrated force over time

$$\Delta p_y = \int F(t) \mathrm{d}t, \tag{2.37}$$

with $F_y = qE_y$ being the Lorentz force invoked by the streaking field, neglecting the magnetic contribution. Here the momentum was calculated from the integral over travel distance instead time of flight as a function of the entrance time t_0

$$\Delta p_y(t_0) = q/c \int \tilde{E}_y(z, t_0) \mathrm{d}z. \tag{2.38}$$

This equation was easily solved by a numerical integration for different entry times, the result is shown in fig. 2.17 (b) as dashed line.

However an analytical expression is desired. For solving the integral, the unmodulated streaking field $E_y(z)$ can be approximated as a rectangular step function rect(z) that yields 1 between the steps located at $-\zeta$ and $+\zeta$ and 0 outside, multiplied by the streaking field amplitude $\hat{E}_{y,\mathrm{strk}} = 13.5\,\mathrm{MV/m}$:

$$E_y(z) \approx \hat{E}_{y,\mathrm{strk}} \, \mathrm{rect}(z, \zeta) = \hat{E}_{y,\mathrm{strk}} \, \Theta(z - \zeta) \, \Theta(z + \zeta) \tag{2.39}$$

The step position ζ was chosen such, that the integral beneath the step function matches the numerical integral beneath the unmodulated streaking field $E_y(z)$:

$$\int E_y(z) \mathrm{d}z = 104\,\mu\mathrm{m}\,\hat{E}_{y,\mathrm{strk}} \tag{2.40}$$

$$\int \hat{E}_{y,\mathrm{strk}} \, \mathrm{rect}(z, \zeta) \mathrm{d}z = 2\zeta \, \hat{E}_{y,\mathrm{strk}} \tag{2.41}$$

$$\zeta = 52\,\mu\mathrm{m} \tag{2.42}$$

With this simplification, the integral of equ. 2.38 becomes solvable:

$$\Delta p_y(t_0) \approx q/c\,\hat{E}_y \int \mathrm{rect}(z, \zeta) \, \sin\left((z/c - t_0)\, 2\pi f_{\mathrm{strk}}\right) \mathrm{d}z \tag{2.43}$$

$$= q/c\,\hat{E}_y \int_{-\zeta}^{+\zeta} \sin\left((z/c - t_0)\, 2\pi f_{\mathrm{strk}}\right) \mathrm{d}z \tag{2.44}$$

$$= \frac{q/c\hat{E}_y}{2\pi f_{\mathrm{strk}}/c} \left[\cos((z/c - t_0)\, 2\pi f_{\mathrm{strk}}) \right]_{-\zeta}^{+\zeta} \tag{2.45}$$

The identity

$$\cos(x) - \cos(y) = -2\,\sin\left(\frac{x - y}{2}\right) \sin\left(\frac{x + y}{2}\right) \tag{2.46}$$

can be reformulated for our case as

$$\cos(At + B) - \cos(At - B) = -2\,\sin\left(\frac{B - (-B)}{2}\right) \sin\left(\frac{At + At}{2}\right) \tag{2.47}$$

with $A = -2\pi f_{\text{strk}}$ and $B = 2\pi f_{\text{strk}} \zeta / c$. After reordering, the integral becomes:

$$\Delta p_y(t_0) = \frac{-2c}{2\pi f_{\text{strk}}} \sin(\zeta / c \cdot 2\pi f_{\text{strk}}) \sin(t_0 \cdot 2\pi f_{\text{strk}}) \cdot \hat{E}_y \frac{q}{c} \tag{2.48}$$

$$= 103.1 \times 10^{-6} \sin(t_0 \cdot 2\pi f_{\text{strk}}) \cdot \hat{E}_y \quad \text{in} \quad \text{eV/c (analytical)} \tag{2.49}$$

The factor q/c is shifted into the unit notation of eV/c. For every $1\,\text{MV/m}$ in peak field strength, the maximum vertical momentum is approximately $103\,\text{eV/c}$.

This analytical result is also shown in fig. 2.17(b), the result is very close to the numerical calculation. They share the same sinusoidal shape but differ in amplitude by a negligible $0.2\,\%$.

Note, that this calculation was conducted under the assumption of $v_z = c$. A calculation that considers a finite forward velocity yields a different result already in equ. 2.37. The time spent in the streaking field for bunches with $v_z < c$ increases. Consequently, p_y approximates the result calculated here in the ultra-relativistic limes with $1/p_z$. The deviation of p_y between the relativistic correct calculation and the simplification made here is already below $1\,\%$ for a bunch forward momentum of $5\,\text{MeV/c}$, this deviation may be an explanation of the differences between the above calculation and the simulation result. Another TDS chamber is planned to be installed after the FLUTE linac, which will increase the bunch momentum up to $50\,\text{MeV/c}$. Even for this case, the difference in Δo_y calculated for these two momenta is below $1\,\%$ too. With these results, it can be confidently asserted that the relativistic perspective can be disregarded, and the simplification of using $v = c$ can be used for bunch momenta of $5\,\text{MeV/c}$ or more.

Slope and vertical offset: With the vertical momentum p_y and the unaffected longitudinal momentum p_z the electron travels on an angled trajectory after it passed the SRR. The slope of this trajectory is given by the momenta ratio $m = p_y/p_z$. The used small angle approximation is justified, because p_y is three orders of magnitude below the forward momentum p_z.

The vertical offset on the beam monitor is determined by the product of the drift length d_{drift} and the trajectory slope, using the small angle approximation:

$$\Delta y = d_{\text{drift}}\, p_y / p_z \tag{2.50}$$

Inserting the expression of the vertical momentum 2.48 into the above relation gives:

$$\Delta y(\hat{E}_y) = 103.1 \times 10^{-6} \sin(t_0 \cdot 2\pi f_{\text{strk}}) \cdot \frac{d_{\text{drift}} \hat{E}_y}{p_z} \quad \text{in} \quad \text{m} \tag{2.51}$$

The distance between the YAG screen and the SRR is $d_{\text{drift}} = 1126\,\text{mm}$ and the forward momentum is assumed to be $p_z = 5\,\text{MeV/c}$. The vertical offset is calculated for both, a streaking field amplitude of $\hat{E}_y = 1\,\text{MV/m}$ and the expected amplitude $\hat{E}_{y,\text{strk}} = (13.5 \pm 0.9)\,\text{MV/m}$ that has been calculated in equ. 2.31.

The vertical offset is:

$$\Delta y(1\,\text{MV/m}) = \sin(t_0 \cdot 2\pi f_{\text{strk}}) \cdot 0.023\,\text{mm} \tag{2.52}$$

$$\Delta y(13.5\,\text{MV/m}) = \sin(t_0 \cdot 2\pi f_{\text{strk}}) \cdot (0.311 \pm 0.021)\,\text{mm} \tag{2.53}$$

This result indicates that individual electrons can arrive at the beam screen, either higher or lower, by up to 0.311 mm depending on the entrance time t_0. If the bunch has a minimum length equal to the streaking window of 2.4 ps, the head is maximally down, and the tail is maximally up-streaked. Consequently, its vertical beam size increases by up to 0.622 mm. However, it must be noted that the beam shape will no longer be Gaussian, and the beam size should no longer be specified in terms of sigma. This size difference compared to an unstreaked bunch is certainly measurable, and a detailed examination of the limitations of this measurement method is presented in Chapter 2.3.

2.2.2. Tracking simulation

Simulation software: The SRR is an active component that cannot be directly incorporated into any tracking code. To accurately simulate the dynamics, the software needs to be slightly modified from its default parameters. The preceding discussion of the analytical calculation serves as a benchmark to verify the correct initialization of the simulation software.

The tracking code ASTRA [38] was choosen as tool for all beam dynamic related simulations within this thesis. This software is known for precise space charge calculation especially in the low energy regime. As the bunch is focused on the tiny SRR gap, a high charge density can be expected where the space charge forces will become relevant. As a first step however, the simulation is carried out without the repelling space charge effect in order to consider solely the streaking field influence.

Simulations covering the intra-beam charge effects are discussed in the upcoming following chapter.

Tracking scenario: The bunch parameters for the tracking scenario have been already discussed in the beginning of this chapter and are summarized in tab. 2.5. The simulation was carried out in two steps. The first simulation focused on precise tracking of the bunch over a distance of 1.4 mm [4] , wherein the streaking field is centered. In this simulation, the full 6D field map was taken into account, utilizing the sinusoidal approximation to approximate the field temporal behavior.

For a precise simulation, the Maxwell equations should be reevaluated and applied on the bunch several times while the bunch travels through the streaking field. Yet the SRR is

---

[4] The simulated distance of 1.4 mm covers the position for the full streaking field 0.16 mm and a 4 ps bunch length (5σ) before and after the streaking field.
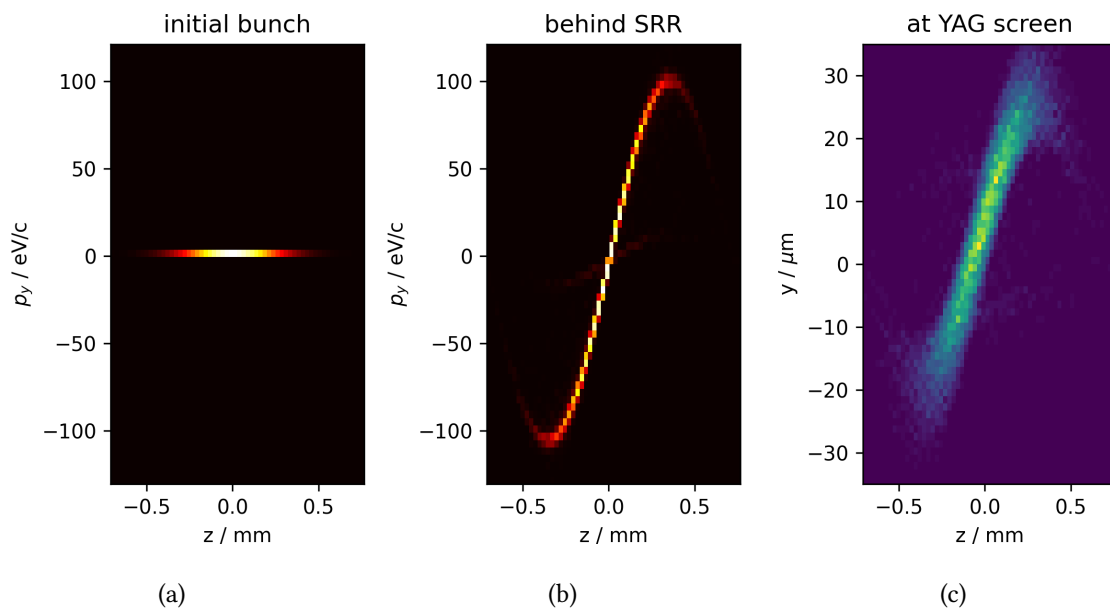
Figure 2.18.: Tracking simulation results. (A) and (b) show the bunch vertical momentum distribution versus the longitudinal position for (a) the initial bunch and (b) the bunch streaked right after the SRR. (C) shows the distribution of macro particles in the y-z plane. Note the different color schemes for momentum and position displays.

much smaller than regular accelerator components and the default simulation step size is too large. ASTRA allows setting the temporal step size of the simulation by the so called Runge-Kutta [39] parameter Hmax. The streaking field is modeled with a precision of 1 μm. Hmax was set to 1.1×10^{-6} fs, with the bunch velocity of $v = c$ which means, that the Maxwell equations are reevaluated every 0.3 μm.

A second simulation was conducted that simulates the bunch drifting to the beam screen station over $d_{\mathrm{drift}} = 1.126$ m. This simple scenario allows for larger step sizes of Hmax= 100 ps, corresponding to a step size of approximately 3 mm. This choice of step size allowed for more efficient computational performance while still maintaining an acceptable level of accuracy for the simulation.

2.2.3. Comparison and conclusion

The simulation results are presented by the three subplots of fig. 2.18. In subfigure (a), the bunch is depicted in the $p_y - z$ phase space before entering the streaking field, showcasing the initial distribution without any transverse momenta.

In subfigure (b), again bunch is again shown in the $p_y - z$ phase space, this time after the streaking process. The phase space carries the sinusoidal streaking imprint.

The third subplot (c) portrays the bunch in the $y - z$ plane, revealing the amplitude of the streaking effect versus time.

In order to compare the values of the y-offset and the vertical momentum to the analytical calculation one should take into account the diffuse spread of the simulated bunch. The initial transverse spread leads to some electrons picking up the spiking field values at the resonator gap edges and corners, leading to larger maximum values than expected. This can be clearly seen in fig. 2.18 as the distribution spread out around the highest and lowest p_y and y values. A fair comparison can be drawn as follows:

Both parameters, y and p_y peak at a relative z-position of 330 μm within the bunch. Considering only the share of macro particles within this z-position ±10 μm, one can find mean values of $\tilde{y}(sim) = 24.0$ μm and $\tilde{p}_y(sim) = 114.7$ eV/c.

These mean values are in a good agreement of the analytically calculated expectations for a streaking field amplitude of 1 MV/m: $\tilde{y}(ana) = 23$ μm and $\tilde{p}_y(ana) = 102.2$ eV/c.

Although the tracking simulation includes the entire 6D streaking field model, its outcome matches closely with the analytical expectations. Overall, the simulation check supports the initial assumption that the streaking field model can be simplified and reduced to the E_y component with the discussed linear relations between the streaking field amplitude, the resulting vertical momentum and finally the vertical offset. Also the streaking of bunches shorter than the streaking window of $T_{\text{strk}} = 2.38$ ps can be calculated and simulated with the sinusoidal approximation of the temporal development.

The measured and calculated THz pulse properties finally lead to an expected streaking offset of the electron bunch of ±345.6 μm. A streaking effect of this amplitude is clearly detectable with the FLUTE diagnostic system. The actual limitations for detecting streaking but also for using the streaking for a profile measurement are subject of the upcoming subsection.

2.3. Measurement limitations and resolution

2.3.1. Signal to noise

The detection of streaking relies on the additional vertical offset, that can be diagnosed by comparing the screen image of a streaked bunch to that of an unstreaked bunch. However, in the experiment both machine and bunch parameter instabilities exist to some extent. A "stable experiment" implies that the instabilities affecting the observable are below the detectable signal.

The stability of the electron beam size is a direct consequence of all instabilities of the active accelerator parts contributing to the experiment. These components include for example the clystron for the RF power or the UV pulse for electron generation. Yet these components also carry on imperfections from accessory equipment like for example the temperature stability of the water cooling for these devices or the electric net stability. Some of these sources are hardly avoidable.

Therefore the beam size changes from shot to shot, spreading around a mean value. The instability can therefore be quantified as the standard deviation of its spread. Despite the details strongly depend on the discrete experiment and machine settings, one can give a conservative estimation of $\sigma_{\mathrm{STD}} = 50\,\mu\mathrm{m}$.

The signal-to-noise ratio can be defined as the quotient of the observable signal and the according signal spread. If this S/N ratio is large enough, the signal can be detected clearly. The techniques developed in the scope of this thesis claim to differentiate streaking from non-streaking already at a $S/N = 2$. Therefore the streaking offset should be at least 2 times larger than the beam instability, this leads to a required streaking amplitude of $100\,\mu\mathrm{m}$. This limitation is much larger than the later discussed limitations coming from the beam screen resolution. Therefore controlling and improving the beam stability plays an important role in future upgrade planes for FLUTE.

2.3.2. Bunch length limitations

Longest measurable bunch length: The streaking method is only valid for bunches with a length below the streaking window, namely the time window between the streaking field maximum and minimum $T_{strk} = 2.38\,\text{ps}$. Otherwise the bunch will span more than half a period length in the streaking field, resulting in an overlap of multiple bunch parts beeing deflected to the same vertical offset. This could hardly be resolved in the data analysis and eventually would lead to wrong measurement interpretations.

In order to measure longer bunch lengths, the resonator geometry has to be altered to yield a lower streaking frequency. As discussed previously, this can be achieved by increasing the radius of the circular resonator cutout.

Shortest measurable bunch length: Much shorter bunches will experience only a small difference in the streaking field between the bunch head and tail. This of course negatively affects the streaking amplitude and therefore the possibility of its resolution. As discussed in the previous section in equation 2.52, the streaking offset is modulated by the electron arrival time by a sinusoidal function.

In order to maintain a resolvable S/N ratio, the above discussion demands a streaking offset of at least $100\,\mu\text{m}$. Assuming the discussed, expected streaking amplitude of $\hat{E}_{y,\text{strk}} = 13.5\,\text{MV/m}$, the bunch length is required to be at least $273\,\text{fs}$.

In order to measure shorter bunches, multiple approaches can be tackled:

- Increase of the streaking frequency by reducing the resonator cutout radius.

- Increase of the streaking field amplitude by e.g. more THz power or a smaller resonator gap dimension.

- Decrease of the noise level in the bunch size measurement.

2.3.3. Lower charge threshold for streaking detection

To detect a streaked bunch using a YAG screen image, it's essential to take into account the limits of charge density. Naturally, a bunch with lower charge is easier to focus, but there's still a threshold for it to be visible. The bunch is focused in the TDS chamber and diverges afterwards on its way to the forward YAG screen. Assuming again a streaking kick that results in a vertical streaking amplitude of $\Delta y = \pm 0.366$ mm, and further a natural bunch divergence that leads to an unstreaked bunch size at the forward screen of also 0.366 mm in x and y. This results in a final bunch size on the YAG screen of:

$$A = \pi \, \sigma_x \, (\sigma_y + 2\Delta y) = 1.263 \, \text{mm}^2 \tag{2.54}$$

Depending on the readout mode, the lower limit of charge density is either 0.26 pC/mm^2 or 1.89 pC/mm^2 respectively as discussed in section 1.2.2. By multiplying the charge density limit with the estimated bunch area, the lower limit of charge is calculated between 0.3 pC and 2.4 pC. At least, this amount of charge must undergo streaking to produce a detectable streaking image with the YAG screen setup.

Note, that the vertical, sinusoidal relocation of parts of the bunch by $\pm\Delta y$ would not directly increase the one sigma bunch size by $2\Delta y$. This quick estimation serves for a calculation of the expected order of magnitude.

2.3.4. Beam screen resolution

The beam monitor system, as discussed in section 1.1 has a resolution of 28 μm per pixel. This sets the technical lower limit for detecting a streaking offset. Obviously this limitation is much smaller than the limitations due to beam instabilities and therefore not a major concern for the time being. Yet this can be easily upgraded with an improved camera.

The resolution of the camera also determines the measurment resolution. Around the streaking field zero crossing, the streaking offset given in equ. 2.52 can be treated as linear:

$$\Delta y = \sin\left(t_0 \, 2\pi f_{\text{strk}}\right) \cdot 0.311 \, \text{mm} \approx t_0 \, 2\pi f_{\text{strk}} \cdot 0.311 \, \text{mm} \tag{2.55}$$

This equation can be reordered to find the temporal offset that yields a streaking amplitude equal to the screen resolution:

$$t_{\text{res}} = 28 \, \mu\text{m}/(2\pi f_{\text{strk}} \cdot 0.311 \, \text{mm}) \tag{2.56}$$

This equation yields a measurement resolution of $t_{\text{res}} = 69$ fs. This is a soft limitation, one can improve the resolution by an upgrade of the camera resolution, higher streaking frequency or a stronger streaking kick. For commissioning the SRR in the FLUTE low energy section, this resolution is already very good.

# 3. Influence of machine parameters

This chapter discusses the influence of several machine parameter on the streaking effect. Therefore different scenarios have been investigated by ASTRA tracking simulations, including space charge forces and the 3D streaking field model in the sinusoidal approximation. The results of an ideal scenario has been discussed in [40], its results are presented in fig. 3.1, it demonstrates the appearance of an obvious streaking signal. In this scenario, a 4.5 MeV/c bunch with a charge of 0.5 pC is created by a UV laser spot with a radius of 50 μm. The bunch is focused at the resonator where 87 % of electrons went through the SRR gap, afterwards the bunch drifts one additional meter towards the beam monitor. This scenario was carried out twice, without and with a THz pulse exciting the TDS resonator. The plotted screen images show the footprint for the unstreaked bunch (left) and the streaked bunch (right). Their difference image (right) is obtained by subtracting the pixel count of one image from the other for every pixel[1].

In this example, most of the bunch is affected by the streaking field. The tracking simulation lead to a slightly lower streaking amplitude than the expected $\Delta y = 346\,\mu$m, stated back in section 2.2.3 due to preliminary assumptions on streaking field properties. Still, the streaking offset surpasses the unstreaked bunch size, this signal would be clearly detectable in a real experiment, a similar outcome could be demonstrated by [9]. A second tracking

---

[1] The sign of difference pixel counts and thus, the order of the subtraction does not matter since later on the absolute value will be considered
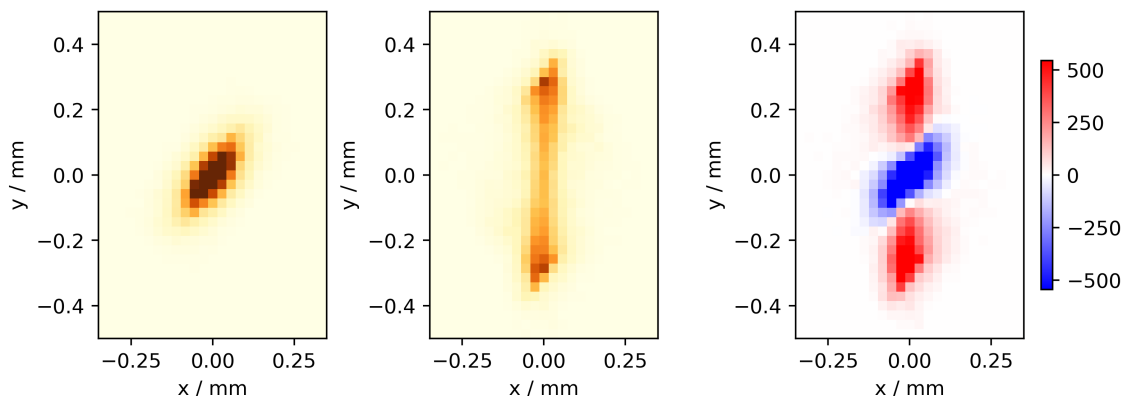
Figure 3.1.: Simulated forward screen image from ASTRA tracking simulation without (left) and with (center) an active streaking field in the TDS resonator. A difference image is calculated (right). In this simulation, 87 % of electrons went through the SRR gap. The image granularity resembles the actual screen resolution.
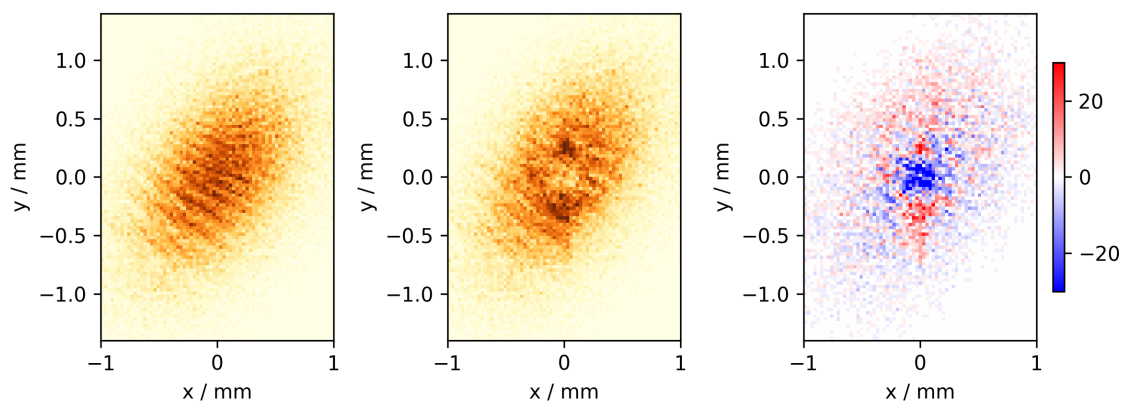
Figure 3.2.: Simulated forward screen image from ASTRA tracking simulation without (left) and with (center) an active streaking field in the TDS resonator. A difference image is calculated (right). In this simulation, 21 % of electrons went through the SRR gap. The image granularity resembles the actual screen resolution.

scenario was carried out with identical parameters except for a 10 times larger laser spot size, leading to a larger electron beam. The results are shown in fig. 3.2, this time only 21 % of charge could fit inside the gap. Also the unstreaked beam size on the forward screen is larger than the streaking offset. However, also in this outcome, the streaking signal can be detected by the charge relocation which is visible in the vertical structures in the difference image. The simulations shown in fig. 3.1 and fig. 3.2 were conducted with only 0.5 pC and are not representative for the beam dynamics engaged in the experiments later, yet demonstrate the detection principle.

As FLUTE operates with bunch charges above 5 pC, it is not possible to realize streaking images similar to the first shown example. Therefore this experiment relies on detecting the signal from difference images. Finding machine parameter to enhance their clarity is the goal of this chapter. The discussion is framed as an optimization problem. The following section address the degrees of freedom, boundary conditions, optimization objectives, and the optimization procedure.

3.1. Optimization strategy

The streaking field is spatially confined to the $20 \times 20\,\mu m$ gap. Even with ideal focusing conditions, it is inevitable that some electrons from the bunch will miss the gap, these are called q_{out}. Particles that hit the resonator body are highly scattered and can be disregarded for now. The remaining electrons that pass by the gap stay unstreaked and travel to the beam screen, forming the background. Electrons that are focused through the gap, denoted as q_{in}, build the streaking signal, which needs to be discovered within the background. This chapter discusses various machine parameters aimed at improving the signal-to-background ratio.
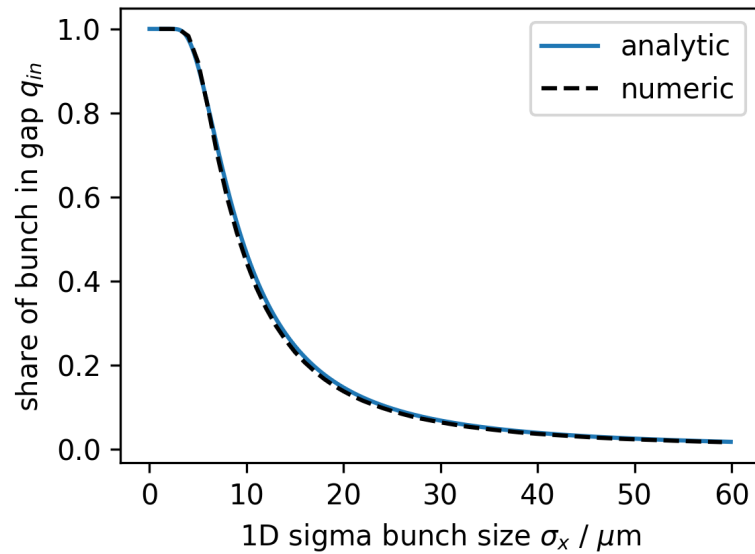
Figure 3.3.: Relation between the horizontal 1D bunch size and the charge within the 2D, 20 μm gap, called q_{in}.

3.1.1. Optimization goals

Two optimization strategies were specifically developed for different experiments: brightness-optimized and contrast-optimized.

Brightness optimized experiment: The first strategy is to simply maximize the signal. Since the streaking kick is independent of beam parameters, this means maximizing the absolute value of q_{in}.

Contrast optimized experiment: The second strategy involves optimizing the q_{in}/q_{out} ratio. This ratio will also be called relative q_{in}, it represents the charge within the gap relative to the charge outside the gap and thus the contrast of the streaking signal from the background.

As long as the bunch remains rotation symmetric and Gaussian, q_{in} exhibits a clear relationship with the bunch size. The bunch size σ_x refers to the standard deviation of the projection of the bunch's charge profile onto the horizontal axis. This projection typically forms a 1D Gaussian distribution. Meaning a bunch with a size of $\sigma_x = 10$ μm would fit 68 % of its particles inside a 20 μm wide slit.

A 2D aperture however further truncates this relation in the second plane. The charge inside a finite integral within $x \in [-X; X]$ and $y \in [-Y; Y]$ of a 2D Gaussian distribution follows:

$$q_{\text{in}} = \int_{-X}^{+X} \int_{-Y}^{+Y} \frac{1}{2\pi\sigma_x\sigma_y} \, e^{\frac{-x^2}{2\sigma_x^2} + \frac{-y^2}{2\sigma_y^2}} \, \mathrm{d}x \, \mathrm{d}y = erf\left(\frac{X}{\sqrt{2}\sigma_x}\right) erf\left(\frac{Y}{\sqrt{2}\sigma_y}\right) \qquad (3.1)$$

with the error function erf. Additionally, this analytical expression was cross-checked by a numerical calculation, based on a simulated 3D Gaussian bunch. Both approaches are evaluated using the dimensions of the SRR aperture, $X = Y = 10\,\mu\text{m}$ and assuming a rotation symmetric bunch with $\sigma_x = \sigma_y$. The results are plotted in fig. 3.3. This means that even with a bunch size of $\sigma_x = 10\,\mu\text{m}$ only 47 % of charge finds itself within the gap boundaries. The remaining charge partially gets scattered and eventually lost by the collision with the resonator body and partially reaches the screen unaffected from the entire TDS experiment and contributes as background.

As long as the bunch is rotation symmetric and Gaussian, the simulations can be evaluated by the (horizontal) bunch size which is easier accessible than the actual q_{in} and q_{out} parameters. Truncating the charge distribution with the aperture for example requires to examine the actual q_{in} value.

As a subordinate optimization goal, the unstreaked beam divergence should be minimized. A large divergence spreads the streaking signal over a larger screen area, which dilutes it, making the search more challenging.

3.1.2. Degrees of freedom

Machine parameters are directly and independently controllable during the experiment and serve as the degrees of freedom for this discussion, they are listed in tab. 3.1. A distinction should be made between machine parameters and the resulting beam parameters. Typically, a machine parameter primarily affects one specific beam parameter, as summarized in tab. 3.1, e.g. the laser power affects the bunch charge. Yet beam parameters are intertwined with each other via the repelling space charge forces, therefore a machine parameter also inflicts indirect changes on several other beam parameters too. A higher bunch charge for example leads to a higher bunch divergence and with the changed trajectory leads to different pick-ups in all EM-fields.

Table 3.1 presents the six studied degrees of freedom, namely the RF phase and field strength, the solenoid magnetic field strength, the installed aperture diameter and the charge releasing UV laser pulse power and spot size. Note, that the laser parameters are always referred to as (laser) spot and the particle beam as (electron) bunch. Additionally, there are the quadrupole strength and laser pulse length, which have been studied too but not in a comparable fashion.

Table 3.1.: Studied machine parameters for finding beneficial working points.

Machine parameter	Influenced bunch parameter
RF field phase	momentum profile
RF field strength	momentum
Solenoid field strength	focus point
Aperture	beam truncation
Laser power	bunch charge
Laser spot size	initial bunch size

3.1.3. Boundary conditions

As boundary conditions, we must consider limits for machine protection. This restricts a) the upper limit of the RF field strength and b) the laser damage threshold. It's also essential to ensure that the charge density on the YAG screen does not fall below the detectable limit.

The laser pulse length could be considered a free parameter. In the optical path of the UV pulse, a quartz rod is installed for dispersive stretching of the laser pulse. Several quartz rods with different lengths are available. As the laser pulse length increases, the electron bunch length also increases, facilitating commissioning in two aspects: This reduces the charge density, resulting in lower transverse emittance, which makes focusing easier. With a longer electron bunch, it becomes easier to achieve temporal overlap between the bunch and the streaking field. Therefore, for commissioning, we consistently utilized the longest available quartz rod for creating the longest possible laser pulse length. After successful commissioning the pulse length and thus the electron bunch length will be reduced again.

Due to the steep dependency of q_{in} on the bunch size, the solenoid strength was determined always for minimizing bunch size in the IP.

3.1.4. Optimization procedure

In general, the problem could be globally optimized using a multi-objective optimization (MOO) approach. An example where a Pareto front was found by simulations and successfully pursued in an experiment is provided in [41]. A similar network has already been developed and published for FLUTE, with four degrees of freedom, but for a different research question [42]. However, implementing this approach with a total of eight independent degrees of freedom is overwhelmingly computational expensive.[2]

---

[2] The simulations required to train the NN with four input parameter took about 10 hours, while the simulations for eight input parameters would require about 14 years![42]

Table 3.2.: Summary of simulation settings. The scanned parameters are listed as intervals, fields marked with "*" are optimized for every scan step.

Scan	Spot size [μm]	Charge (pC)	RF grad (MV/m)	RF phase (°)	Sol (mT)
RF phase	270	1	75	[-18;10]	*
RF grad	270	1	[60;85]	*	*
Laser power	60	[1;20]	77	*	*
Spot size	[25;800]	{1,4,11}	77	-8	*

For this thesis, four linear simulation campaigns were conducted, involving the scanning of

1. the RF phase,

2. the RF field strength,

3. the laser power and

4. the laser spot size.

The linear scans allow to grasp the complex behaviors in the beam dynamics which is essential for the experimental commissioning. Within each step of an optimization campaign, an inner loop was executed to optimize the solenoid strength for minimizing the bunch size at the SRR position. In two out of the four campaigns, an additional, second inner loop was run to optimize the RF phase as well. An overview of the campaigns is provided in tab. 3.2, where the scanned parameter ranges are labeled with interval brackets, and the intrinsically optimized parameters are marked with a "*" sign.

These inner optimization processes involve adjusting the solenoid field (or the RF phase) many times and then conducting a series of slightly alternated tracking simulation. From this series the solenoid strength and RF phase for the smallest bunch size at the SRR position, the IP, can be evaluated with the precision of the series steps. Because both these parameter, the solenoid field and the RF phase have a predictable impact on the beam, a model based on the scan results was created using polynomial fitting[3]. The fit models allowed for a more detailed optimization than the scan steps granularity. Meaning the optimization simulations can be done e.g. by changing the solenoid field in steps of 10 mT. With the model fitted onto the stepped simulation outcomes, the ideal solenoid field can be evaluated exactly.

With these inner loops, a campaign can be discussed regarding how the smallest possible bunch size (or q_{in}) changes by varying one degree of freedom.

---

[3] The actual degree of the polynomial model depends on the actual case, usually a clear optimum could be resolved with a degree of 4.
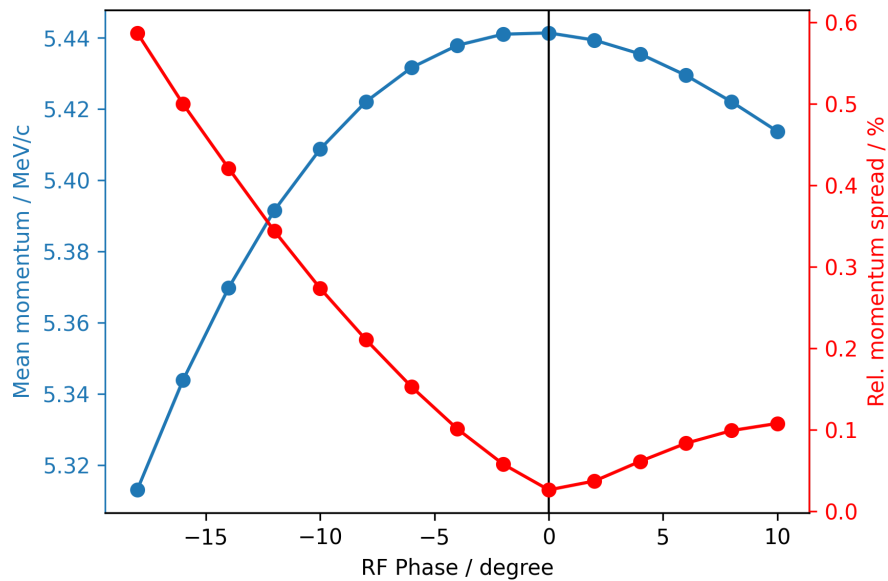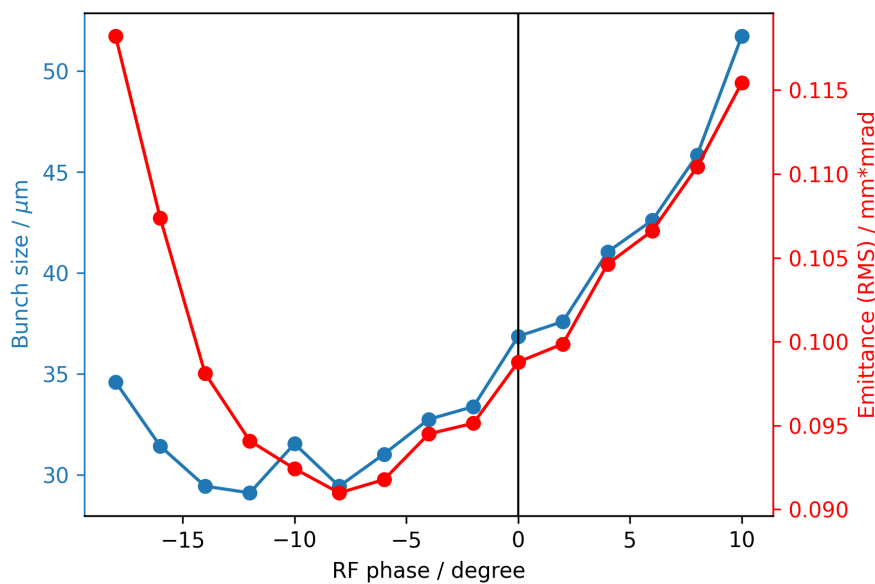
Figure 3.4.: Results of a simulated phase scan with the solenoid optimized for every phase step, displayed are the bunch mean momentum (blue) and the momentum spread (red). The vertical black line indicates the phase for highest bunch momentum and defines the phase zero position.

3.2. Scan of the RF phase

The first simulated parameter scan changes the phase of the RF field in the photoinjector with respect to the laser arrival time. The RF phase affects the charge release from the cathode and the field amplitude for the electrons energy pick-up. Both aspects have been detailed before in section 1.1.1 for a broad phase window of 130°, to introduce the overall mechanics. However, for the simulation campaign, the RF phase is investigated only in a narrow window of 30°. Outside of that window, the bunch momentum spread or the charge uncertainty grows so strong, that precise operation is not possible anymore. This has been tested in both, simulations and experiment. For this simulations, the bunch charge is set to be 1 pC, changes of the charge to the beam dynamics are discussed in a later measurement campaign.

Phase offset: The RF phase offset follows different definitions in both, simulations and the experiment. For this thesis, the RF phase is defined with 0° equals the phase for ideal acceleration and thus, maximum momentum. There are several factors that can cause the phase of highest energy to shift, such as the RF field strength or charge, therefore the offset must be determined individually for each scan. The zero position is marked with a vertical, black line in the plot.

Momentum response: The RF phase affects the bunch momentum spread and deviation over the bunch's longitudinal expansion and with that, affecting fundamentally the beam

Figure 3.5.: Result of a simulated phase scan with the solenoid optimized for ideal focusing in every phase step. The resulting bunch size (blue) and emittance (red) is shown. The phase offset is set at maximum energy and marked with the black line.

dynamics. The course of the bunch mean momentum and momentum spread over a phase scan is shown in fig. 3.4. The momentum has a clear maximum, which lies per definition at phase zero. In this setup, the momentum spread minimum lies at the same phase. For negative phases, the momentum falls steeply, and the moment spread increases sharply. In this half, the bunch head is generated with higher momentum than the bunch tail. This leads to velocity debunching, which relaxes the charge density and thereby inhibiting destructive space charge forces. For positive phases, the moderate decrease in momentum and increase in momentum appears advantageous. However, this regime leads to velocity bunching, which increases space charge forces, leading to a growth of emittance and thus to worse focusing possibilities.

Bunch size response: The simulation steps are evaluated at the IP. Figure 3.5 shows the evolution of the bunch size (blue) and its RMS emittance (red) at the SRR position during this scan. With negative RF phase values, the bunch length (not plotted) increases steadily by up to a factor of 2.5 within the investigated phase window and thus reduces the early SC forces, this is beneficial for the beam quality. Yet the momentum drops and the momentum spread rises which is unfavorable for the beam quality. Because of these contrary acting developments, the emittance shows a minimum below the phase for maximum acceleration, at $-8°$ and as a follow up, the optimized beam size has its minimum at $-12°$. Note, that these values depend on the machine working point and differ if the RF field strength or the charge changes.
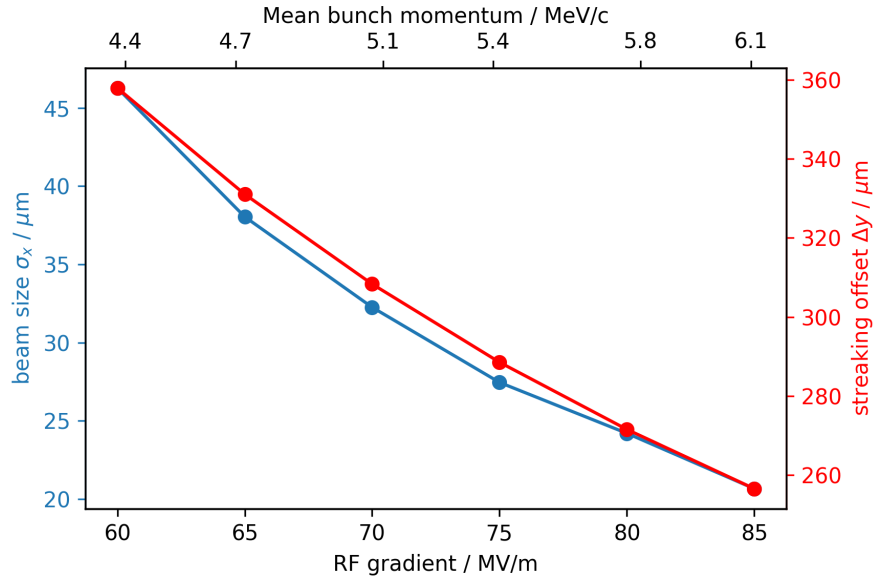
Figure 3.6.: Simulation scan of various RF field strengths. In each scan step, the RF phase and solenoid field are optimized for smallest bunch size (blue) at the IP. The calculated streaking offset is shown in red. The mean bunch momentum can be read from the second horizontal axis label (top).

Conclusion: For both strategies, contrast and brightness optimized, the most favorable working point lies at the RF phase for the smallest bunch size. However, the difference between this phase and the phase of minimum emittance is negligible in terms of beam quality.

3.3. Scan of the RF field strength

The previously discussed phase scan was conducted with a constant RF field strength of 75 MV/m. This scan was repeated for different values of the photoinjector field strength.

The RF field strength primarily determines the bunch momentum. With increasing momentum the space charge forces are suppressed. As a follow up, higher momentum shrinks the emittance, the bunch can be focused better and diverges less. Yet a draw back for higher energies is a more rigid beam, recalling equation 2.50:

$$\Delta y = d_{\text{drift}} \, p_y / p_z \tag{3.2}$$

reveals that a higher forward momentum suppresses also the streaking offset on the beam screen.

The optimized bunch size and the calculated, expected streaking amplitude according to the aforementioned equation are plotted in fig. 3.6. Within the simulated phase window, the applied RF field strength and the mean bunch momentum are connected almost linearly, the plot shows the bunch momentum as a second x-axis.

(a)   (b)
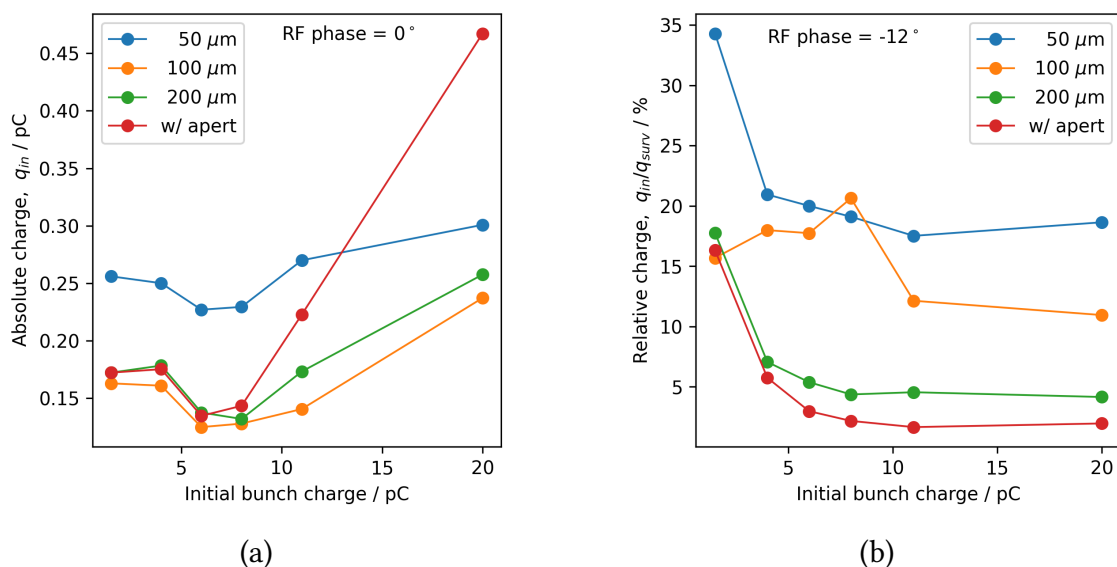
Figure 3.7.: Simulation scan of various applied aperture diameters, represented by different colors for different initial bunch charges. The solenoid field is optimized for maximum charge inside the SRR gap. The RF phase was chosen as $0°$ in a) and $-12°$ in b). Subfigure a) presented the absolute charge inside the gap q_{in} and subfigure b) shows the charge inside the gap, relative to the remaining charge, surviving the aperture q_{in}/q_{surv}.

Conclusion: By increasing the bunch momentum from $4\,4$ to $6.1\,\mathrm{MeV/c}$, the simulated bunch size but also the expected streaking amplitude drop. The bunch size shrinks to $45\,\%$ of its initial value while the streaking amplitude shrunk only to $72\,\%$ of the original value.

Here the small reduction of streaking amplitude is a relatively small price to pay for the strong reduction in beam size. As a conclusion it is clear that a high momentum is desired. Recalling the strongly non-linear relation between the bunch size and the charge inside the gap strengthens this argument further. In the experiment the bunch momentum was limited to a maximum of around $5.5\,\mathrm{MeV/c}$.

3.4.   Scan of the bunch charge

This simulation campaign discusses the influence of varying initial bunch charges in combination with three different aperture sizes. The released bunch charge is affected by almost every single machine parameter. Yet the laser power affects solely the charge production and can be used to adjust the charge to the desired value after all. The round aperture hole, with a diameter 50, 100 or 200 µm, is installed 8 cm before the resonator. The electrons colliding with the aperture body are completely stopped.

The campaign contains tracking simulations for different initial bunch charges and for three different aperture diameters. Intrinsically these simulations hold also the information of tracking simulations without an aperture. In the simulation software, the particles

blocked by the aperture are marked with a flag. From this point on, the lost particles are still tracked further on as passive particles, which does not interact anymore with the rest of the bunch.

This setup was simulated for a range of different RF phases. The relative RF phase for maximum momentum shifts with the initial bunch charge, because of that, the relative phase offset was reevaluated for every initial charge individually. For every combination of initial charge, aperture and phase, the solenoid was optimized with an inner loop for maximizing q_{in}, the charge inside the SRR gap, after the bunch is truncated by the aperture.

In total this campaign contains of around 4700 individual tracking simulations. After investigating this extensive campaign, the results can be summarized by the two plots, shown in fig. 3.7. Subplot a) shows the absolute value of q_{in} for the RF phase of $0°$, the phase for highest bunch momentum. From all tested phases, the highest q_{in} values are achieved with this phase. Subplot b) shows the relation $q_{\text{in}}/q_{\text{surv}}$ which is the charge inside the gap, relative to the charge surviving the aperture truncation. This representation shows the results simulated with an RF phase of $-12°$, the phase of minimum bunch size. This phase lead to the highest amount of relative charge.

Discussion: In fig. 3.7 a) one can see, that the absolute q_{in} grows with both, initial bunch charge and aperture diameter.

For the brightness experiment, the regime of high initial charges is of great interest. When comparing the case with a 200 µm gap to free flight for a 20 pC bunch, it becomes apparent that the absolute charge within the gap increases by a factor of 2, while the relative fraction decreases by a factor of 2. Trends suggest that with even higher initial charges, absolute q_{in} continues to increase, while the relative q_{in} changes barely. Consequently, for the brightness experiment, high initial charges without aperture or with a larger aperture diameter provide good streaking conditions.

On the other hand, for the contrast experiment, low initial charges have been investigated. It was observed that relative q_{in} values are high for small initial charges. Trends indicate that a high relative q_{in} value is achieved with small aperture diameters.

Discussion of ASTRA anomalies: While studying the plotted data, one can find several anomalies.

1. At initial charges of 6 up to 11 pC, there is a notable drop in the absolute q_{in} values across all curves.

2. For initial charges below 11 pC, the curve for the 100 µm aperture does not follow the general trend.

3. The curve for the 50 µm aperture yields disproportionately high absolute charges.

69
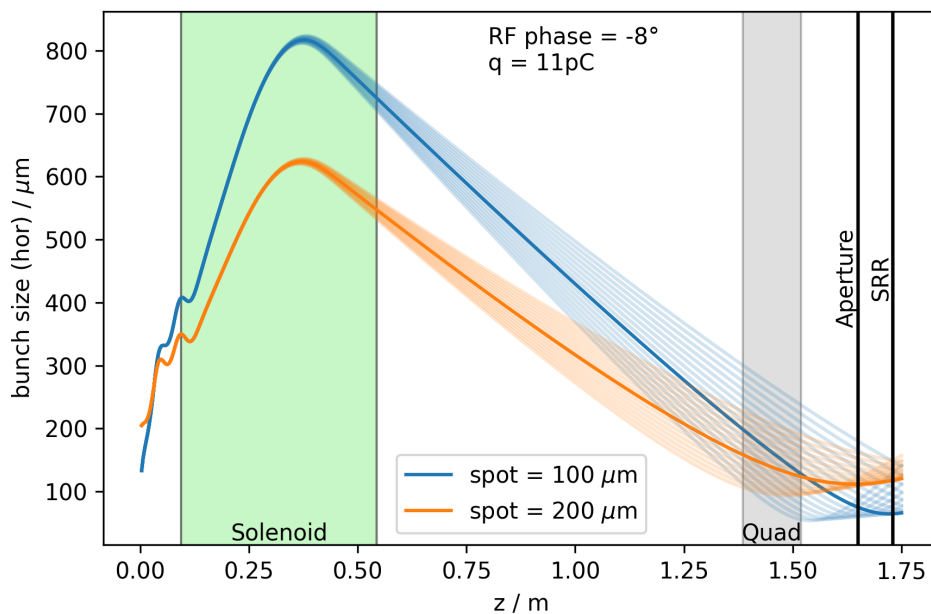
Figure 3.8.: The course of the bunch size for a laser spot size of 100 (blue) and 200 µm (orange) for a 11 pC bunch and an RF phase of $-8°$. The array of semi-transparent trajectories represent interim results of the solenoid optimization, the bold trajectory indicates the trajectory with smallest bunch size at the SRR. The range of magnetic fields (including fringe fields) is marked for the solenoid (green) and the quadrupole (gray, not used in this campaign).

In particular, the last point suggests that the results obtained from ASTRA may not represent physical solutions. Potential reasons for this phenomenon could include binning effects, especially in the regime of substantial particle losses, although a precise explanation has not yet been established. One approach to validate these findings is to compare them with results from other software that also calculates space charge effects, such as OPAL [43]. It is suspected that the fundamental statement, the tendencies for favorable operating points, remains valid, even though the absolute values should be interpreted with care.

Conclusion: For the brightness optimized experiment, a maximum of absolute q_{in} is achieved with the RF phase of $0°$ (phase for highest momentum), high initial charges and a large aperture diameter or even without an aperture after all.

For the contrast optimized experiment, a maximum of relative q_{in} is achieved with the RF phase of $-12°$ (phase for smallest spot size), low initial charges and a small aperture diameter.

3.5. Scan of the laser spot size

This last simulation campaign discusses the influence of different initial laser spot sizes. The spot size was varied within the region of experimentally achievable values. The RF

field strength and phase were constant during the entire campaign, the phase was set to $-8°$ for a minimum emittance. The solenoid was optimized for minimum bunch size at the IP in every step. The scan was repeated for three different charges, 1.5, 4 and 11 pC[4], during a scan the charge is kept constant. Note, that in the experiment the released charge drastically grows by increasing the spot size. The absolute charge value however can be controlled freely by adjusting the laser power.

Development of the bunch size: By altering the laser spot size, the beam dynamics change in a complex way. For a better understanding, first a simple subset of the campaign is discussed. In fig. 3.8, the evolution of the 11 pC bunch's size along the accelerator's z-axis is plotted for an initial laser spot size of 100 μm (blue) and 200 μm (orange). The plot indicates the positions of the SRR, the aperture, and the regions of the magnetic fields (including extensions from fringe fields). The aperture and quadrupole are not used in this campaign but plotted for completeness. The two curves are complemented by an array of additional semi-transparent trajectories, which correspond to the various traces from the internal solenoid optimization. The bold lines represent the optimization results, the traces with the smallest bunch size at the SRR.

For this discussion, two parameters are introduced: σ_{max}^{sol} represents the maximum bunch size located within the solenoid, and σ_{min}^{SRR} is the minimum bunch size for optimal focusing on the resonator. This example shows, that the bunch, created with a 100 μm laser spot, diverges so strong, that it's bunch size surpasses the size of the bunch, created from a 200 μm laser spot, already within the first 5 cm of travel. The first bunch reaches a greater σ_{max}^{sol} and with that a smaller σ_{min}^{SRR}.

This can be explained through linear beam dynamics. For a given emittance, the minimum beam size at the focal point σ_{min}^{SRR} is anti-proportional to the beam convergence upon approaching the focal point. Since the distance between the solenoid and the SRR is fixed and the solenoid is always adjusted to keep the focus point at the SRR, the convergence is directly proportional to the beam size in the solenoid σ_{max}^{sol}. This leads to the in-between result, that σ_{min}^{SRR} is anti-proportional to σ_{max}^{sol}.

The fig. 3.8 shows the evolution of the bunch size along the accelerator z-axis, with the extreme values σ_{max}^{sol} and σ_{min}^{SRR}. Numerous simulations of this nature with varying laser spot sizes have been conducted in this campaign, and both parameters were collected for all simulated spot sizes, they are shown in fig. 3.9. Additionally, the emittance (at the SRR), is included as a subplot beneath. The plot shows the anti-proportional relation between σ_{max}^{sol} and σ_{min}^{SRR} from the above stated in-between result. The extreme points of the curves are slightly offset. The minimum beam size is also proportional to the bunch emittance, which increases with the applied laser spot size and therefore shifts the maximum position of σ_{min}^{SRR}.

A bunch created with a photocathode has an initial bunch size and emittance offset, both are proportional to the laser spot size. The bunch size but also the emittance grow during

---

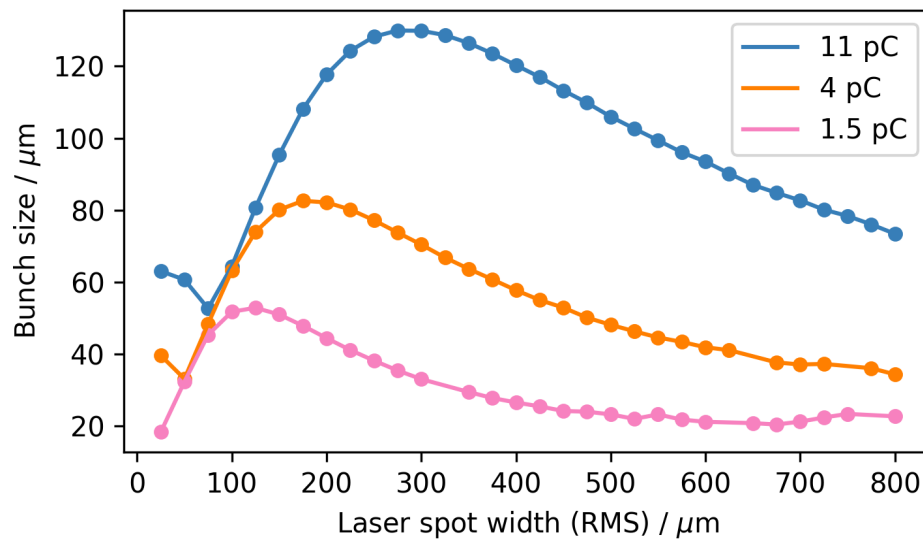[4]   There is no specific reason behind these actual values.
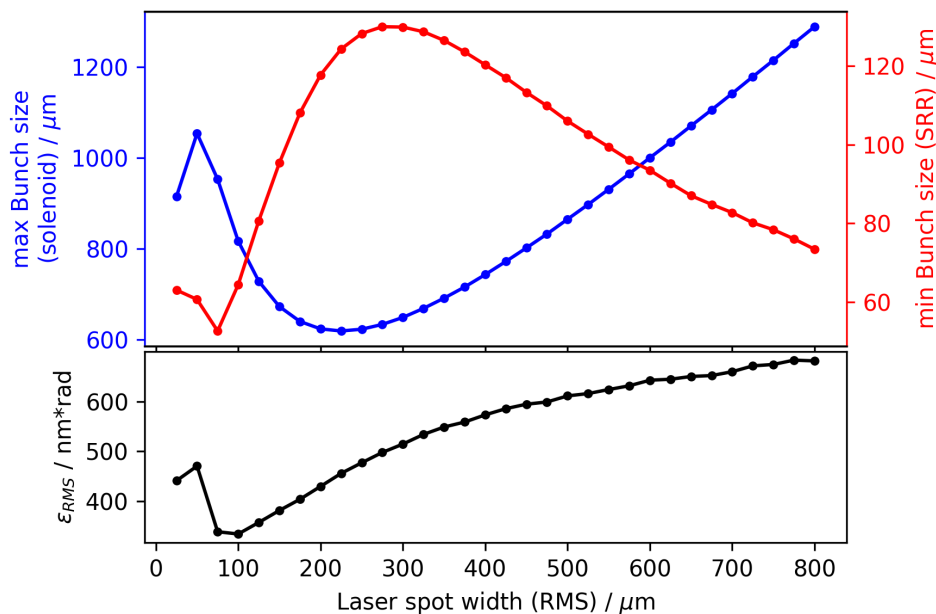
Figure 3.9.: Simulation scan of various laser spot sizes. The solenoid field is optimized for minimizing the bunch size in the IP, the charge is 11 pC, the RF phase is $-8°$, the phase of minimum emittance. The maximum bunch size within the solenoid (blue) and the minimum bunch size at the SRR (red) are shown, the RMS bunch emittance is attached in a subplot beneath.

the transport through the RF photoinjector because of the repelling SC forces, these dynamics are discussed in great detail in [44, 45]. With increasing spot size, the bunch size and emittance offset are increased but their growth is inhibited. These two contrary acting tendencies lead to a minimum in $\sigma_{\mathrm{max}}^{\mathrm{sol}}$ and in a knee in the emittance at around the same spot size. Between these two distinct positions, $\sigma_{\mathrm{min}}^{\mathrm{SRR}}$ has its maximum, where the focusing conditions are worst.

Conclusion: The simulation campaign repeated for three different charges: 1.5, 4 and 11 pC, the minimum bunch size $\sigma_{\mathrm{min}}^{\mathrm{SRR}}$ for all charges is plotted against the applied laser spot size in fig. 3.10. Higher bunch charges just shift and upscale the bunch size courses, otherwise the dynamics appear static. This simulation campaign reveals diverging results for the two optimization strategies.

1. For the contrast optimized experiment, the minimum laser spot size is favorable, because they lead to the smallest bunch size and to the smallest emittance.

2. For the brightness experiment a high charge is favorable as discussed previously. For creating high bunch charges, the laser spot should be less focused for machine protection reasons. In order to create the desired high bunch charges and a low bunch size at the SRR, the laser spot size should be chosen as large as possible.

As a final remark, this campaign was studied at the phase of minimum emittance. A cross check for with different RF phases will be a valuable addition as a future study.

Figure 3.10.: Simulation scan of various laser spot sizes. The solenoid field is optimized for minimizing the bunch size in the IP, the RF phase is −8°, the phase of minimum emittance. The minimum bunch size at the SRR is shown for three different charges: 1.5, 4 and 11 pC.

Table 3.3.: Summary of the simulation campaign results for the examined parameters for the two optimization strategies *contrast* and *brightness*.

	RF phase (degree)	Field strength (MV/m)	Spot size (µm)	Charge (pC)	Aperture (µm)
contrast	-10	max	≤100	≤5	50
brightness	0	max	≥500	≥20	≥200

Discussion of anomalies: All shown bunch parameters show a sudden jump for very high charge densities, namely for 11 pC (or 4 pC) and spot sizes below 80 µm (respectively 50 µm), this anomalies could not be explained so far. It is not clear if this sudden change in trend really represents a physical behavior or if this is a succession of simulation artifacts. Since these setting are barely achievable in the experiment, this kink is not a major concern.

3.6. Summary

After discussing these four simulation campaigns, a clear conclusion can be drawn regarding the examined parameters. The findings have already been presented individually in each section and are now summarized concisely in tab. 3.3.

4. The experimental procedure and analysis

For the feasibility study the previously elaborated beam dynamic strategies are tested experimentally. For a detectable streaking signal, relative high amount of the bunch charges have to be focused and guided through the resonator's $20 \times 20\,\mu\text{m}$ gap. Further, the boundary conditions have to be fulfilled, namely the temporal and spatial alignment of the electron bunch and the THz pulse at the Interaction Point (IP), the gap of the TDS resonator. These requirements can be met partially through precise pre-alignments and daily checks. The THz spatial alignment however cannot be verified exactly, since the TDS experimental chamber needs to remain sealed for the vacuum level. Therefore the alignment of the THz pulse can only be verified before entering the experimental chamber. To address remaining uncertainties, the experiment has been systematically repeated at different alignment positions, effectively stepping through a 2D raster of these parameters. This process and the automated data acquisition is hereafter called the Raster Alignment Program (RAP). Section 4.1 elaborates on the challenges associated with the alignment processes.

To achieve a measurable streaking signal, a sufficient relative amount of charge must be focused and guided through the resonator gap. Additionally to the two working points, namely *contrast* and *brightness*, also four additional working points have been investigated experimentally. Section 4.2 discusses the motivation of the six working points and their experimental outcomes.

Among the tested six working points, three have been suitable for an extensive RAP experiment. Section 4.3 discusses the RAP experiments and the data analysis.

4.1. Prerequisites

During the delicate micrometer and picosecond alignment, it has been observed that many assumptions on several machine components are incorrect. Assumingly isolated parameters reveal cross-correlations with bunch parameters that one would not intuitively assume.

For example, changes in the laser spot size inflict a slight shift of the laser position on the cathode, invoked by just a tiny inaccuracy of the alignment of the movable focusing lens. Consequently, the electrons are released off-axis. The focusing properties of the

RF field act radially on the entire bunch and therefore driving it towards the fields axis. This example shows, how changes in the laser spot size lead to an deviation of the beam angle.

Of course, this influence is vanishingly small, so small that for standard accelerator operations no one ever noticed this correlation. Yet, we do. In fact, every machine parameter somehow influences the bunch alignment. I will spare the reader further details here. For the exceptionally high precision required for the TDS experiment, we are required to find and account for such dependencies.

4.1.1. Machine instabilities

Beside the mentioned cross-correlations, the bunch alignment is also sensitive to machine instabilities. In general, most machine parameters are inherently stable only up to a certain degree and the FLUTE instabilities are acceptable for a normal accelerator operation. Yet the TDS experiment encounters a significant challenge in maintaining stable enough conditions for its high requirements. The encountered machine instabilities can be categorized into three types:

Jitter: Fast disturbances, such as air movement on the laser path, cause the laser pulses, and as a follow up, the beam parameters to fluctuate from pulse to pulse around a mean value. To mitigate jitter instabilities, the experiment observables are not individual screen images but averaged images, composed from a series of single bunch profiles.

Drift: Slow processes, such as heating up of the clystron, lead to a gradual drift of several beam parameters mean values. To mitigate drift instabilities, key alignments are checked frequently, as discussed in the following section.

Breakdowns: The breakdown phenomena may be caused from RF-breakdowns. Heat and particles emit into the photoinjector cavity, worsen the vacuum level. Occasionally they are accompanied by an electric discharge or arc in the photo-injector. The machine response on breakdowns is unpredictable, usually it makes multiple different machine parameter jump to a new value, some of them may jump back soon, some recover over time and sometimes, some parameters just stay on a different level. Meaning it is possible, that suddenly the RF power output drops by 10 % and just stays there until it is discovered.

To give an example of the instabilities effects on the alignment, the horizontal bunch position was recorded on the SRR YAG screen for 15 hours during a *contrast* experiment. The data is presented in fig. 4.1 in form of a median value and the range of the 95 % confidence level around it, calculated as a moving average with a subset size of 50 individual data points. One can see how the bunch position constantly jitters in a band of around 100 µm around the median and how the median drifts slowly in the order of 100 µm over the course of hours. Also one can see several sharp jumps of the bunch position caused
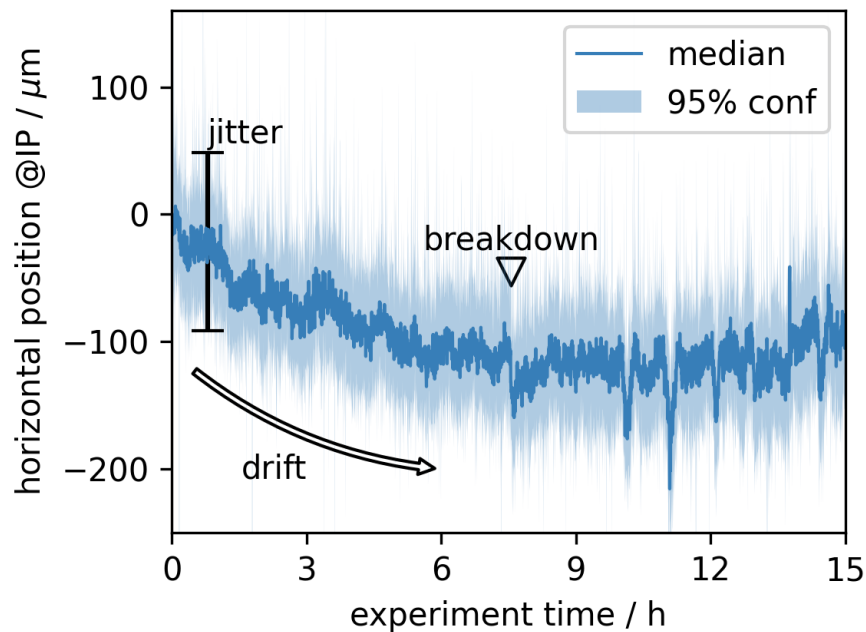
Figure 4.1.: Measurement of the horizontal bunch position at the interaction point, recorded with the YAG screen inside the TDS chamber. The position median and 95 % confidence range are shown for a moving data subset of 50 data points. Three different instabilities can be seen: Jitter leads to a large confidence range, drift changes the median location over time and breakdowns lead to sudden interrupts.

by breakdowns, one marked at around the 7th hour. After the breakdown, the median position slowly recovers its former state from before the jump. In the marked example, this process takes around half an hour.

So far, it has not been possible to identify the extent to which the instabilities of individual machine parameters affect the beam stability.

4.1.2. Laser spot alignment with RF and solenoid fields

As previously mentioned, an off-axis bunch experiences radial forces from the RF-field and also from the solenoid field towards the electrical respectively the magnetic field axis. If this is the case, the beam path is sensitive to jitter in both field strengths and also to jitter in the bunch momentum which affects the beam rigidity.

A procedure was developed to the align beam path with the RF-field axis and with the solenoid magnetic axis onto one common "field-axis". To align these three components, two of them have to be moved to a correct position: the laser spot position on the cathode defines the beam starting point and the entire solenoid can be moved by its motorized stand. Changing the position of the RF photoinjector is not possible due to the rigid RF waveguide system.

The correct alignment of the field-axis can be confirmed using a YAG screen: if the electron bunch changes size but maintains its position on the screen while altering the RF power or solenoid strength, the alignment is perfect. Apparently, the field axis becomes misaligned after some time, and the alignment process needs to be repeated. Therefore, it has become part of a daily routine.

4.1.3. Beam alignment at the interaction point

Because of the drift instabilities, it is essential to frequently verify key alignments at the IP, explicitly:

1. The spatial alignment of the electron bunch.

2. The spatial alignment of the THz pulse.

3. The temporal synchronization between THz and electrons.

1. Bunch spatial alignment: In general, the field-axis does not exactly match the "geometric axis" of the accelerator beam pipe, along which the IP is located. The beam screens and the TDS resonator positions have been referenced on a micro-meter level with a laser-based alignment procedure, this allows to identify the accelerator geometric axis [46]. Behind the solenoid, the beam path is redirected to follow the geometric axis of the accelerator, employing two horizontal and two vertical corrector magnets. The spatial alignment of the electron beam can be verified by two YAG screens. In the TDS chamber, the SRR can be replaced by a YAG screen to confirm the beam position directly at the IP. The forward YAG screen is located at the end of the beam pipe and reveals a remaining angle in the beam path. Depending on the chosen working point, the forward YAG screen can also serve as an additional verification tool. If the bunch size is considerable large, the shadow cast by the SRR and its gap onto the beam screen image can be identified, confirming a successful alignment.

2. THz spatial alignment: The THz pulse is precisely aligned with the IP as described in section 2.1.1, by swapping the SRR with a THz sensor. This process requires opening the vacuum chamber and is therefore very time-consuming. It takes several days until the vacuum level is again good enough for bunch operation. A daily check of the THz pulse position and angle, right before entering the vacuum chamber was carried out. This check was done by centering the THz pulse simultaneously at two distant iris apertures on the optical table, by hand.

In this technique, the position and angle of the THz pulse can only be determined with limited precision. Given the horizontal orientation of the entire laser setup, errors in the verticle plane are intrinsically well suppressed. As the IP is approximately 30 cm worth of laser path behind the last iris, a residual and unavoidable uncertainty remains in the horizontal alignment of the THz pulse. Since the THz pulse cannot be steered remotely,

the SRR and with it the IP is shifted As a solution, the spatial THz alignment is one out of two scanning axes in the RAP experiments.

3. Synchronization: The temporal arrival of the electron bunch was synchronized with the THz pulse at the SRR during a complex experiment by M. Nabinger [29]. The electron pulse was steered to collide with the resonator body intentionally, creating a flash of photons radiated in every direction. A fraction of this light found its way upstream along the THz path, through the incoupling window onto the optical table outside of the accelerator. A fast THz detector was installed such, that it detects the arrival time of both, the laser-generated and the electron-generated THz pulse. By considering the time of flight from the IP to the detector, these signals were used to set the (laser-generated) THz delay such, that the synchronization criterion at the IP is met.

This synchronization check is time-consuming to set up and the installed beam splitter leads away valuable power of the THz pulse, therefore this experiment was carried out just once. To account for a potential systematical error in this experiment or a shift of the ideal synchronization over time, the THz delay stage was the second scanning axis in the RAP experiments.

4.1.4. Raster Alignment Program tool

As previously explained, the alignment prerequisites can be certainly verified only for electron alignment, while spatial and temporal THz alignment can be confirmed only partially. The RAP scan is visualized in fig. 4.2, which repeats the streaking experiment at different positions for both alignment criteria in the form of a 2D scan.

Axis 1, THz delay: The first RAP axis delays the THz pulse in its arrival time with the delay stage, located in the IR laser path in the THz arm. Great care was taken to ensure precise alignment of the stage so that moving the stage does not affect the horizontal position of the laser. The estimated precision of the synchronization pre-alignment is assumed to be around ±1 cm worth of laser path, corresponding to approximately ±33 ps in time.

We agreed on an asymmetric scanning range of $[-2\Delta t; +1\Delta t]$, where a negative delay time indicates that the THz pulse arrives earlier at the IP than the electrons. Having the THz pulse arriving before the electron bunch is more likely to produce a streaking signal than the other way around, because, the streaking field rise time is much faster than the decay time. The actual scanning range is set differently for each RAP experiment but at least $\Delta t \geq 83$ ps [1]. The streaking field lifetime is 4.3 ps and the expected bunch length is around 1 ps. Since the delay stage is scanned in steps of 0.2 mm, corresponding to 1.3 ps, the

---

[1] The actual applied values depended on the available machine time. Even longer scan axis could be selected for RAP scans that have been run over a weekend for example.
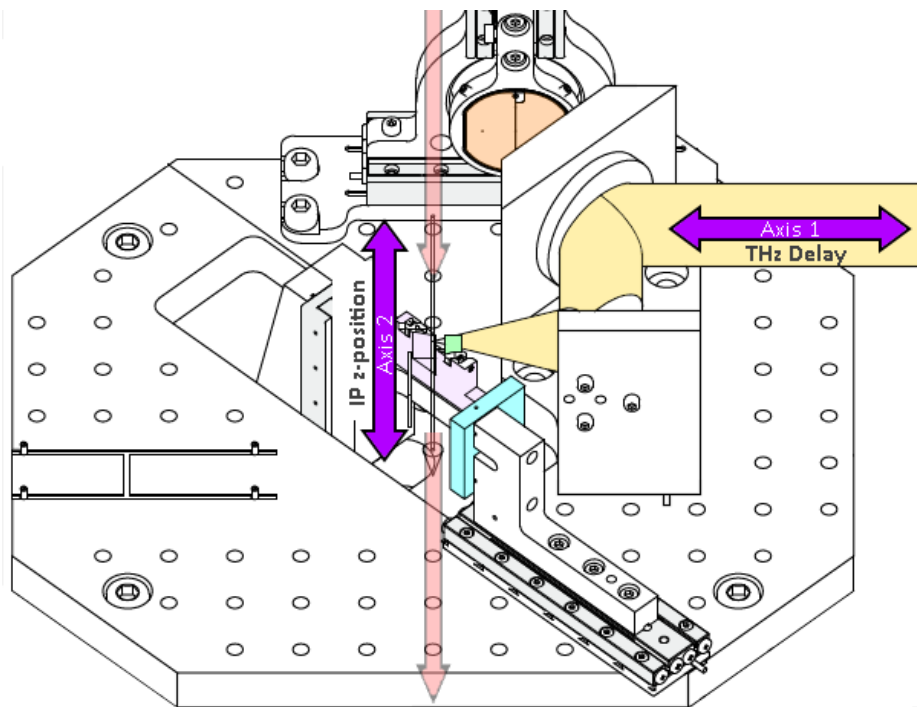
Figure 4.2.: Representation of the two scanning axes during a RAP scan. Axis 1 changes the THz temporal delay and axis 2 moves the SRR in z-direction to change the IP horizontally for the THz pulse but not for the electron path. The motor axes are diagonally aligned, for a movement of axis 1, two motors are driven together.

synchronization should allow streaking for at least four consecutive scan steps somewhere within an axis-1 scan.

Axis 2, SRR z-position: The second axis shifts the SRR in the z-axis (the direction of the electron bunch path), causing the IP to move horizontally against the THz pulse, while preserving the electron alignment with the IP. The installed stepper motors are aligned diagonally, for a movement of axis 2 actually two motors are moved alternately. The motor axis have been discussed in section 1.4 and are presented in fig. 1.7.

The THz pulse has a diameter of 2 mm [2] and the resonator width is 80 μm. We scanned the SRR position in the range of ±1 mm with 0.5 mm steps around the pre-aligned position. From this setup, a good coverage of the resonator by the THz pulse should be ensured for a 2-3 consecutive scan steps within an axis-2 scan.

The scanning processes for both axes are shown exemplary for one contrast optimized RAP experiment in fig. 4.11. Conducting such a RAP scan ensures that the streaking experiment is definitively performed several times with correct alignment. A single scan of axis 1 can take more than three hours due to the data acquisition per scan step, making the entire scan duration up to 20 hours long, depending on the actual settings. Of course

---

[2] In the measure of $1/e^2$, see paragraph 2.1.1.2.

this extensive scan is only possible for stable beam operation, which is why it could be executed only for a selection of working points.
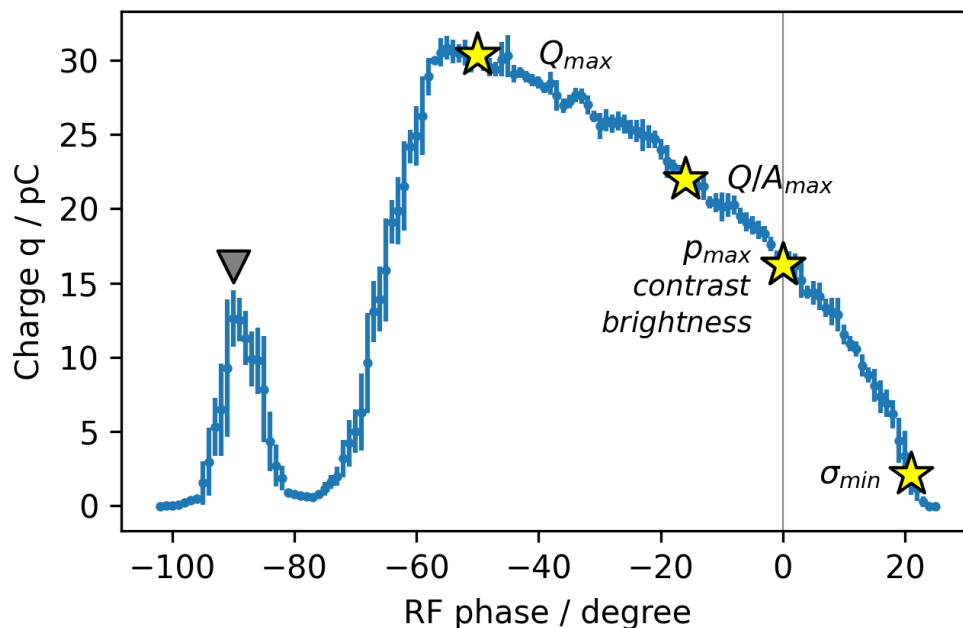
Figure 4.3.: Bunch charge measured with the ICT during an RF phase scan. The phases of the investigated working points are marked and labeled. The sharp sidebump maximum (gray triangle) is used for identifying the daily changing phase offset in the control system.

4.2. Experimental procedure

Six working points were experimentally investigated, with two previously introduced as *contrast* and *brightness*. The remaining four working points vary according to the selected RF phase, chosen to optimize a specific bunch parameter which defines the working point names.

Q_{max}: Operates on the RF phase for the maximum bunch charge.

Q/A_{max}: Operates on the RF phase experimentally found, for the highest charge per area ratio at the IP.

p_{max}: Operates on the RF phase for the maximum bunch momentum.

σ_{min}: Operates on the RF phase for the minimum bunch size at the IP.

The working point *brightness* was previously motivated to operate at the phase of $0°$ which is the same phase as for p_{max}. The working point *contrast* was considered to operate at $-10°$. Nevertheless, we decided to also operate this working point at $0°$ to have three working points at the same phase with different laser spot sizes.

The RF phase defines the broad majority of beam dynamics, as discussed in the beginning of this thesis in section 1.1.1. The measured charge during a phase scan discussed therein and shown initially in fig. 1.4 is presented again in fig. 4.3, supplemented with markers indicating the phases of each working point.

Table 4.1.: Summary of differing machine parameters among the tested working points.

WP	RF phase (°)	Spot size hor;vert (µm)	UV power (mW)	Charge (pC)
Q_{max}	-50	61;60	120	45.6
Q/A_{max}	-16	61;60	120	11.7
p_{max}	0	61;60	67	17.7
σ_{min}	21	61;60	67	4.0
brightness	0	199;141	362	171
contrast	0	48;45	61	9.3

The RF phase but also the laser spot size and the laser power influence the resulting bunch charge. In fact these are the machine parameter through which the working points differ. These machine parameters and the resulting, measured bunch charge are listed in tab. 4.1. Unfortunately, the laser power had to be reduced for machine protection reasons for the working points p_{max} and σ_{min}. Not included are machine parameters that are chosen identical for all WP:

- The RF power was set to the maximum available power considering machine protection boundaries of 5 MW, read back from a probe located inside the RF photoinjector. This lead to a bunch mean momentum of 4.3 MeV/c.

- The solenoid was always optimized for smallest spot size in the SRR plane.

- The quadrupole was not in use during this experiment.

The TDS experiment followed a clear routine for each working point.

1. The THz is aligned spatially with the IP.

2. The experimental hall is closed and the accelerator is started.

3. The UV laser is directed to the cathode center.

4. After starting the clystron, the RF phase has an arbitrary offset in the operation system. An RF phase scan is performed, and the charge maximum in the "sidebump" is identified and its RF phase is labeled as $-90°$.

5. Machine parameters for the working point are set.

6. The laser spot on the cathode is aligned with the RF electric field and solenoid magnetic field axis.

7. The electron beam is aligned spatially with the IP and parallelized with the geometric accelerator axis.

8. Measurement of bunch parameters in the working point: charge, beam size, momentum, momentum spread and emittance. The dipole and quadrupole magnets are cycled to avoid remaining magnetic fields invoked from hysteresis effects after a measurement.
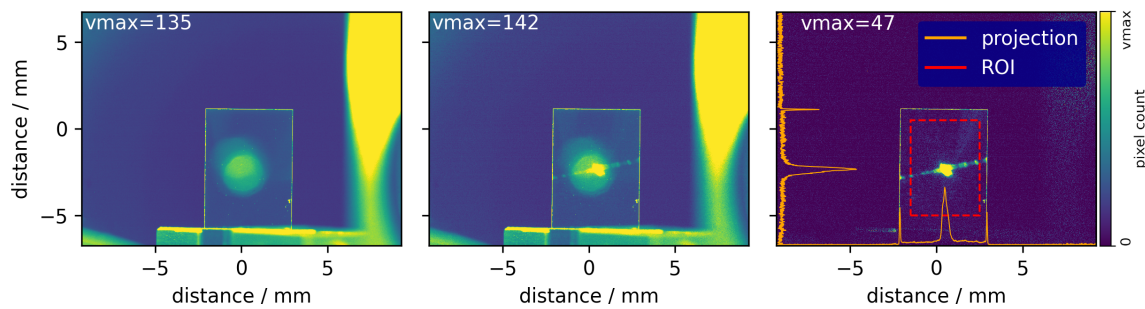
Figure 4.4.: Example for the bunch size measurement in the interaction point. The background image (left) is used to reduce the screen image with bunch (center) to the signal image (right). The signal image is complemented by the intensity projection for each axis (orange) and the selected region of interest (red) wherein the projections are evaluated. The colormap's upper end (vmax) is chosen dynamically as the 90 % quantile, the calculated vmax value is printed in each image.

9. Investigation which aperture diameters are feasible.

10. The THz is released to the IP, the THz shutter is set to periodically open and close.

11. Finally, the forward screen is observed simultaneously for instant screen images and averaged screen images. At the same time, the temporal synchronization between electrons and THz pulse at the IP is scanned.

The measurement of bunch parameters will now be described exemplary for the *contrast* working point.

Charge measurement: The charge is measured passively by the ICT. The charge is also a bunch parameter that suffers by drift and jitter effects. The values discussed in this thesis are collected from the measurement during the emittance measurement, presented as the charge average and the measured standard deviation. For the *contrast* experiment, the measurement yielded a charge of $q = 9.3 \pm 0.8$ pC. The uncertainty originates from statistical charge fluctuations over the curse of the measurement.

Unfortunately, an incorrect configuration in the ICT falsified the charge measurements to be only half of the actual bunch charge. Months after the experiment, this circumstance has been found and a data correction for the corrupted measurements has been elaborated. Of course in this thesis only corrected values are quoted.

Beam size measurement: During the electron spatial alignment process, the SRR is replaced with the YAG screen. At that moment, the beam screen image is used to evaluate the bunch size. The bunch size is determined through a script embedded directly in the control system. Initially, a series of several (typically 50[3]) screen images without an electron bunch is recorded, and the average image serves as the background, this is shown in fig. 4.4 with the leftmost image. Another image with electron beam is recorded, it is

---

[3] Sometimes fewer images than 50 are recorded to speed up the process.

shown in the center image. This image shows a straight line of charge hot-spots crossing the bunch center, which will be referred to as "horizontal, linear artifact", whose origin is unclear so far. It occurs consistently among a wide range of beam screen images and potentially also falsifies measurements of the horizontal bunch size and emittance.

The bunch size is then calculated from the difference image, as shown in the right image. A projection of the camera pixel counts onto the horizontal axis is calculated (orange). The beam size is then calculated as the 1σ width of the Gaussian profile fitted on the projection. In the same way, the vertical bunch size is calculated from the projection onto the vertical axis.

In the left and center image of fig. 4.4 one can clearly see the rectangular YAG screen on top of the aluminum holder. The bright edge on the right is an artifact from the mirror edge and can be disregarded. The background subtraction effectively removes the mirror edge artifact. Besides the bunch footprint only the brightened edges of the YAG screen are visible. Therefore, a Region of Interest (ROI) selection is chosen (red rectangle), the fitting routine only considers data from within this ROI.

Not for the data processing but for human readability, the screen images shown in this thesis are displayed with a continuous color gradient where the bright colors represent a high pixel count. The highest considered pixel count is called "vmax", it is chosen dynamically as a percentile of 90^4 of all pixel counts within an image and stated in the upper left or right image corner.

The measured bunch size is horizontal $\sigma_{\mathrm{hor}} = 160 \pm 6\,\mu\mathrm{m}$ and vertical $\sigma_{\mathrm{vert}} = 167 \pm 6\,\mu\mathrm{m}$. The uncertainties originate from statistical fluctuations during the size measurement. The uncertainty of the Gaussian fitting routine is not monitored by the control system. Exclusively for the two working points *contrast* and *brightness*, the screen was recorded for over an hour to gather meaningful statistics on different parameters, such as the just stated uncertainty on the bunch size in the IP.

Bunch momentum measurement: The fig. 4.5 shows three spectrometer screen images with the bunch deflected with different dipole strengths. The spectrometer images are presented such, that a positive horizontal position indicates a higher deflection from the linear accelerator axis and therefore indicates a lower particle momentum. In the leftmost image, the particles with the bunch's lowest momentum, positioned in the leftmost edge of the bunch, align with the screen center, likewise for the middle and right image.

From the beam alignment it is ensured, that the bunch enters the dipole in the geometrical center and without an angle. The momentum for particles reaching the screen center can therefore be calculated from equ. 1.2, the spectrometer magnetic field is calculated from the applied dipole current and a calibration curve. The three measurements yield a bunch center momentum of 4.32 MeV/c and a momentum range in the bunch between

---

[4]   For some images, the percentile level has to be adapted, e.g. for images, polluted by bright artifacts like in fig. 4.4.
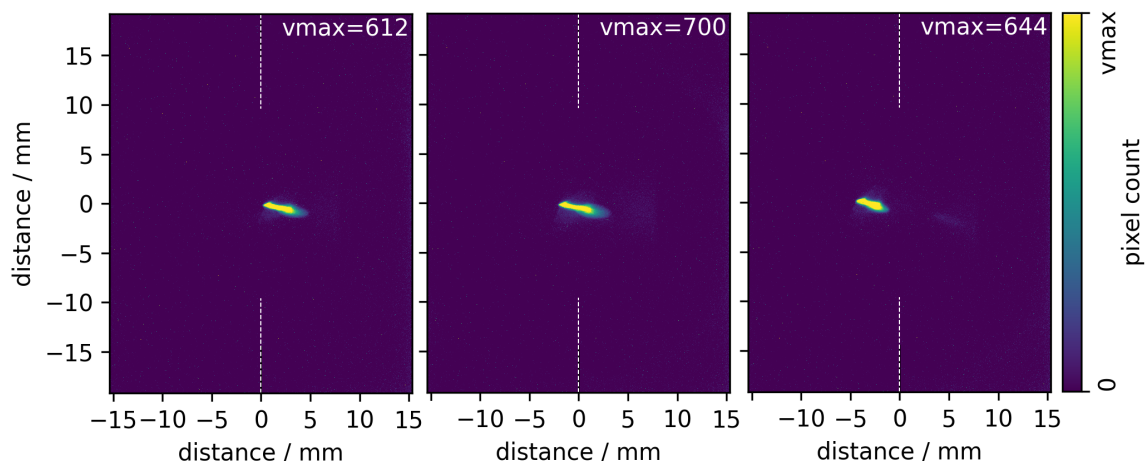
Figure 4.5.: Example for the bunch momentum and momentum spread measurement. Three spectrometer images show the spread bunch with different positions aligned to the screen center. Particles at positive x-values are deflected further from the original beam axis because of lower momenta. The images are sorted for the applied dipole field strength which decreases from the leftmost to the rightmost image.

4.28 MeV/c and 4.35 MeV/c.

The bunch momentum and the according relative momentum spread can therefore be expressed as $4.32\,\text{MeV/c}^{+0.7\%}_{-0.9\%}$.

A more detailed analysis of the energy spread requires a clear discussion about the precise identification of the bunch's leftmost and rightmost edge. Here the momentum spread plays only a subordinate role, therefore this rough estimation is sufficient.

Emittance measurement: For the emittance measurement, a standard technique known as quadrupole scan is used. The measurement principle and math are described in standard literature like [47], the explicit application at FLUTE was formulated in [19, 16]. The bunch size is recorded during a scan of the quadrupole current. From the beam size σ, the beam variance σ^2 is calculated. To compute the quadrupole strength $K1$, three contributors are required: the quadrupole current, a calibration curve and the bunch momentum. During the quadrupole scan, the beam variance follows the shape of a parabola. The beam sigma matrix can be determined from the curvature of this parabola, obtained through a simple polynomial fit, the emittance equals the determinant of the sigma matrix. The measured variance including statistical uncertainties and the fitted parabola are illustrated in fig. 4.6 for both the horizontal and vertical plane.

The calculation yields the RMS emittances at the position of the quadrupole: $\epsilon_{\text{RMS,x}} = 236 \pm 112\,\text{nm rad}$ and $\epsilon_{\text{RMS,y}} = 375 \pm 24\,\text{nm rad}$. The given uncertainty originates from the uncertainty of the parabolic fitting routine, considering also the statistical uncertainties of the bunch size measurements.

The measurement shows some abnormalities that are representative for all emittance measurements in this campaign. The minima of both curves should be located symmetrically apart from the $K1$ zero position. This asymmetry suggests an astigmatism in the electron
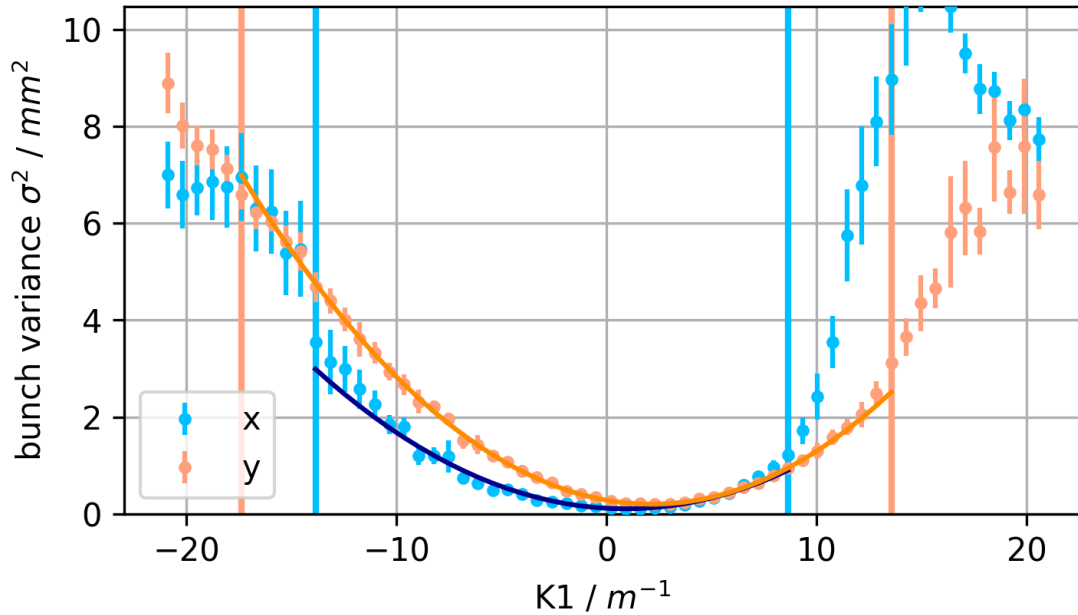
Figure 4.6.: Example for the emittance measurement. The bunch variance is plotted versus the applied, normalized quadrupole strength $K1$. A parabolic fit is performed for the data in between the vertical markers and the fit result is plotted. The RMS emittance can be calculated from the parabola curvature.

bunch. The beam size (and consequently the variance) increasingly deviates from the expected parabolic trace for increasing quadrupole fields, this requires a truncation of the data considered for the fitting routine, the limits are indicated by the vertical lines. The range of valid data is consistently lower in the horizontal axis and even lower for positive $K1$ values. This distortion might originate from the "horizontal, linear artifact" in the bunch, visible for example in fig. 4.4.

4.2.1. Individual working point characteristics

The bunch parameters for all considered working points are listed in tab. 4.2 as far as they could be measured. The notation for the bunch momentum includes the momentum range with the upper limit as superscript and the lower limit as subscript. The working points are discussed in the following paragraphs individually.

Working point Q_{max}: This working point was chosen for completeness and operates on the RF phase $-50°$ for maximum charge. The beam suffered from strong fluctuations in position and charge, neither an alignment nor the routine measurements are possible.

From simulation results shown in fig. 1.3, a bunch momentum of around $3\,\mathrm{MeV/c}$ is expected for this working point. The instability is a consequence of the low beam rigidity. This working point was not investigated further.

Table 4.2.: Measured bunch parameters for all working points. The values for bunch charge and emittance also contain the value uncertainty as one standard deviation. The notation for the bunch momentum includes the momentum range with the upper limit as superscript and the lower limit as subscript. For two working points, the momentum range could not be measured.

Working point	Charge (pC)	Momentum (MeV/c)	Bunch size (µm)	Emittance (nm rad)
Q/A_{max}	11.7 ± 1.0	$4.33^{+1.2\%}_{-1.8\%}$	$x : 87$	$x : 227 \pm 52$
			$y : 160$	$y : 310 \pm 63$
p_{max}	17.7 ± 0.6	4.37	$x : 182$	$x : 267 \pm 35$
			$y : 176$	$y : 324 \pm 46$
σ_{min}	4.0 ± 1.4	4.30	$x : 40$	$x : 74 \pm 12$
			$y : 100$	$y : 143 \pm 35$
$contrast$	9.3 ± 0.8	$4.32^{+0.7\%}_{-0.9\%}$	$x : 160$	$x : 236 \pm 112$
			$y : 167$	$y : 375 \pm 24$
$brightness$	171 ± 16	$4.36^{+1.1\%}_{-1.6\%}$	$x : 213$	$x : 981 \pm 296$
			$y : 377$	$y : 2061 \pm 357$

Working point $Q/A_\mathbf{max}$: The RF phase for this working point was found by a 2D scan: The quotient of measured charge and bunch area was tracked during a phase scan. A second, internal loop was employed to vary the solenoid field for different phase steps. This procedure is visualized with a screenshot of the FLUTE control system in fig. 4.7, over time (horizontal axis) the 2D scan of the RF phase (red) and solenoid current (blue) is tracked. The bunch charge is measured by the ICT and the beam size is calculated from the YAG screen image. The quotient Q/A is calculated live and plotted (purple), its peak value can be identified (ignoring the high, sharp out-layers). The corresponding RF phase [5] and solenoid current are marked with a cross-hair and labeled in the screenshot.

Two exemplary beam screen images from the forward YAG screen are shown in fig. 4.8. During the experiment, a 500 µm aperture (subfigure a) and a 200 µm aperture (subfigue b) were employed. By comparing both screen images, the SRR shadow of almost the full resonator body can be seen in subfigure a), and the shadow of the streaking gap can be identified in subfigure b). That subfigure b) really shows bunch charge going through the gap can be experimentally tested. By steering the bunch slightly to negative x-values, more charge is blocked by the resonator body. These images may offer a glimpse into the difficulties encountered during the alignment for small bunch sizes and charges.

This working point allows very stable operation and high beam quality. It was investigated a total of four times on four different days. The found ideal RF phase varied from day to day within $[-17°; -10°]$, a possible explanation for this might be coupled to the bunch charge but was not investigated further. This working point was stable enough for a

---

[5] Note, that the RF phase displayed here is the clystron set-value of the RF phase. This follows a different definition, in this thesis' definition the labeled value refers to $-16°$.
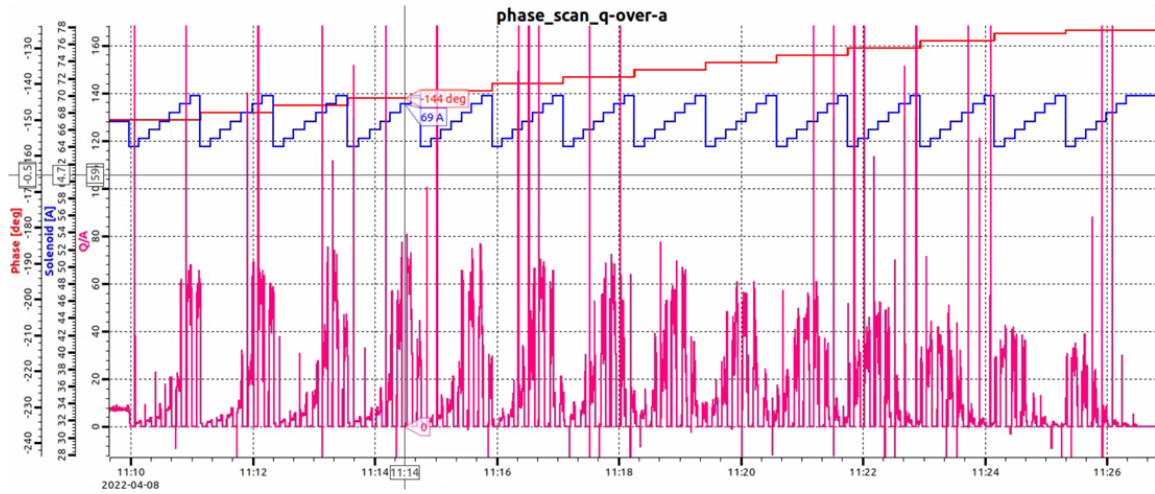
Figure 4.7.: Screenshot of the control system panel for the experimental search of the RF phase for the working point Q/A_{max}. The course of a 2D scan, RF phase (red) and solenoid current (blue) are plotted versus time (horizontal axis). The bunch size at the interaction point and the charge are recorded continuously and the parameter Q/A is computed and plotted (pink). The ideal constellation is identified at 11:14, the scan parameters at that time stamp are labeled: Rf phase = $-144°$, Solenoid current = 69 A.
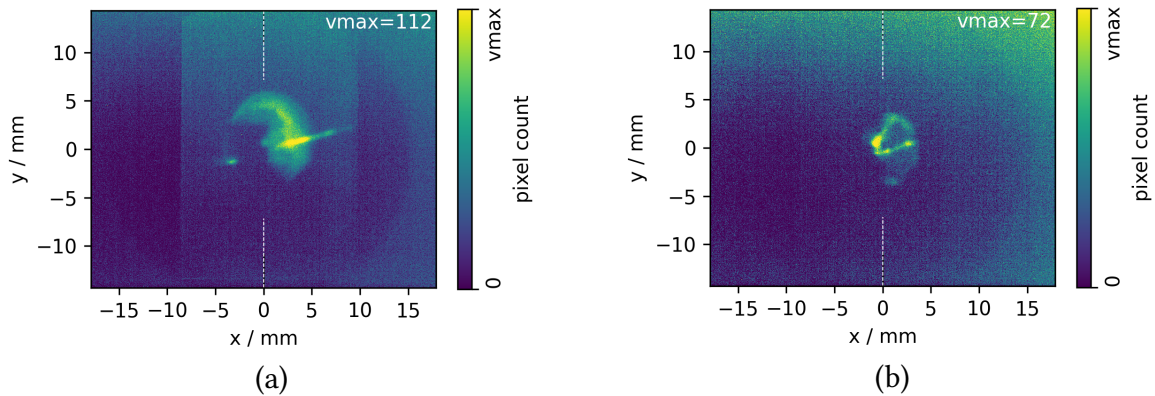
Figure 4.8.: Beam screen image from the forward YAG screen with the Q/A_{max} working point and a 500 μm aperture (a) and a 200 μm aperture (b) installed. Subfigure (a) shows a clear shadow of the SRR.

deeper investigation in an extensive RAP experiment, the details of which are discussed in the next section.

Working point p_{max}:   The working point for maximum bunch momentum also provided very good bunch quality and stability. The forward screen images show a smaller bunch size and should therefore even be more likely to reveal streaking beyond the bunch size, an example is given in fig. 4.9

As working points *contrast* and *brightness* can be considered as further developments of p_{max}, this working point was not additionally investigated in a RAP scan.
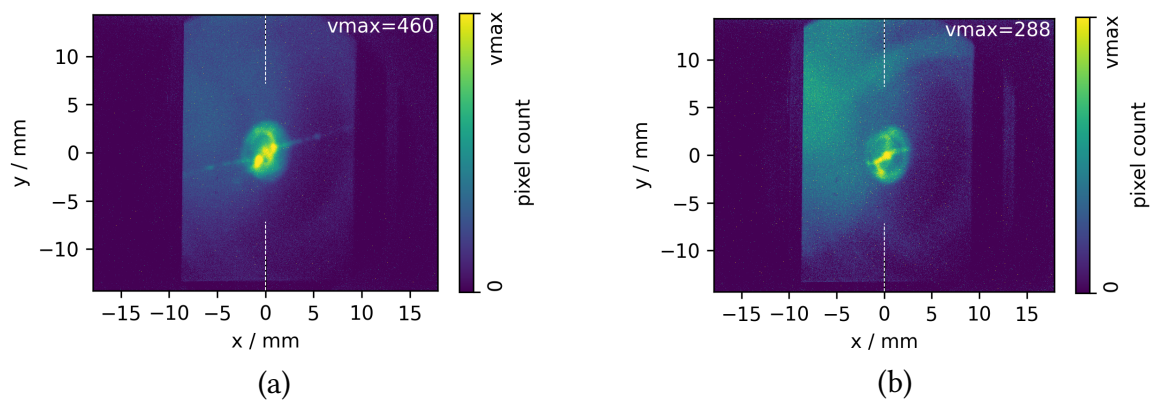
Figure 4.9.: Beam screen image from the forward YAG screen with the p_{max} working point and a 500 μm aperture (a) and a 200 μm aperture (b) installed.

Working point σ_{min} : The working point for minimum bunch size in the IP was evaluated with fixed laser power, the RF phase was found to be +21°, actually the bunch size should increase for positive RF phases, as shown in fig. 3.5, the results of the first simulation campaign. By changing the RF phase to positive values, the bunch charge dropped significantly to only 4 pC, compared to 17.7 pC, the charge measured at 0° with otherwise identical parameers, see working point p_{max}. Therefore the reduce in bunch charge is the reason for the small bunch size even tho the positive RF phase actually does not provide ideal conditions for a small bunch waist.

The jitter on the bunch charge is independent of the absolute charge as one can see from the charge measurement back in fig. 4.3. Therefore this working point is accompanied by significant fluctuations of the bunch charge of 1.4 pC. This is the highest charge uncertainty in relative terms across all working points, making this working point impossible for operation. During the attempt of measuring the momentum (spread), the instabilities become so large, that the investigations for this working point have been stopped.

Working point *contrast*: The working point contrast was investigated for the RF phase of zero degrees but with the lowest possible laser spot size. For machine protection reasons, the laser power was reduced to keep a comparable power density with respect to the other working points. The resulting low charge and the small laser spot size have been investigated by simulations to provide a high charge density at the interaction point. In fact the charge density at the interaction point is lower than the density reached with the Q/A_{max} working point.

Nonetheless this working point operates with very stable bunch parameters due to the high charge, it was investigated two times manually and two times with a RAP scan.

Working point *brightness*: For the *brightness* working point, the laser spot was enlarged as much as possible. With the larger spot, the laser power could be significantly increased without causing damage to the cathode. Both effects support the charge generation,
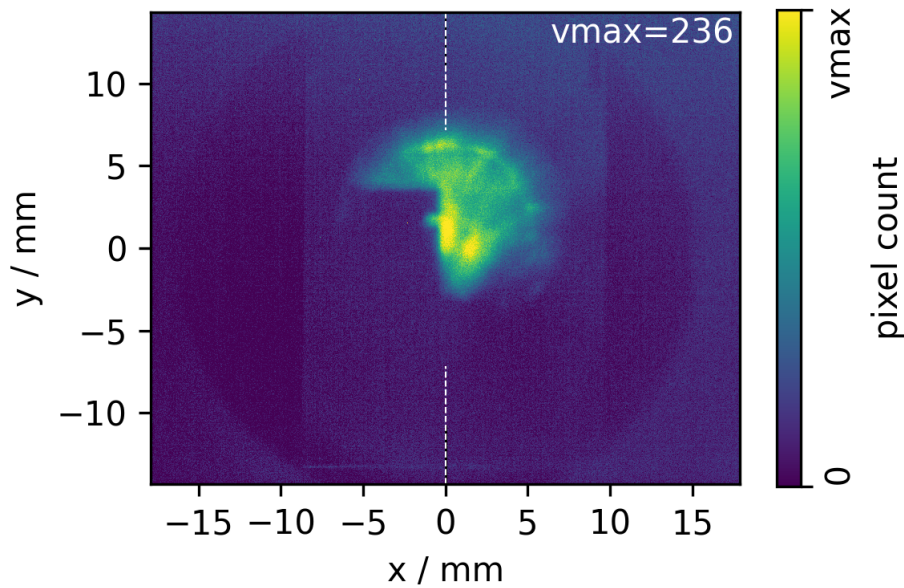
Figure 4.10.: Beam screen image from the forward YAG screen with the *brightness* working point and a 1500 μm aperture, the large beam size projects a clear shadow of the SRR on the YAG screen.

resulting in a massive bunch charge of around 170 pC. The working point was repeated several times, parameters like the charge differ greatly across the experimental days.

Because of the massive charge, this working point has the highest momentum spread and emittance across all working points. As predicted from the simulations, this setup provides good focusing conditions. The bunch size at the interaction point is only marginally larger compared to the contrast experiment with 210 μm instead of 160 μm for the horizontal bunch size. This provides a massively higher charge density in the bunch core and therefore also in the resonator gap, which was the motivation for this working point in the first place. In absolute terms, the 1σ bunch size is large enough, that the entire SRR body is visible in the shadow, as seen in fig. 4.10. With that, aligning the bunch (core) with the gap is a trivial task, rendering it a good candidate for a RAP scan.
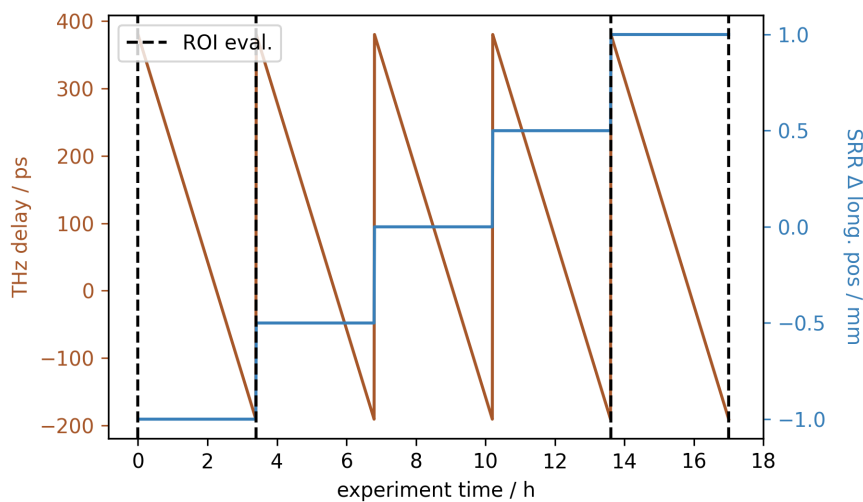
Figure 4.11.: The course of the two scanning axes versus time for a RAP scan. The THz delay appears to be changed continuously but actually has 1.3 ps steps. The bunch alignment is investigated at the four positions, marked with the black, dashed lines.

4.3. Experiments with the Raster Alignment Program

The discussed working points were examined manually for streaking effects. For this, the uncertain alignment parameters, the THz spatial and temporal alignment have been scanned individually. During this initial investigation, no streaking was observed. Therefore, additional RAP experiments were conducted for the three most stable working points $Q/A_{\max}$, *contrast* and *brightness*.

4.3.1. The RAP rhythm

The RAP varies the two alignment axes:

Axis 1: The THz arrival time is changed by moving the THz delay stage.

Axis 2: The IP z-position is changed via its motorized holder.

The progress of these two axes is illustrated in fig. 4.11. After the motors address a new scan position, an internal loop for the data acquisition is started. The process first captures a series of images without electron beam to construct a background image, followed by recording several screen images with beam. For the first data set the THz shutter is open and the streaking field is present. This data allows to build a background subtracted averaged image, called $\text{img}_{\text{avg}}^{\text{open}}$. Afterwards, the THz shutter is closed and a second data set, including also a second background image, is acquired for the corresponding averaged image, $\text{img}_{\text{avg}}^{\text{block}}$. Then the program proceeds to the next scan position.

Also during a RAP experiment the beam position is subject to the three types of machine instabilities: jitter, drift, and breakdowns. To compensate for machine jitter, only averaged images are considered in the data analysis with a high number of individual images (mostly

50 pieces) was chosen. To mitigate drifts in the beam position, the data for the background subtraction is updated for every averaged image.

In order to monitor drift instabilities, four "probe" images from strategic scan positions are investigated. These probe images are taken in the beginning and end of the first and last scans of axis 1, this is visualized in fig. 4.11 by the black, dashed lines. These probe images are evaluated to determine if a drift invalidated the beam alignment. An example set of probe images is shown in fig. 4.12, the marked squares reference on the different ROIs which are discussed in the following section.

The effects of breakdown events are challenging to come by because of their varying error patterns. Fortunately, the RF upgrade for FLUTE will provide a new klystron with higher stability. For future experiments, it can be expected that breakdowns will occur much less frequently.

4.3.2. Data processing

A ROI is a tool for excluding areas of the camera images that are not relevant e.g. image regions off the YAG screen. Using a ROI helps reducing the likelihood of artifacts or outliers influencing the analysis and also speeds up the analysis processing time.

The ROIs are developed and examined using the four probe images mentioned before, an example is given in fig. 4.12. Three different ROI types have been developed which can be seen in the image.

Golden: This ROI trims the camera view vertically by the golden ratio to 1/1.6[48] of the image size.[6] Horizontally the image is cut to the actual YAG screen width.

CoM: This ROI center equals the charge distribution's center of mass. The ROI horizontal and vertical size is proportional to the charge projections standard deviations.

Tight: A manually set ROI, very tight around the SRR gap shadow.

Quantification of difference images: The streaking signal can be detected by comparing the averaged images of a data pair with open and blocked THz pulse with each other, a simulated example is shown again in fig. 4.13, this image was already shown in the previous chapter as fig. 3.1. A RAP scan collects around 100 GB worth of screen images. To analyze these extensive data sets, a quantification of a streaking likelihood is required. An "empty" difference image where every pixel has a pixel count of zero, refers to completely identical averaged images, where definitely no streaking is visible. As positive and negative pixel counts are equally interesting for this analysis, the absolute value of the pixel counts in the difference image has to be considered.

[6] Later the ROI height was increased slightly to 1/1.5, the ROI name was not changed.
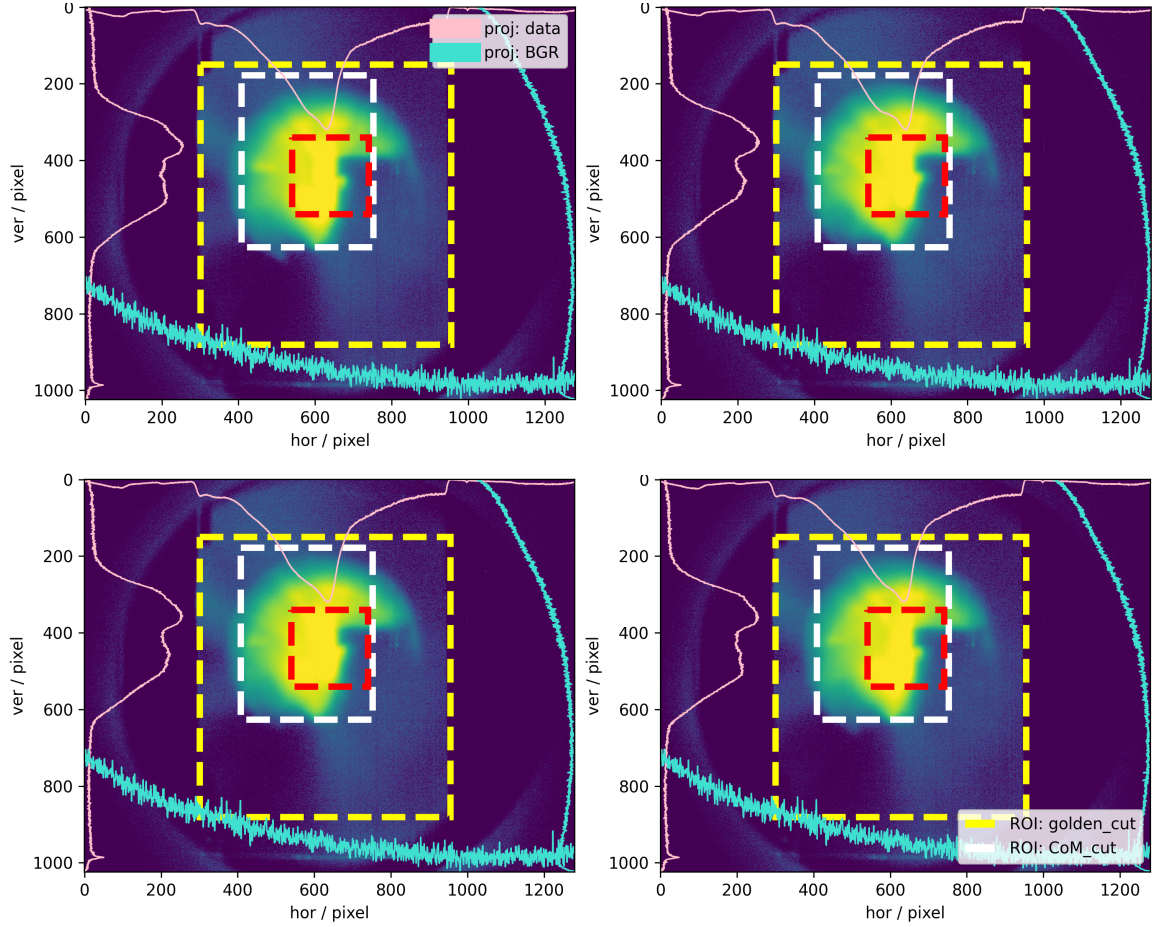
Figure 4.12.: Set of four probe images for investigation of machine stability during a contrast RAP experiment. The subfigures show the averaged forward beam screen image without background subtraction at different distinct positions during the RAP scan. The background and signal projection is shown by light blue and pink lines, the three different ROIs are shown by dashed rectangles. If the four images show no difference, the machine alignment did not change during the scan.

The so called distance of a difference image from an empty image can be mathematically expressed with several algorithms, e.g. the Manhattan distance, which is a standard tool in the discipline of image processing [49]. The Manhattan distance is calculated by the l_1-matrix norm of the image pixel matrix, which simply sums up the absolute pixel counts of the hole image.

In this analysis, the Normalized Integrated absolute Pixel Difference (NIPD) value is defined to quantify the streaking likelihood of visible streaking effects [50]. It is a slight modification of the Manhattan distance. Different ROIs are employed, therefore the l_1-norm is calculated only within the ROI $[m, n]$ sub matrix of the image and is normalized by $m \cdot n$, the number of pixels in the selected ROI.

$$\text{NIPD} = \sum_{i=1}^{m} \sum_{j=1}^{n} \frac{1}{m\,n} \left| \text{img}_{\text{avg}}^{\text{open}} - \text{img}_{\text{avg}}^{\text{block}} \right|_{i,j} \tag{4.1}$$
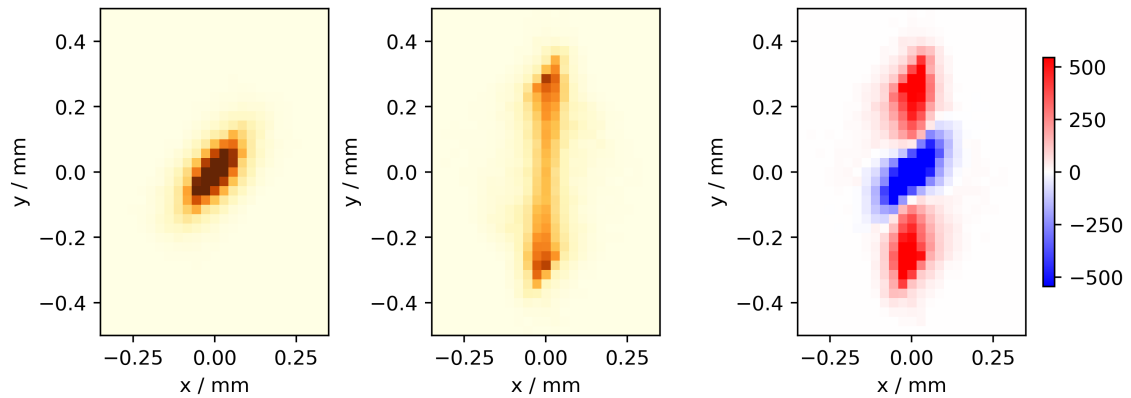
Figure 4.13.: Simulated forward screen image from ASTRA tracking simulation without (left) and with (center) an active streaking field in the TDS resonator. A difference image is calculated (right).

For a RAP experiment analysis, every scan position is quantified by a NIPD value. NIPD can take on values from within $[0; +\infty[$, where 0 corresponds to an empty difference image, and positive values indicate increasingly differing images.

The level of NIPD increase with a streaking signal can be estimated from simulations. The simulated example mentioned in the beginning of this chapter, presented in fig. 4.13 was used to calculate a NIPD value of 57 [51]. For this calculation, a tight ROI was used. The simulated ensemble of macro particles is transformed into a virtual beam screen image, meaning it is presented in the horizontal versus vertical spatial plane (x, y) and binned with the same granularity as the FLUTE beam screen images. The binning height is then adjusted to represent a realistic pixel intensity distribution. For the last step, the ratio of measured pixel intensity versus charge collected in the area seen by a camera pixel was referenced in a dedicated measurement at FLUTE.

4.3.3. Evaluation of a RAP scan

In the discussion of the experiment prerequisites, the scanning axes have been introduced, and the signal expectations have been formulated: Recalling from the experiment prerequisites, the streaking potential while changing the alignment axis: A scan of axis 1, the THz delay, provides streaking conditions only for four consecutive scan steps around the correct alignment, otherwise the synchronization of electrons and THz is off and the electrons cannot be streaked. Similarly, for a scan of axis 2, the THz spatial alignment, provides streaking conditions for 2-3 consecutive scan steps around the correct alignment. If both conditions are met, streaking is possible, a difference image should then show some charge relocation.

From the periodically scanning, the streaking signal has to appear in a clear pattern during the RAP scan. The streaking signal should increase the NIPD values in this exact pattern. In the example *contrast* experiment, the RAP scan covered 190 steps along scanning axis 1 (the delay stage) and repeated this procedure for five steps along axis 2 (the IP z-position).
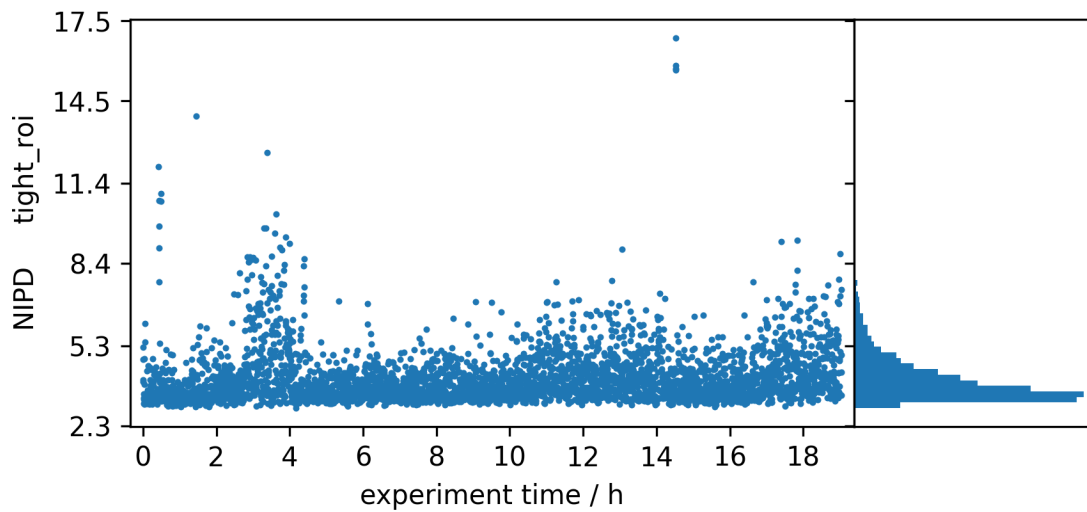
Figure 4.14.: NIPD values during a *contrast* RAP experiment with tight ROI, presented against the experiment time. A projection of all NIPD values is attached on the right.

The streaking conditions are fulfilled during four consecutive steps in axis 1 and for 2-3 neighboring steps in axis 2, while a single step in axis 2 takes roughly 4 hours. This means the streaking signal should build a group of four consecutive measurement points with increased NIPD values. In total 2-3 of these groups, separated by four hours can be expected.

Results of the *contrast* scan: The NIPD values during this scan are displayed in fig. 4.14 for the *contrast* RAP experiment, evaluated with the tight ROI. The evaluations for the other two ROIs show very similarly shaped results. The analysis for all three ROIs is presented side by side in Appendix A.5. The right hand side shows the projection of all NIPD values during the scan. The projection shows an asymmetrically folded normal distribution for the jitter-affected NIPD values. With this representation, the streaking signal can be searched in the scan data by three different approaches.

1. In absolute numbers, this RAP scan addressed $190 \cdot 5 = 950$ positions. From the 950 recorded image pairs, only 8-12 pairs which is roughly 1 % of the collected data, have a chance of showing a streaking signal. The histogram could reveal the signal as an elevation above a smooth background distribution. This elevation should be located at high NIPD values and contain up to 1 % of the total histogram volume.

2. The streaking signal should reveal itself in the scatter plot through elevated NIPD values, following the previously discussed pattern: 2-3 groups separated by 4-hour intervals, with each group consisting of four consecutive data points, each with increased NIPD values.

3. As a final attempt, the difference images with the highest NIPD values were individually observed by hand. Two examples of difference images are shown in fig. 4.15,
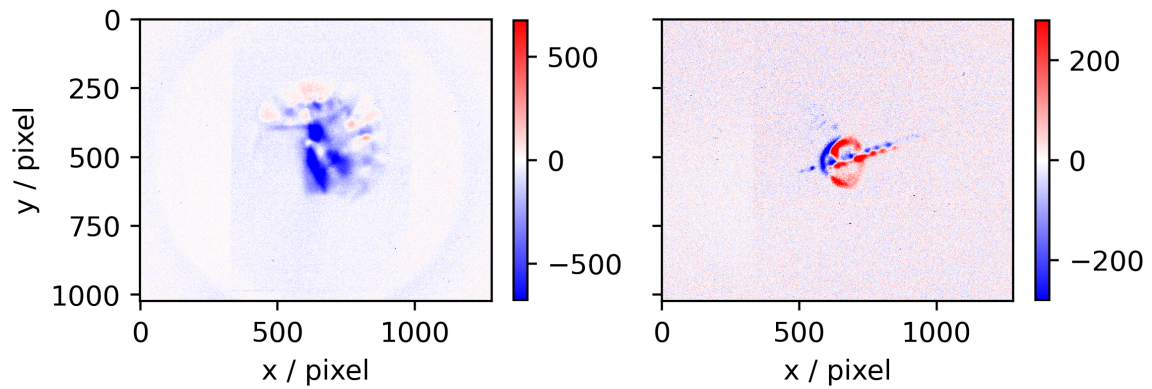
Figure 4.15.: Example of difference images showing typical outlayers with relative high difference intensities. The two images originate from a *brightness* (left) and a *contrast* (right) RAP scan.

the left image originates from a *brightness* and the right from a *contrast* RAP scan. These examples are typical results of outliers with exceptional high NIPD values. In the left difference image, the intensity distribution indicates horizontal movement of particles. The right image displays a chaotic reordering of the charge within the bunch footprint. Both distributions are not oriented vertically, as one might expect from streaking.

In total, 10 different RAP scans were conducted across three different working points. Approximately 1 TB worth of averaged screen image pairs were analyzed using the three just discussed approaches to evaluate their NIPD values. Unfortunately, no visible streaking signal was observed.

Nevertheless, several partial successes for example a clear understanding of the experimental challenges was achieved. Several improvements can be implemented for future TDS experiments, these considerations are presented in the following chapter.

5. Design of an optimized TDS experiment

Several approaches have been conceived to make the streaking signal more easily detectable. To enhance the visibility of the streaking signal, it should clearly stand out from the background. This requires an optimized vertical streaking kick p_y, recalling from equ. 2.38, the kick strength is proportional to the streaking field, resonating in the gap, integrated along the electron path through the field:

$$p_y \propto \int \hat{E}_{\text{strk}}(z)\mathrm{d}z \tag{5.1}$$

According to equ. 2.31, the streaking field amplitude is given by

$$\hat{E}_{\text{strk}} = \hat{E}_{\text{THz}}\, X\,. \tag{5.2}$$

The enhancement factor X as well as the streaking field extent in z-direction are defined by the resonator geometry. The geometry can be further optimized, as discussed in section 5.1. The factor $\hat{E}_{\text{THz}}$ is the electric field strength of the THz pulse front. Increasing the THz pulse energy is one of several possibilities of optimizing the experimental setup, as outlined in section 5.2. If the streaking is still not visible, an optimized data analysis can be developed, ideas in this regard are discussed in section 5.3.

5.1. Resonator Optimization

Recall the dimensions of the TDS resonator from tab. 1.1 used in the experiment, its thickness is $d = 80\,\mu\text{m}$ and the radius of the circular cutout is $U = 153\,\mu\text{m}$. First simulation studies by S. Glukhov have been presented in section 2.1.3. According to these findings, the circular cutout of the resonator can be adapted so that the SRR resonance frequency matches the peak frequency of our THz pulse at 258 GHz[1]. This adaptation should increase the resonator enhancement factor X. According to fig. 2.14, the cutout diameter has to be reduced to $U = 70\,\mu\text{m}$, which is less than half of the initial value. However, the study was performed for resonators with a thickness of $U = 20\,\mu\text{m}$, the actual value is subject to future, adapted simulation.

The resonator thickness can be increased until the electron experiences a streaking field phase advance of 90°. According to equ. 2.32, the optimized thickness is $d = 360\,\mu\text{m}$, which

---

[1] Note, that this value is calculated indirectly, first a precise measurement of the THz spectrum is required.
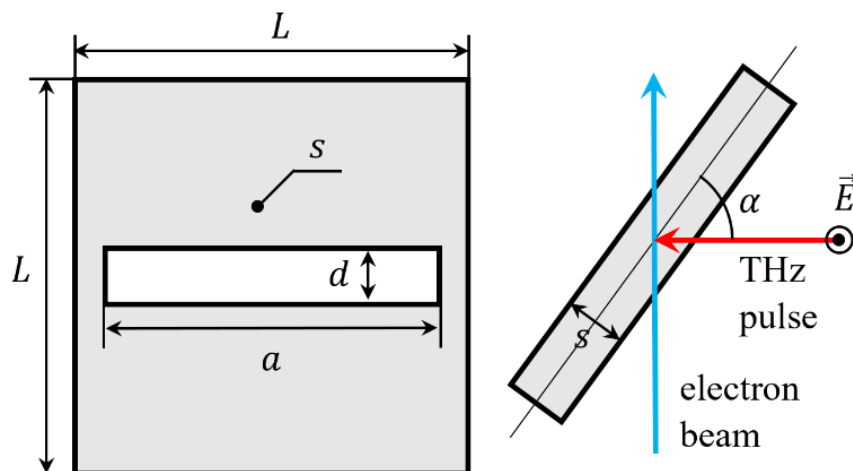
Figure 5.1.: TDS Slit-Resonator design. This figure was kindly provided by S. Glukhov.

is 4.5 times the current value. Recalling equ. 5.1, this leads to a higher vertical streaking kick by integrating longer over $\hat{E}_{\mathrm{strk}}$.

Due to complex cross-correlations, the optimization of the thickness d and the diameter U has to be found in a conjunct simulation. The actual optimized values might differ from the 1D optimization results, presented in the cited study.

Slit-Resonator Design: An alternative resonator design has been discussed in the collaboration, first resonator specimens have been realized and will soon be tested in the updated FLUTE accelerator. The geometry is shown in fig. 5.1, the performance in terms of the streaking amplitude is marginally lower than that of the SRR design [36]. However, the design has a built-in aperture and automatically blocks all charge that misses the gap. This way, alignment challenges can be avoided almost entirely.

5.2. Experimental Setup Optimization

The experimental setup offers several optimization opportunities beyond the resonator itself. Particularly noteworthy is the major upgrade of FLUTE's hardware, the klystron, the RF-photoinjector and the solenoid are replaced by factory new components. The upgrade of the RF system is expected to yield much less breakdown events, mitigating the most invasive machine instability [52]. From the new photoinjector, an overall reduction in bunch emittance and dark current is expected. The latter is particularly important for operating with lower bunch charges. However the concrete possibilities arising from these upgrades will be clarified post-commissioning. Even further potential enhancements in the experimental setup can be achieved in the near future.
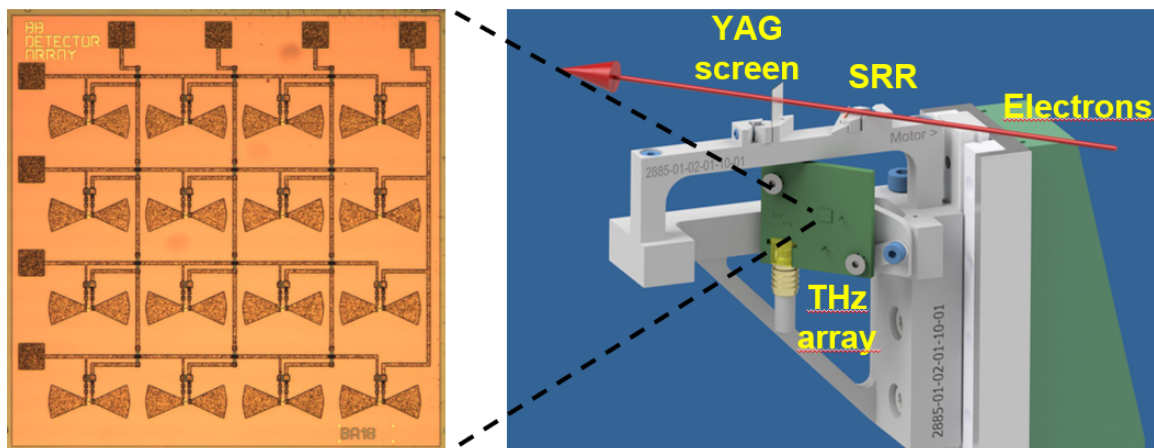
Figure 5.2.: Microscope image of the THz antenna array (left) and the mount holding also the YAG screen and the TDS resonator (right). The microscope image is taken by Dr. N. Neumann (TU Dresden), the CAD drawing is provided by T. Borkowski (IBPT), adapted by M. Nabinger (IBPT).

Increasing the THz pulse energy: By increasing the THz pulse energy, the electric field front $\hat{E}_{\text{THz}}$ increases. The presented THz setup can be adapted with relatively low effort by the following three items:

1. THz optics made from the material UHMWPE absorb much lower THz power compared to conventional optics which have been in use so far [2]. A set of new lenses made from UHMWPE was tested in a mock-up setup and will be installed for the upcoming TDS experiments in the actual FLUTE setup.

2. Enclosing and dehumidifying the TPFM setup allows for the control of ambient conditions, including air pressure, movements and moisture. This further reduces energy absorption for the THz pulse before it reaches the TDS vacuum chamber. This, along with the tests of the UHMWPE optics, has been discussed in [34] by M. Nabinger, estimating a pulse energy increase to 188 ± 40 % compared to the current setup.

3. The Lithium Niobate crystal in the TPFM is the core element for creating the THz pulse. By cooling this crystal, the conversion efficiency from the Infrared (IR) pump pulse to the THz pulse energy can be increased to 250 %, according to [53]. However, this process alters the THz pulse spectrum which may lead to a different, ideal resonator design.

Improvements to the THz alignment prerequisites: One major challenge during the experiment was ensuring the fragile beam and THz alignment with the IP. Since the THz pulse could only be aligned outside the TDS chamber, an uncertainty remained regarding the pulse position. This necessitated to scan the resonator in the z-position as one of the RAP scan axes.

---

[2] The THz optics installed so far are made from a material called ZEONEX by TYDEX.

It is foreseen to add a THz antenna array to the TDS chamber setup to validate the pulse position. The antenna will be mounted together with the resonator and the YAG screen on the XYZ motorized stage in the center of the chamber, as shown in fig. 5.2. This arrangement allows to move the antenna array directly to the IP, verifying the THz pulse position within the experiment. This improvement completely eliminates the need for one scanning axis, speeding up the experiment and thus, reducing its susceptibility to drift instabilities.

The second scanning axis is the THz temporal synchronization with the electron bunch. The measurement of the synchronization pre-alignment as described in [29] should be repeated right before the next TDS experiment. This enables a reduction in the required scanning range of the delay stage.

Reducing Machine Instabilities: The other major challenge lies in the instability of the bunch position. The just discussed improvements to the experimental prerequisites allow for a much shorter compacted RAP (cRAP) scan, which is inherently less affected by drift effects. The RF upgrade is expected to mitigate the breakdown events.

To identify the machine parameter with the most significant impact on the bunch jitter, a simulation campaign may be initiated. For this purpose, a dataset was collected, monitoring the stability of machine parameters include the laser spot position, size and intensity, details around the RF system and auxiliary information like multiple temperature and vacuum levels. In simulations, the influence of instabilities of single isolated machine parameter can be investigated. The simulation results will identify the driving forces of the beam instability, allowing to develop a strategy to fight the bunch jitter.

Beam dynamics: Retrospective, the working point $Q/A_{\max}$ appears to be the most promising working points, due to its overall good beam quality and low instabilities. This is also reflected the low bunch emittance and beam size[3]. Further, it appears, that the bunch charge is the most important parameter to tune. Lower charges should be addressable with the new FLUTE components due to a reduce in dark current.

The quadrupole has not been utilized so far but may be a valuable keystone for a new modus operandi. The magnet is located briefly before the TDS chamber, where the bunch is still converging. Applying a strong quadrupole gradient can reduce the bunch vertical convergence, this eventually leads to a lower vertical divergence of the electron beam behind the focus plane. This will benefit the ratio of the vertical momenta between streaked against unstreaked electrons.

---

[3]   The working point $\sigma_{\min}$ yielded even lower values in emittance and beam size due to the bunch charge being less than half the value compared to the working point $Q/A_{\max}$.

5.3. Data Analysis Optimization

A final improvement can be implemented in the data analysis of the difference images. The analysis used in this thesis quantifies the difference between two beam screen images without and with THz shine onto the TDS resonator, using the Manhattan distance. There are several ways to make this investigation more sensitive to the pattern of a streaking signal, two of which follow are:

Since streaking redistributes electrons vertically, the Manhattan distance can be combined with a weighting matrix. This way, a vertical charge redistribution contributes stronger to the NIPD value.

A more complex but also more promising approach would be to implement an anomaly detection, based on a neural network. One image of each data pair definitely shows no streaking signal. Such a data set is well-suited for training of a neural network. One could even further train this network with the expected pattern of streaking signals from simulated data.

Throughout the work of this thesis, the experimental challenges have been identified and partially already addressed. Plans for further tackling all the remaining hurdles have been formulated and discussed. Some of these plans can be implemented in short term and first experimental tests with an improved setup are scheduled to be conducted in spring 2024. A discussion of the upgrades and the experimental outcomes are planned to be presented at the upcoming IPAC conference [54].

Summary

This work studies the feasibility of the Transverse Deflecting Structure experiment at FLUTE, the commissioning of a novel electron bunch length measurement setup. The THz-powered resonator and explicitly the induced, resonating streaking field are discussed in detail. Notably, the characteristics of the streaking field depend on the properties of the incoming THz pulse, particularly its energy and spectrum. Both aspects are investigated in our setup, and their measurement results were incorporated into the analysis. This allowed for precise predictions of the TDS performance in our setup, such as a streaking amplitude of ±345 µm, and the resolution of the bunch length measurement in our specific setup of 69 fs. This resolution of an early stage test experiment promises to clearly outperforms optimized state-of-the-art RF-based streaking setups by around an order of magnitude.

For the feasibility study, a holistic understanding of the accelerator and laser setup was gathered. Comprehensive bean dynamic simulations were conducted, covering multiple different settings in the RF system, magnetic components and the charge generating laser parameters. With these studies two strategies have been elaborated: maximizing the absolute and the relative charge focused in the streaking gap. These optimizations resulted in two working points, which, along with four others, were experimentally tested with the goal of generating a streaking signal.

The considerable experimental challenges were encountered and systematically addressed in this work. Due to the high precision requirements in the micro-meter level, the experiment was exceptionally sensitive to otherwise negligible fluctuations or inaccuracies in the experimental setup. Countermeasures were developed, including precise beam-based alignment of the electron bunch with the RF-photoinjector, the solenoid, the geometrical axis of the beam pipe and of course the streaking field. Ensuring the precise spatial and temporal co-arrival of electrons and THz pulses at the resonator interaction point was a critical challenge. The TDS resonator is placed in an evacuated experimental chamber, directly integrated into the accelerator. During the experiment, the vacuum seal of the TDS chamber must not be broken and the THz alignment with the interaction point cannot be verified directly. To overcome remaining uncertainties about the THz horizontal position and its arrival time, the RAP scan was developed and successfully tested. The deployed scan routine acquired automatically pairs of beam screen images in which only one image shows a bunch which was exposed to the streaking field. A streaking signal would be visible within their difference image, therefore an analysis tool was developed.

The results presented in this thesis form a solid foundation for the continuing commissioning of the TDS experiment at FLUTE. With the understanding of the potential appearance of the streaking signal, as well as tackling alignment and synchronization challenges,

important milestones for this project have been achieved during this work. The strategies discussed for further experiment enhancements lay the groundwork for successful streaking as the next consequent step towards the long-term goal of transforming the TDS experiment into a regularly applied routine measurement tool for any future short-pulse facility.

Bibliography

[1]   Erik Brundermann, Heinz-Wilhelm Hubers, and Maurice Kimmitt. *Terahertz Techniques*. en. 2012th ed. SPringer series in optical sciences. Berlin, Germany: Springer, Apr. 2012.

[2]   Dayne F. Swearer et al. "Monitoring Chemical Reactions with Terahertz Rotational Spectroscopy". In: *ACS Photonics* 5.8 (2018), pp. 3097–3106. DOI: 10.1021/acsphotonics.8b00342. eprint: https://doi.org/10.1021/acsphotonics.8b00342. URL: https://doi.org/10.1021/acsphotonics.8b00342.

[3]   P. J. Emma. *Bunch Length Measurements Using a Transverse RF Deflecting Structure in the SLAC Linac*. Technical Report, DE2002-799088; SLAC-PUB-9241. May 2002.

[4]   Filippos Toufexis and Valery Dolgashev. "Sub-Picosecond X-Ray Streak Camera using High-Gradient RF Cavities". In: *10th International Particle Accelerator Conference*. 2019, THPTS064. DOI: 10.18429/JACoW-IPAC2019-THPTS064.

[5]   Sonja Jaster-Merz et al. "First Studies of 5D Phase-Space Tomography of Electron Beams at ARES". In: *JACoW* LINAC2022 (2022), MOPORI10. DOI: 10.18429/JACoW-LINAC2022-MOPORI10.

[6]   Justyna Fabiańska, Günther Kassier, and Thomas Feurer. "Split ring resonator based THz-driven electron streak camera featuring femtosecond resolution". In: *Scientific Reports* 4.1 (July 2014). ISSN: 2045-2322. DOI: 10.1038/srep05645. URL: http://dx.doi.org/10.1038/srep05645.

[7]   X. L. Shen et al. "A THz driven split-ring resonator based ultrafast relativistic electron streak camera". In: *AIP Advances* 9.8 (Aug. 2019), p. 085209. ISSN: 2158-3226. DOI: 10.1063/1.5080374. eprint: https://pubs.aip.org/aip/adv/article-pdf/doi/10.1063/1.5080374/12909727/085209_1_online.pdf. URL: https://doi.org/10.1063/1.5080374.

[8]   X.Y. Liu. "Design of BPM System for FEL Facility at NSRL and Research on THz-driven Streak Camera". Dr. Hefei, China, Oct. 2021.

[9]   Oliver Finlay. "Electron Beam Manipulation in Terahertz Frequency Radiation-Driven Structures". English. PhD thesis. Lancaster University, 2022. DOI: 10.17635/lancaster/thesis/1753.

[10] M. J. Nasse et al. "FLUTE: A versatile linac-based THz source generating ultra-short pulses". In: *IPAC 2013: Proceedings of the 4th International Particle Accelerator Conference*. 55.51.20; LK 02. Asian Committee for Future Accelerators, 2013, pp. 2147–2149. ISBN: 978-3-9545012-2-9.

[11]   A. Einstein. "Über einen die Erzeugung und Verwandlung des Lichtes betreffenden heuristischen Gesichtspunkt". In: *Annalen der Physik* 322.6 (1905), pp. 132–148. DOI: `https://doi.org/10.1002/andp.19053220607`. eprint: `https://onlinelibrary.wiley.com/doi/pdf/10.1002/andp.19053220607`. URL: `https://onlinelibrary.wiley.com/doi/abs/10.1002/andp.19053220607`.

[12]   R Bossart et al. "A 3 GHz photoelectron gun for high beam intensity". In: *Nuclear Instruments and Methods in Physics Research Section A: Accelerators, Spectrometers, Detectors and Associated Equipment* 375.1 (1996). Proceedings of the 17th International Free Electron Laser Conference, ABS7–ABS8. ISSN: 0168-9002. DOI: `https://doi.org/10.1016/0168-9002(95)01369-5`. URL: `https://www.sciencedirect.com/science/article/pii/0168900295013695`.

[13]   Zikri M. Yusof, Manoel E. Conde, and Wei Gai. "Schottky-Enabled Photoemission in a rf Accelerator Photoinjector: Possible Generation of Ultralow Transverse Thermal-Emittance Electron Beam". In: *Phys. Rev. Lett.* 93 (11 Sept. 2004), p. 114801. DOI: `10.1103/PhysRevLett.93.114801`. URL: `https://link.aps.org/doi/10.1103/PhysRevLett.93.114801`.

[14]   David J. Griffiths. *Introduction to Electrodynamics -*. Cambridge: Cambridge University Press, 2017. ISBN: 978-1-108-42041-9.

[15]   Eva Panofski et al. "Commissioning Results and Electron Beam Characterization with the S-Band Photoinjector at SINBAD-ARES". In: *Instruments* 5 (Aug. 2021). DOI: `10.3390/instruments5030028`.

[16]   Thiemo Schmelzer et al. "Systematic Beam Parameter Studies at the Injector Section of FLUTE". In: *12th International Particle Accelerator Conference : virtual edition, May 24th-28th, 2021, Brazil : proceedings volume / IPAC2021. Ed.: R. Picoreti.* 12th International Particle Accelerator Conference. IPAC 2021 (Online, May 24–28, 2021). 54.11.11; LK 01. JACoW Publishing, 2021, pp. 2837–2839. ISBN: 978-3-95450-214-1. DOI: `10.18429/JACoW-IPAC2021-WEPAB103`.

[17]   Vinit Kumar. "Understanding the focusing of charged particle beams in a solenoid magnetic field". In: *American Journal of Physics* 77.8 (Aug. 2009), pp. 737–741. ISSN: 0002-9505. DOI: `10.1119/1.3129242`. eprint: `https://pubs.aip.org/aapt/ajp/article-pdf/77/8/737/13068856/737\_1\_online.pdf`. URL: `https://doi.org/10.1119/1.3129242`.

[18]   Klaus Wille. *The physics of particle accelerators : an introduction; Repr.* Includes bibliographical references and index; English. Oxford [u.a.]: Oxford Univ. Press, 2009, XIII, 315 S : Ill., graph. Darst. ISBN: 0-19-850550-7. URL: `https://reserves.ub.rwth-aachen.de/record/131066`.

[19]   T. Schmelzer et al. "Detailed Analysis of Transverse Emittance of the FLUTE Electron Bunch". In: *13th International Particle Accelerator Conference : June 12-17, 2022, Impact Forum, Muangthong Thani, Bangkok, Thailand : conference proceedings. Ed.: T. Chanwattana.* 13th International Particle Accelerator Conference. IPAC 2022 (Bangkok, Thailand, June 12–17, 2022). International Particle Accelerator Conference.

54.11.11; LK 01. JACoW Publishing, 2022, pp. 2289–2291. ISBN: 978-3-9545022-7-1. DOI: 10.18429/JACoW-IPAC2022-WEPOMS022.

[20] U. Iriso, G. Benedetti, and Francis Perez. "Experience with YAG and OTR screens at ALBA". In: *DIPAC 2009 - 9th European Workshop on Beam Diagnostics and Instrumentation for Particle Accelerators* (Jan. 2009).

[21] R. Nishi et al. "Electron energy dependence of characteristics of fluorescent plates for ultrahigh-voltage electron microscopes". In: *Ultramicroscopy* 62.4 (1996), pp. 271–275. ISSN: 0304-3991. DOI: https://doi.org/10.1016/0304-3991(96)00004-6. URL: https://www.sciencedirect.com/science/article/pii/0304399196000046.

[22] Roman Spesyvtsev. "Transverse beam size measurement systems at photo injector test facility in Zeuthen". Other thesis. 2007.

[23] Renuka Krishnakumar. "Scintillation screen materials for beam profile measurements of high energy ion beams". en. PhD thesis. Darmstadt: Technische Universität Darmstadt, 2016. URL: http://tuprints.ulb.tu-darmstadt.de/5504/.

[24] A H Lumpkin et al. "Spatial resolution limits of YAG:CE powder beam-profile monitors at the Fermilab A0 photoinjector". In: (Oct. 2009). URL: https://www.osti.gov/biblio/967400.

[25] Thiemo Schmelzer. *Discussion about bluring out of a YAG screen.* Private communication. 2023.

[26] Theodor Scheimpflug. "Festschrift zum 150 Jährigen Bestand des staatlichen Vermessungswesens in Österreich." In: *Blätter für Technikgeschichte.* Berlin Heidelberg New York: Springer-Verlag, 2019, pp. 169–277. ISBN: 978-3-709-15528-8.

[27] Advatech UK Limited. *YAG(Ce) - Yttrium Aluminium garnate (Cesium) Scintillator Crystal.* Accessed on August 10, 2023. 2023. URL: https://www.advatech-uk.co.uk/yag_ce.html.

[28] Matthias Nabinger. "Aufbau der Laseroptik und Charakterisierung lasergenerierter THz-Strahlung für das Split-Ring-Resonator Experiment bei FLUTE". German. 54.11.11; LK 01. MA thesis. Karlsruher Institut für Technologie (KIT), 2021. 112 pp. DOI: 10.5445/IR/1000150152.

[29] M. Nabinger et al. "Efficient Terahertz Generation by Tilted-Pulse-Front Pumping in Lithium Niobate for the Split-Ring Resonator Experiment at FLUTE". In: *Proc. IPAC'21* (Campinas, SP, Brazil). International Particle Accelerator Conference 12. https://doi.org/10.18429/JACoW-IPAC2021-THPAB251. JACoW Publishing, Geneva, Switzerland, Aug. 2021, THPAB251, pp. 4299–4302. ISBN: 978-3-95450-214-1. DOI: 10.18429/JACoW-IPAC2021-THPAB251. URL: https://jacow.org/ipac2021/papers/thpab251.pdf.

[30] A Ferrari et al. *FLUKA: A multi-particle transport code (program version 2005).* CERN Yellow Reports: Monographs. Geneva: CERN, 2005. DOI: 10.5170/CERN-2005-010. URL: https://cds.cern.ch/record/898301.

[31] Yifang Song et al. "Analytical model of the streaking process in a single split-ring resonator for sub-ps electron pulse". In: *Nuclear Instruments and Methods in Physics Research Section A: Accelerators, Spectrometers, Detectors and Associated Equipment* 987 (2021), p. 164861. ISSN: 0168-9002. DOI: `https://doi.org/10.1016/j.nima.2020.164861`. URL: `https://www.sciencedirect.com/science/article/pii/S0168900220312584`.

[32] *CST Studio Suite*. Version 2022. URL: `https://www.cst.com/`.

[33] D. F. Swinehart. "The Beer-Lambert Law". In: *Journal of Chemical Education* 39.7 (1962), p. 333. DOI: `10.1021/ed039p333`. eprint: `https://doi.org/10.1021/ed039p333`. URL: `https://doi.org/10.1021/ed039p333`.

[34] M. Nabinger et al. "Characterization and optimization of laser-generated THz beam for THz based streaking". English. In: *Proc. IPAC'23* (Venice, Italy). IPAC'23 - 14th International Particle Accelerator Conference 14. JACoW Publishing, Geneva, Switzerland, May 2023, pp. 4149–4152. ISBN: 978-3-95450-231-8. DOI: `10.18429/JACoW-IPAC2023-THPA079`. URL: `https://indico.jacow.org/event/41/contributions/2646`.

[35] Steven W. Smith. *The Scientist and Engineer's Guide to Digital Signal Processing*. USA: California Technical Publishing, 1997. ISBN: 0966017633.

[36] Sergei Glukhov et al. "Simulations of the compact transverse-deflecting system for ultra-short electron bunch diagnostic". In: *14th International Particle Accelerator Conference, Venedig, 7th-12th May 2023*. 14th International Particle Accelerator Conference. IPAC 2023 (Venedig, Italien, May 7–12, 2023). 54.11.11; LK 01. JACoW Publishing, 2023, pp. 4887–4890. ISBN: 978-3-95450-231-8. DOI: `10.18429/JACoW-IPAC2023-THPL192`.

[37] Claudia Brückner et al. "Design and evaluation of a THz time domain imaging system using standard optical design software". In: *Applied Optics* 47.27 (Sept. 2008), p. 4994. DOI: `10.1364/ao.47.004994`. URL: `https://doi.org/10.1364/ao.47.004994`.

[38] K. Flöttmann. *ASTRA: A Space Charge Tracking Algorithm*. Version 2021. URL: `%5Curl%7Bhttp://www.desy.de/~mpyflo%7D`.

[39] Encyclopedia of Mathematics. *Runge-Kutta method", EMS Press, 2001 [1994]*. URL: `http://encyclopediaofmath.org/index.php?title=Runge-Kutta_method&oldid=52628` (visited on 12/01/2023).

[40] Jens Schäfer et al. "Split Ring Resonator Experiment - Simulation Results". In: *12th International Particle Accelerator Conference : virtual edition, May 24th-28th, 2021, Brazil : proceedings volume / IPAC2021. Ed.: R. Picoreti*. 12th International Particle Accelerator Conference. IPAC 2021 (Online, May 24–28, 2021). 54.11.11; LK 01. JACoW Publishing, 2021, pp. 888–891. ISBN: 978-3-95450-214-1. DOI: `10.18429/JACoW-IPAC2021-MOPAB280`.

[41] S. Jalas et al. "Tuning curves for a laser-plasma accelerator". In: *Phys. Rev. Accel. Beams* 26 (7 July 2023), p. 071302.

[42] C. Xu et al. "Surrogate Modelling of the FLUTE Low-Energy Section". In: *Proc. IPAC'22* (Bangkok, Thailand). International Particle Accelerator Conference 13. JACoW Publishing, Geneva, Switzerland, July 2022, TUPOPT070, pp. 1182–1185. ISBN: 978-3-95450-227-1. DOI: 10.18429/JACoW-IPAC2022-TUPOPT070. URL: https://jacow.org/ipac2022/papers/tupopt070.pdf.

[43] A Adelmann et al. "The Object Oriented Parallel Accelerator Library (OPAL), Design, Implementation and Application". In: (Jan. 2009).

[44] K Flöttmann. *Note on the thermal emittance of electrons emitted by cesium telluride photo cathodes. The thermal emittance of electrons emitted by cesium telluride photo cathodes.* Tech. rep. Hamburg: DESY, 1997. URL: https://cds.cern.ch/record/331841.

[45] M. Hänel and DESY. "Experimental investigations on the influence of the photocathode laser pulse parameters om the electron bunch quality in an RF Photoelectron source". Universität Hamburg, Diss., 2010. Dr. Universität Hamburg, 2010. DOI: 10.3204/DESY-THESIS-2010-027. URL: https://bib-pubdb1.desy.de/record/89109.

[46] Jens Schäfer et al. *Laser alignment of internal components of the linear accelerator FLUTE.* Vortrag gehalten auf DPG-Frühjahrstagung : Physik der Hadronen und Kerne (HK), Plasmaphysik (P), Arbeitskreis Beschleunigerphysik (AKBP) (2022), Online, 28. März–1. April 2022. 54.11.11; LK 01. 2022.

[47] Helmut Wiedemann. *Particle Accelerator Physics I.* Springer Berlin Heidelberg, 1999. ISBN: 9783662038277. DOI: 10.1007/978-3-662-03827-7. URL: http://dx.doi.org/10.1007/978-3-662-03827-7.

[48] M. Ohm. *Die reine Elementar-Mathematik: zum Gebrauche an höheren technischen Lehr-Anstalten, besonders aber an Gymnasien und zum Selbst-Unterrichte.* Die reine elementar-mathematik: zum gebrauche an höhern technischen lehranstalten, besonders aber an gymnasien und zum selbst-unterrichte. Jonas, 1834. URL: https://books.google.de/books?id=iks2xwEACAAJ.

[49] Xin-She Yang. "6 - Data mining techniques". In: *Introduction to Algorithms for Data Mining and Machine Learning.* Ed. by Xin-She Yang. Academic Press, 2019, pp. 109–128. ISBN: 978-0-12-817216-2. DOI: https://doi.org/10.1016/B978-0-12-817216-2.00013-2. URL: https://www.sciencedirect.com/science/article/pii/B9780128172162000132.

[50] Jens Schäfer et al. *Split-ring resonator experiments and data analysis at FLUTE.* Vortrag gehalten auf 86th Jahrestagung der DPG und DPG-Frühjahrstagung der Sektion Materie und Kosmos - Arbeitskreis Beschleunigerphysik (SMuK 2023), Dresden, Deutschland, 20.–24. März 2023. 54.11.11; LK 01. 2023.

[51] Jens Schaefer et al. "Split-ring resonator experiments and data analysis at FLUTE". In: *14th International Particle Accelerator Conference, Venedig, 7th-12th MAy 2023.* 14th International Particle Accelerator Conference. IPAC 2023 (Venedig, Italien, May 7–12, 2023). Ed. by Ralph Assmann et al. 54.11.11; LK 01. JACoW Publishing, 2023, pp. 4760–4763. ISBN: 978-3-95450-231-8. DOI: 10.18429/JACoW-IPAC2023-THPL122.

[52] Anton Malygin et al. "Status of the FLUTE RF System Upgrade". en. In: *Proceedings of the 13th International Particle Accelerator Conference* IPAC2022 (2022), Thailand. DOI: 10.18429/JACOW-IPAC2022-THPOST008. URL: https://jacow.org/ipac2022/doi/JACoW-IPAC2022-THPOST008.html.

[53] Xiaojun Wu et al. *Half-percent terahertz generation efficiency from cryogenically cooled lithium niobate pumped by Ti:sapphire laser pulses.* 2016. arXiv: 1601.06921 [physics.optics].

[54] M. Nabinger et al. "Commissioning and Experiments with a Compact Transverse Deflecting System at FLUTE". In: *Proc. IPAC'24.* International Particle Accelerator Conference 15. JACoW Publishing, Geneva, Switzerland, 2024.

[55] Andrzej Wolski. *Beam Dynamics in High Energy Particle Accelerators.* IMPERIAL COLLEGE PRESS, 2014. DOI: 10.1142/p899. eprint: https://www.worldscientific.com/doi/pdf/10.1142/p899. URL: https://www.worldscientific.com/doi/abs/10.1142/p899.

Danksagung

Diese Arbeit wäre ohne die Unterstützung vieler Menschen nicht möglich gewesen. In diesem Abschnitt möchte ich mich bei allen Beteiligten herzlich bedanken.

Zunächst möchte ich Prof. Dr. Anke-Susanne Müller danken für die Möglichkeit, am IBPT zu promovieren.

Ebenso gilt mein Dank Prof. Guido Drexlin, der die Rolle des zweiten Gutachters sofort übernahm und eine unerreichte Geschwindigkeit in der Kommunikation zeigte.

Ein besonderer Dank geht an Dr. Bastian Härer, dessen Gabe, das Wesentliche vom Unwesentlichen zu trennen, stets dafür sorgte, dass ich nicht in den Details meiner Arbeit verloren ging.

Weitere Dankesworte möchte ich der Graduiertenschule KSETA aussprechen, die mir die Gelegenheit bot, viele Kurse zu verschiedenen wissenschaftlichen Themen zu besuchen.

Ein großes Dankeschön geht an alle meine Kollegen in der THz-Gruppe, die eine freundliche, kreative, humorvolle und sehr lebendige Arbeitsumgebung schufen. Ein besonderer Dank gilt Micha Reissig, Sebastian Maier und Chenran Xu, die in unzähligen Kaffeepausen immer für Brainstorming über alle möglichen Details bereit waren. Ein riesiger Dank geht auch an Nigel Smale und Thiemo Schmelzer, die sich mit den kleinsten, verruchtesten Details von FLUTE auskennen und stets sofort zur Hilfe waren, wenn mal wieder etwas klemmte oder bugte.

Das TDS-Experiment begann mit dem Vorhaben, mal eben Streaking nachzuweisen. Damals ahnten wir nicht, auf welche Moloch-Arbeit wir uns einstellten. Mein herzlicher Dank geht an das TDS Team, von dem jeder einzelne so unerbittlich und unermüdlich die vermeintlichen Rückschläge aushielt, um am Ende doch mit Erkenntnissen und Erfolgen diese Arbeit abschließen zu können. Special thanks to Sergei Glukhov who was always eager to dive into the deepest and nastiestest details. Ein großes Dankeschön auch an Michael Nasse, der es trotz aller Verpflichtungen täglich zum Kontrollraum schaffte und direkt mit dabei war beim Experiment, beim Grübeln und beim Planen. Last but not least danke ich Matthias Nabinger. Stoisch und unermüdlich am Arbeiten, am Laser, an FLUTE, an neuen Teilen und Umbauten, und vor allem am humorvollen und motivierten Tandem, das wir Tag für Tag im Kontrollraum abgaben. Ohne dein Zutun wäre die Messkampagne, gar das ganze TDS-Projekt, niemals möglich gewesen. Meine Hochachtung und ewige Dankbarkeit an Matthias Nabinger. Der krasseste Laserboy wo gibt.

Zu guter Letzt möchte ich meiner liebevollen Familie für ihre tolle Unterstützung über all die Zeit danken. Meine Eltern haben mich immer ermutigt, meinen Interessen zu folgen, und waren für mich da, wenn die Dinge nicht wie geplant liefen.

Ein herzliches Dankeschön geht an meine dufte DMZ. Möge der Rage weiter brennen. Vielen Dank für mächtig Reee in unserer süßen Echo-Kammer. Besonders dem Jan sei gedankt. Wie ein gutes Stück Küchenrolle hat er die tägliche Ladung Frust und Verzweiflung aufgesaugt. Insbesondere in der Corona-Zeit warst du ein wichtiger Pfeiler, um mich bei Verstand zu halten. Danke!

Zum Abschluss möchte ich mich bei meiner Anastasiia bedanken. Du hast es täglich geschafft, meinen Kopf kühl und mein Gemüt fröhlich zu halten. Danke für deine ganze Unterstützung.

A. Appendix

A.1. Laser damage threshold

In order to assess the laser energy density that could cause damage, a laser damage threshold LDT was found experimentally. The laser was directed to irradiate various spots on the cathode while the power was increased. Subsequently, the specimens were observed with a light microscope.

The laser spot size was set to a minimum. The laser power for this test was measured approximately 1 m before the cathode at an accessible point on the optical table adjacent to FLUTE. Between this measurement point and the cathode, the laser passes several optical components and partially travels through air. As a result, this value serves as a reference for the FLUTE setup and should not be interpreted as an absolute value.

Within this context, the findings revealed that the copper cathode surface experienced damage at an energy density of $32\,\mathrm{mJ/cm^2}$. It is important to note that this test was conducted without any RF power. It can be assumed that when RF power is in operation, the limit for safe operation would be lower. Nevertheless, this LDT result helps in preventing damage to the cathode, thereby saving both time and resources.

A.2. Collision of electrons with the resonator

The electron beam collides with the resonator material in various scenarios. These scenarios include steering the beam towards the gap, fluctuations in the beam position, or just a too large beam. Consequently, a study was performed to examine the consequences resulting from these collisions.

Simulation setup: These questions have been kindly investigated by Alfredo Ferrari[1]. For this study, the simulation software called Fluka [30] was used where the resonator is represented as a flat, infinite large wall. The simulation represents the resonator as a flat, infinite large wall, made of the real resonator composition, one $76\,\mu\mathrm{m}$ thick glass layer coated by a layer of $2\,\mu\mathrm{m}$ gold on each side. The electrons in the simulation were modeled with a momentum of $5\,\mathrm{MeV/c}$, without any energy spread or divergence.

---

[1] Alfredo Ferrari, IAP & IBPT - Karlsruhe Institute of Technology

(a)   (b)
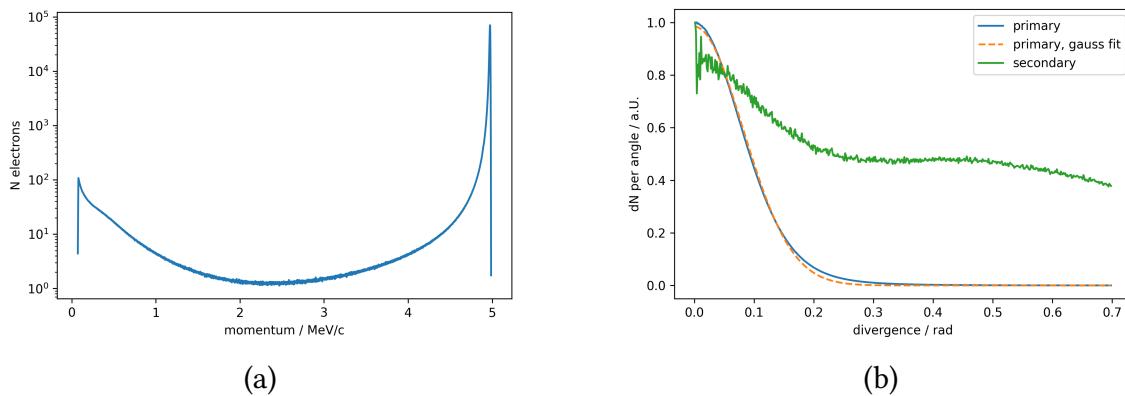
Figure A.1.: Results of the FLUKA simulation of the electron beam colliding with the resonator material. a) shows the momentum spectrum and all electrons after impact, including secondary, note the logarithmic scale. b) shows the angular spread breakdown between primary and secondary electrons in a normalized, linear scale.

Upon interaction, the electrons scatter and deposit some energy onto the material. Additionally, on average 0.6 % of primary electrons release a secondary electron. This process of course also draws energy of the primary electron beam and introduces an angular spread on the bunch.

Energy drop: The total momentum spectrum of all electrons, primary and secondary that reaches the beam monitor is visualized in fig. A.1 (a). Mind the logarithmic scale, the vast majority of primary electrons remains close to the initial momentum. In fact, the energy loss for 88 % of the primary electrons is below 50 keV, and still below 100 keV for 95 % of them.

Since after the impact with the resonator, the electrons just travel passively to the YAG screen, this energy drop can be neglected.

The momentum spectrum displays a second, broad peak at lower momenta, that describes the secondary electrons. More important for those is their angular spread angular spread.

Introduced angular spread: The scattering with the material causes an angular divergence of the primary electron bunch, as is depicted in fig. A.1 (b). The simulation result is shown (blue) as well as a Gaussian distribution, fitted onto the data set (orange, dashed).

The other, green curve represents the angular spread for the released, secondary electrons. The secondary electrons are so few in numbers and so widely spread out, that one can savely neglect their influence on the screen image. The additional green curve represents the angular spread of the released, secondary electrons. These secondary electrons are so few and so widely spread, rendering it safe to neglect their impact on the screen image.
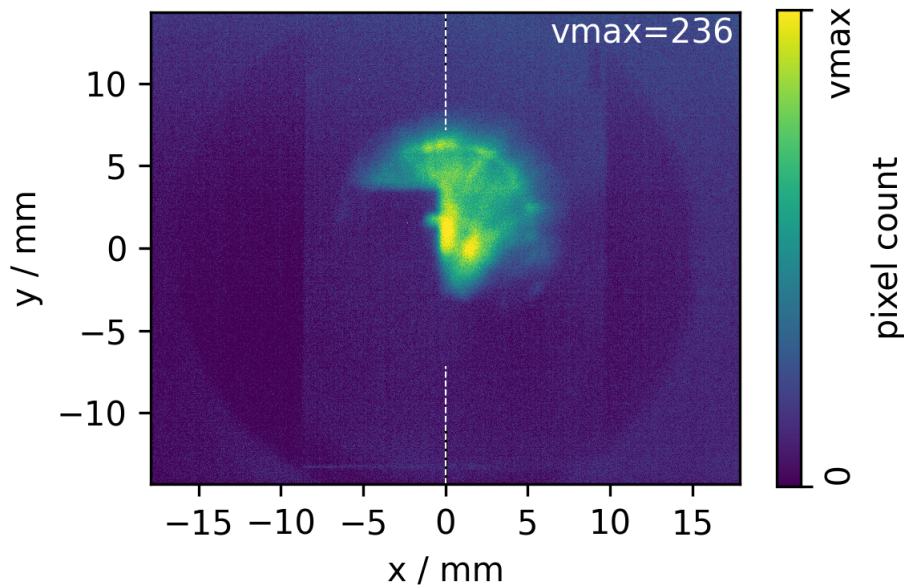
Figure A.2.: YAG screen image of the electron bunch with the resonator shadow visible. The shadow is a result of the scattering of electrons flying through the resonator material. The color map upper limit, vmax, is set to the 99.9 % quantile of all pixel counts in this image.

Conclusion: The secondary electrons can be neglected in any means in this thesis.

The primary electrons carry an additional angular spread after the impact. The gaussian fit model allows to quantize this spread as a (1 sigma) standard deviation of 81 mrad. This introduced spread is quite large compared to typical divergence values of below 20 mrad in the drift section after focusing on the SRR.

The angular spread after impact leads to a decreased charge density behind the SRR material. This reduced density aligns with the resonator's geometry, resulting in a shadow-like pattern of the resonator on the YAG screen image.

This observation is supported by actual experimental YAG screen images, where the impression of the resonator is clearly visible, as shown in fig. A.2[2]. This image does not show streaking but only the blockage.

A.3.   Momentum spread measurement, second method

The mightier, second solution is to interpret the momen dum spread from a single screen image. Therefore the screens horizontal axis needs to be mapped to a corresponding momentum.

Yet, the stretched screen image does not solely depend on the momentum spread but also by the beam size itself. Therefore the beam size and divergence at the spectrometer

---

[2]   This figure has been shown already as fig. 1.11.

entrance needs to be taken into account. One way to cope with that is to calculate the relations via matrix formalism. This mathematical tool is well introduced in [55], also all used matrices in this thesis are discussed by this source.

In matrix formalism one can parameterize a particle exactly in the 6-D phase space by the following vector

$$v_0 = \left[x_0, x\prime_0, y_0, y\prime_0, z_0, \delta \right]^T \tag{A.1}$$

with the horizontal, vertical and longitudinal positions x, y and z, the transverse divergences $x\prime$, $y\prime$ and the momentum deviation δ of the particles momentum p from the reference momentum p_{ref} as

$$\delta_0 = \frac{p_0}{p_{\text{ref}}} - 1. \tag{A.2}$$

The transition from passing through an element is obtained by multiplying the correct transfer matrix onto the vector. The required matrices in our case are the sector dipole M_{sec} and the following drift section M_{drift}. The drift section matrix is

$$M_{\text{drift}} = \begin{bmatrix} 1 & L_D & 0 & 0 & 0 & 0 \\ 0 & 1 & 0 & 0 & 0 & 0 \\ 0 & 0 & 1 & L_D & 0 & 0 \\ 0 & 0 & 0 & 1 & 0 & 0 \\ 0 & 0 & 0 & 0 & 1 & 0 \\ 0 & 0 & 0 & 0 & 0 & 1 \end{bmatrix} \tag{A.3}$$

with $L_{D,30} = 0.545\,\text{m}$ the length of the drift section in the 30° spectrometer arm and respectively the straight arm drift section spans $L_{D,0} = 0.550\,\text{m}$.

The sector dipole matrix is more complex:

$$M_{\text{sec}} = \begin{bmatrix} c & r\,s & 0 & 0 & 0 & r\,(1-c) \\ -s/r & c & 0 & 0 & 0 & s \\ 0 & 0 & 1 & r\,\theta & 0 & 0 \\ 0 & 0 & 0 & 1 & 0 & 0 \\ s & r\,(1-c) & 0 & 0 & 1 & r\,(\theta - s) \\ 0 & 0 & 0 & 0 & 0 & 1 \end{bmatrix} \tag{A.4}$$

with the design deflection radius $r = 0.3\,\text{m}$ and the design deflection angle $\theta = 30° = 524\,\text{mrad}$ of the spectrometer dipole. The terms $\cos(\theta)$ and $\sin(\theta)$ have been abbreviated to c and s.

The particle is deflected by the spectrometer and transported through the drift section:

$$v_{1,30} = M_{\text{drift},30}\, M_{\text{sec}}\, v_0 = \left[x_{1,30}, x\prime_{1,30}, y_{1,30}, y\prime_{1,30}, z_{1,30}, \delta \right]^T \tag{A.5}$$

$$= \begin{bmatrix} \delta\left(L_{D,30}s + \rho\,(1-c)\right) + x_0\left(-\frac{L_{D,30}s}{\rho} + c\right) + x\prime_0\left(L_{D,30}c + \rho s\right) \\ \delta s + x\prime_0 c - \frac{x_0 s}{\rho} \\ y_0 + y\prime_0\left(L_{D,30} + \rho\theta\right) \\ y\prime_0 \\ \delta\rho\,(\theta - s) + \rho x\prime_0\,(1-c) + x_0 s \\ \delta \end{bmatrix} \tag{A.6}$$

From this complicated expression the focus lies in the first element, on the horizontal deposition $x_{1,30}$ and its linear dependence on δ, x_0 and $x\prime_0$. This result of $x_{1,30}$ shows, that the energy spread stretches out the bunch linearly (in first order), yet suffers from an overlay depending on the bunches position and spread at the spectrometer entrance.

The matrix formalism is constructed such, that the z-coordinate of a particle refers to the reference particle $z = 0$. The generic particle $v_{1,30}$ has a finite z-value, this means it does not reach the screen or it even surpassed it by traveling the distance $L_{D,30}$. A correction for the horizontal deposition could be calculated quite easy:

$$\tilde{x}_{1,30} = x_{1,30} + z_{1,30}\, x\prime_{1,30} \tag{A.7}$$

This correction introduces only second order and mixed terms of δ, x_0 and $x\prime_0$ that stay neglected for the time beeing.

To aquire the necessary parameters $x_0, x\prime_0$ one needs at least two additional information. One possibility is a second profile measurement with the second profile monitor in the straight arm. There the particle is described by the vector:

$$v_{1,0} = \begin{bmatrix} x_0 + x\prime_0\, L_{D,0} \\ x\prime_0 \\ y_0 + y\prime_0\, L_{D,0} \\ y\prime_0 \\ 0 \\ \delta \end{bmatrix} \tag{A.8}$$

By measuring the vertical beam size σ_y in both arms, one can isolate the initial position from the divergence.

$$\sigma_{\text{spec},y} = y_0 + y\prime_0\, (L_{D,30} + \rho\theta) \tag{A.9}$$

$$\sigma_{\text{straight},y} = y_0 + y\prime_0\, L_{D,0} \tag{A.10}$$

$$y\prime_0 = (\sigma_{\text{spec},y} - \sigma_{\text{straight},y})a(L_{D,30} + \rho\theta - L_{D,0}) \tag{A.11}$$

$$y_0 = \sigma_{\text{straight},y} - y\prime_0 L_{D,0} \tag{A.12}$$

Utilize the rotation symmetry before the dipole one can identify $x_0 = y_0$ and $x\prime_0 = y\prime_0$ and so solve $x_{1,30}$ for the energy deviation δ.

Although this second method allows to interpret the full screen image, it required some assumptions. The matrix formalism neglects second order terms, the effect of space charge and the dipole fringe fields. Also it depends on the rotation symmetry that is only in first order fulfilled in the experiment. Also the discussed systematic overestimation of the YAG profile measurement comes into play only by interpretating the beam size. Hence, making the simple approach of moving the beam edges into the screen center a more robust method.
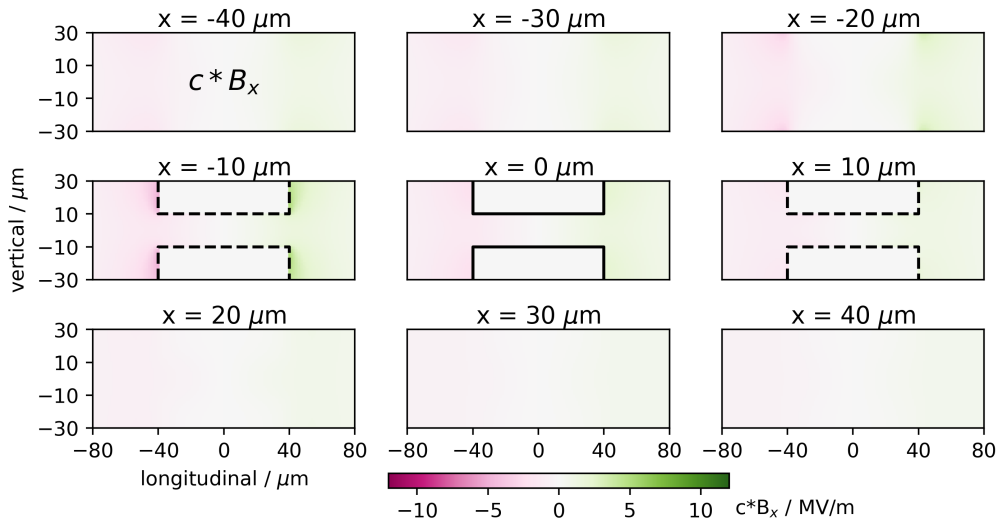
A.4. Streaking field cross sections
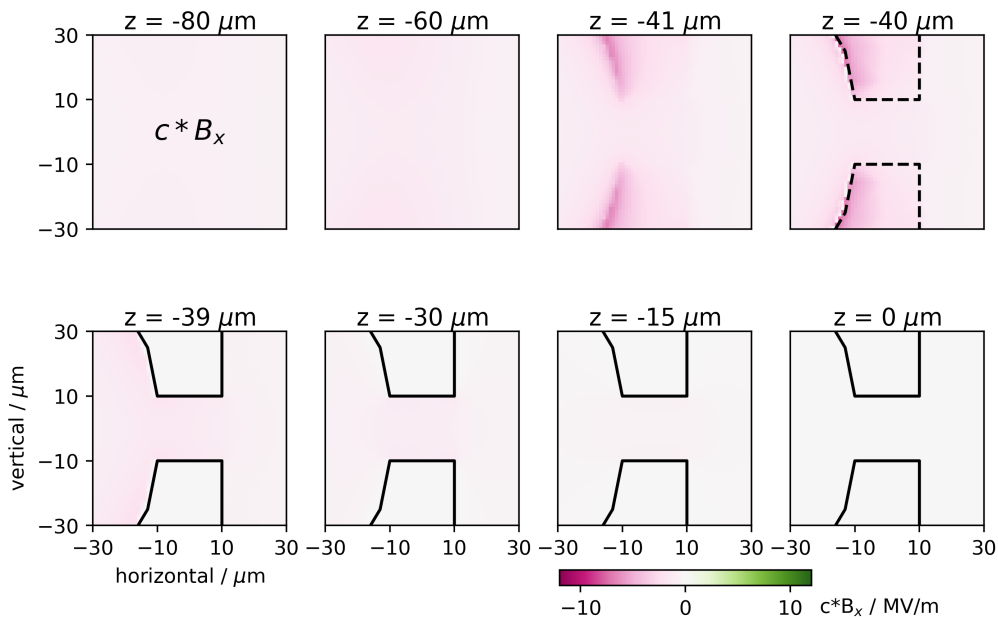

Figure A.3.: B_x in x direction.
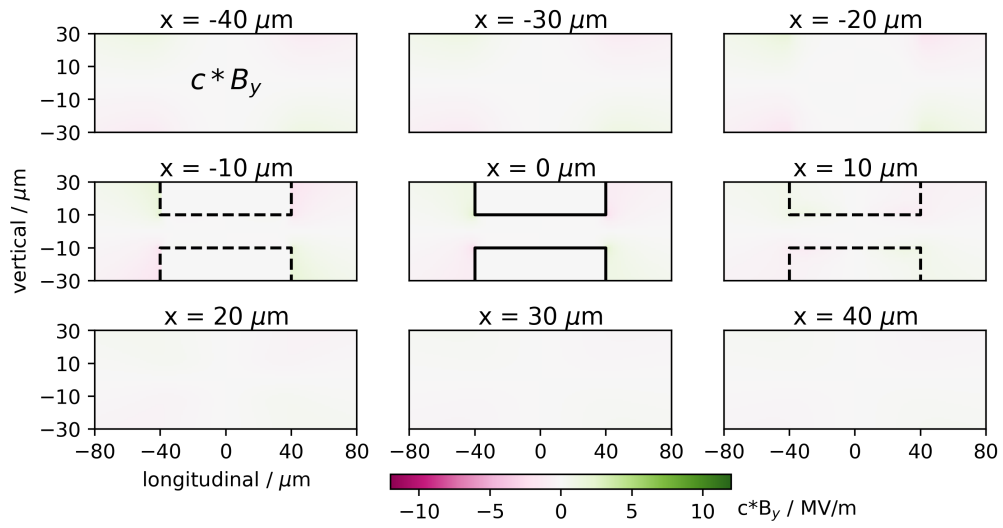

Figure A.4.: B_x in z direction.
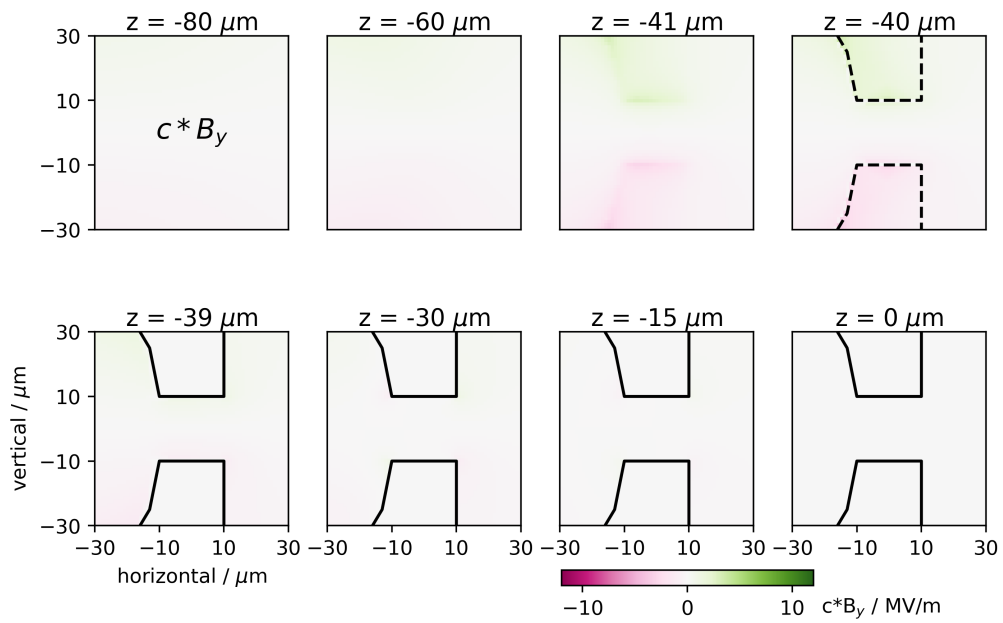
Figure A.5.: B_y in x direction.

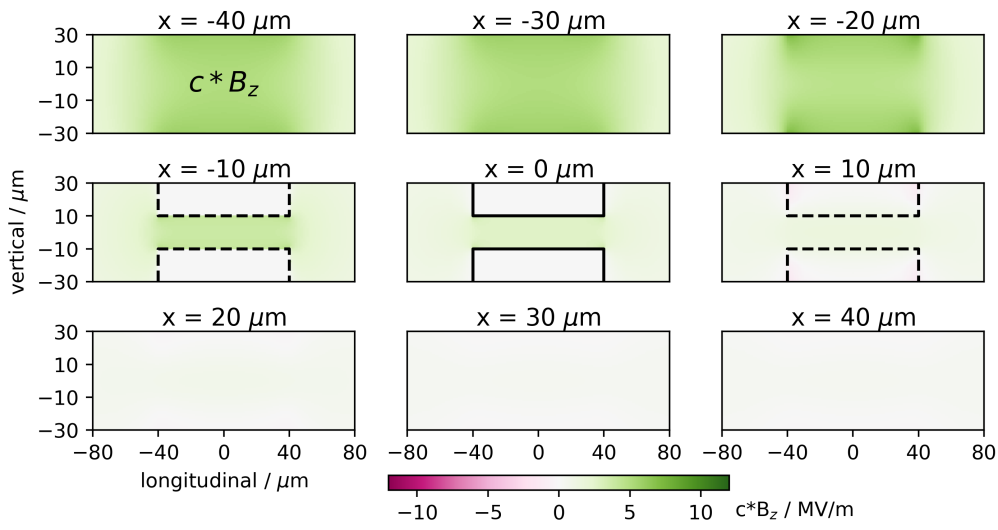**Figure A.6.:** B_y in z direction.

A.5. RAP experiment data analysis
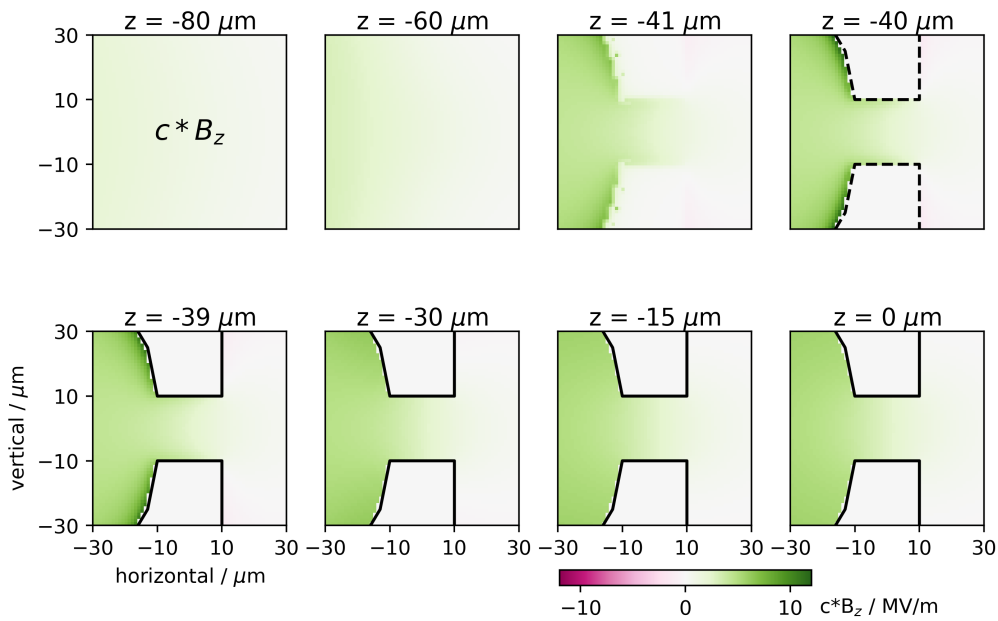
Figure A.7.: B_z in x direction.
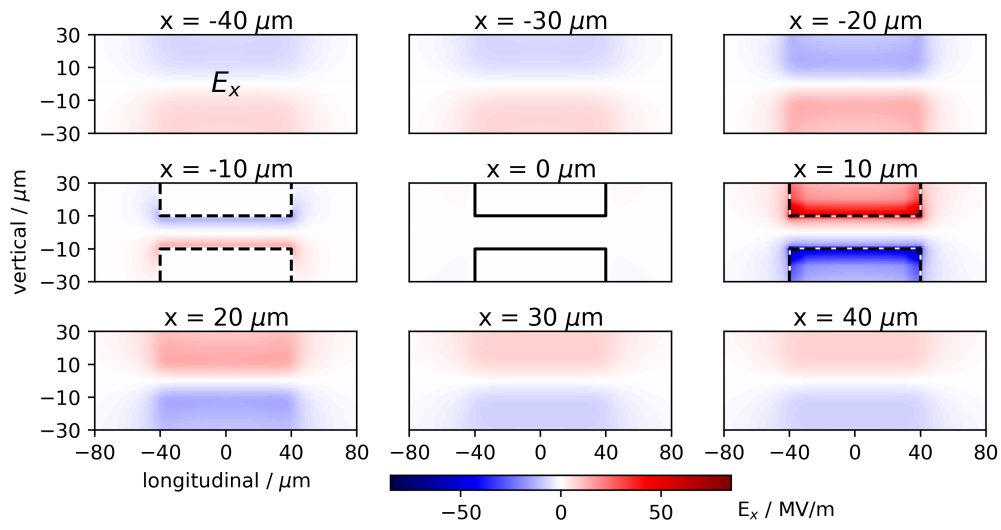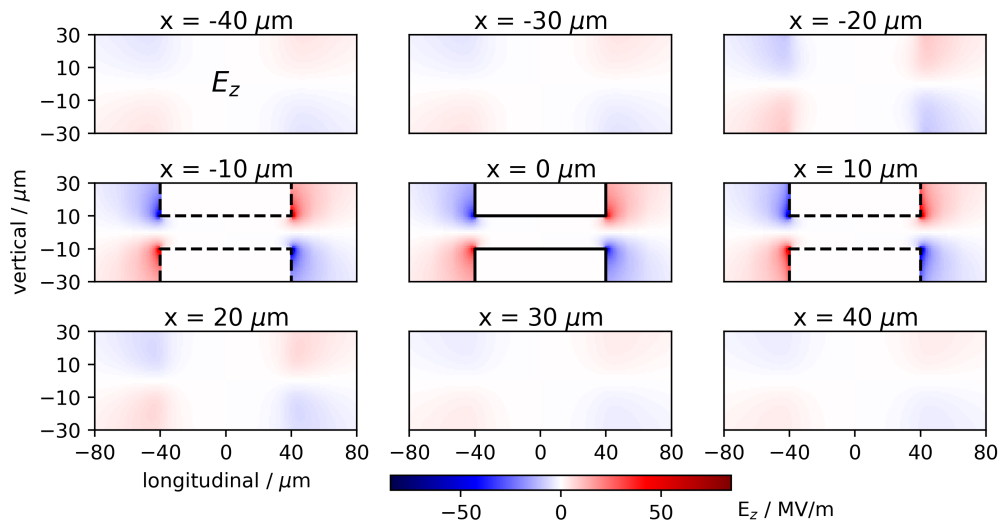

Figure A.8.: B_z in z direction.

Figure A.9.: E_x in x direction.
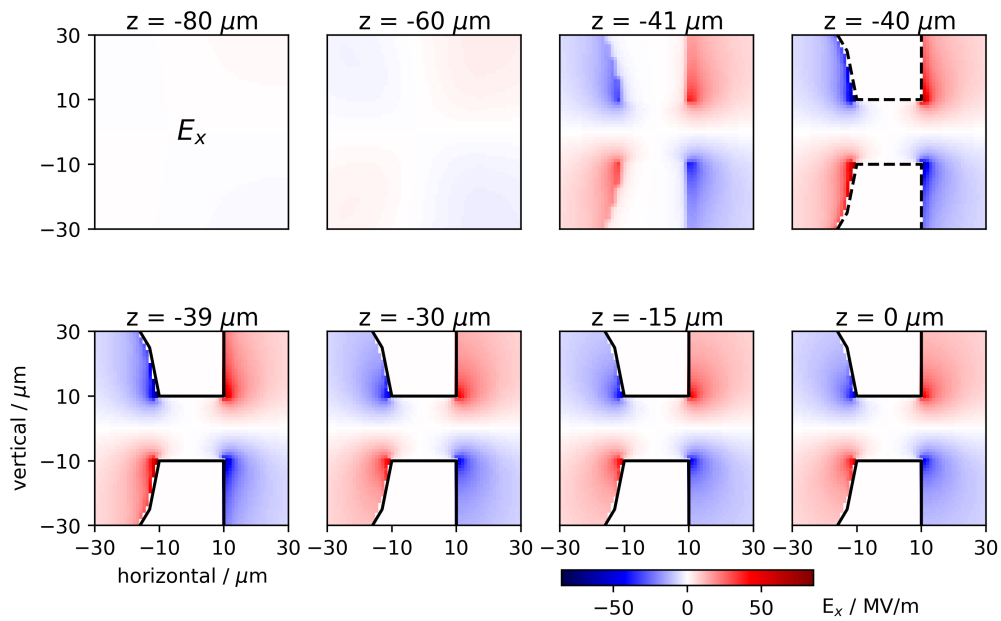
Figure A.10.: E_x in z direction.
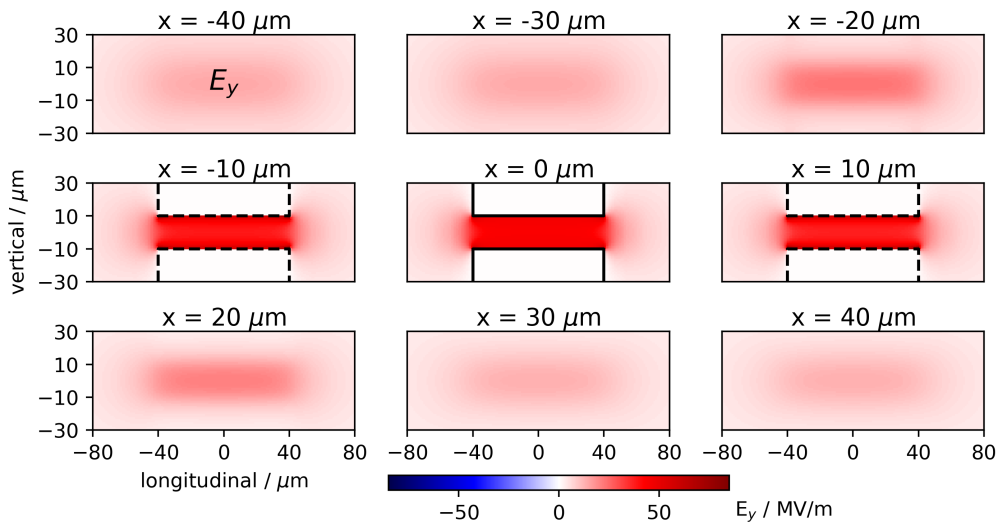
Figure A.11.: E_y in x direction.
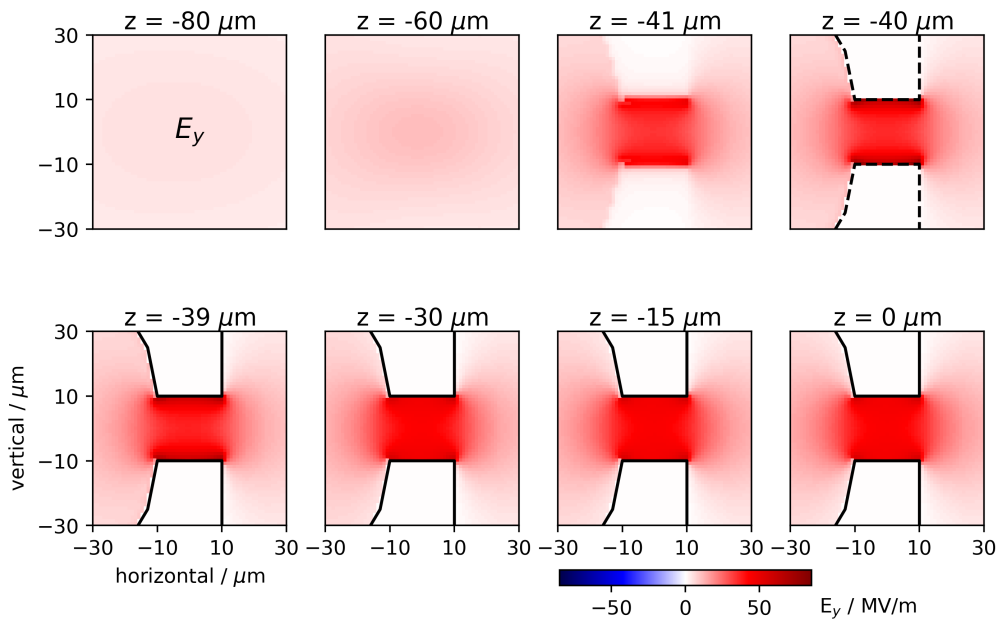
Figure A.12.: E_y in z direction.
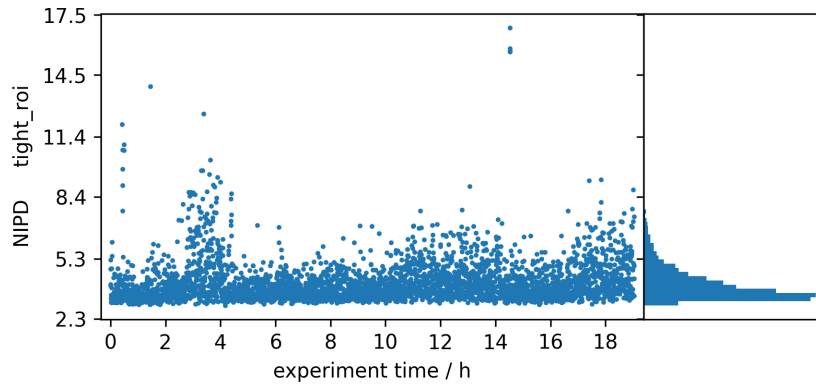
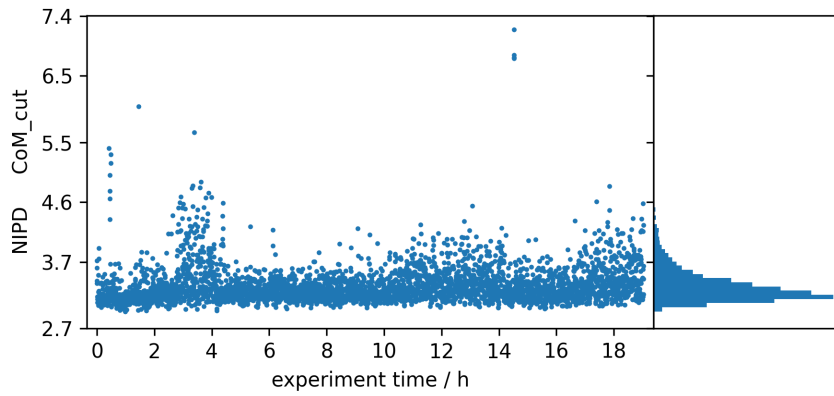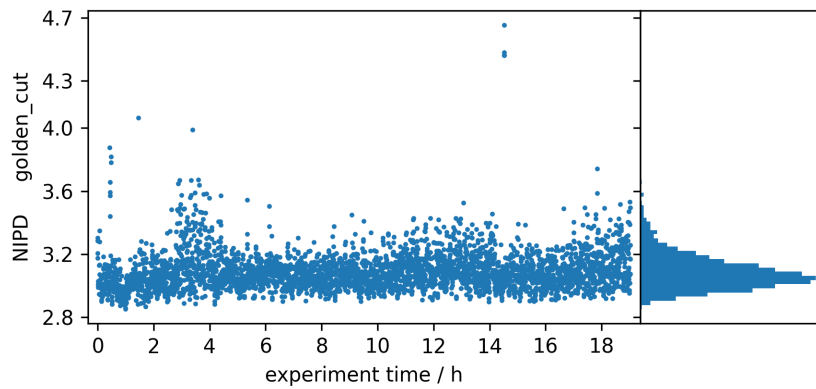**Figure A.13.:** E_z in x direction.
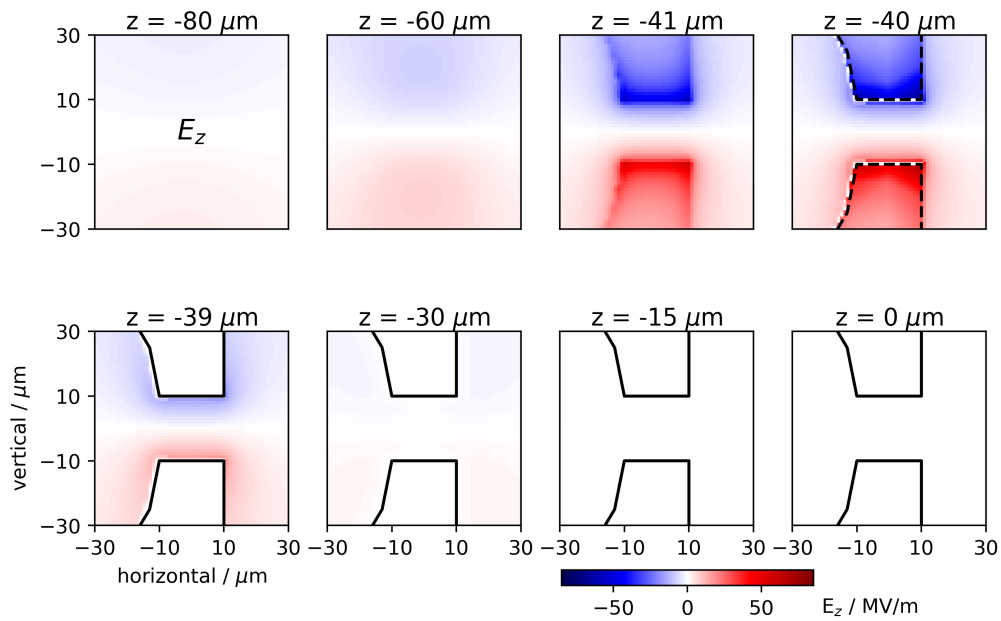
Figure A.14.: E_z in z direction.

(a)

(b)

(c)

Figure A.15.: NIPD values during a *contrast* RAP experiment with a) tight ROI, b) CoM ROI and c) golden ROI, presented against the experiment time. A projection of all NIPD values is attached on the right.